T2R2 東京科学大学 リサーチリポジトリ
Science Tokyo Research Repository

論文 / 著書情報
Article / Book Information

題目(和文)	Alを含有しない組成傾斜分離閉じ込めヘテロ構造による波長980nm高出力半導体レーザの研究 / Al オ ガンユウ シナイ ソセイ ケイシャ ブンリ トジコメ ヘテロ コウゾウ ニ ヨル ハチョウ 980nm コウシュツリョク ハンドウタイ レーザ ノ ケンキュウ
Title(English)	A study of high-power aluminum-free 980-nm graded-index separate-confinement-heterostructure lasers
著者(和文)	大久保典雄
Author(English)	
出典(和文)	学位:博士(工学), 学位授与機関:東京工業大学, 報告番号:乙第3221号, 授与年月日:1998年9月30日, 学位の種別:論文博士, 審査員:
Citation(English)	Degree:Doctor (Engineering), Conferring organization: Tokyo Institute of Technology, Report number:乙第3221号, Conferred date:1998/9/30, Degree Type:Thesis doctor, Examiner:
学位種別(和文)	博士論文
Type(English)	Doctoral Thesis

Powered by T2R2 (Science Tokyo Research Repository)

A Study of High-Power Aluminum-Free 980-nm Graded-Index Separate-Confinement-Heterostructure Lasers

by

Michio Ohkubo

Adviser : Professor Shigehisa Arai

Tokyo Institute of Technology
2-12-1 O-okayama, Meguro-ku, Tokyo, 152-8552, Japan

A Study of High-Power Aluminum-Free 980-nm Graded-Index Separate-Confinement-Heterostructure Lasers

Table of Contents

Chapter 1 Introduction 1

1.1 Background of Fiber-Optic Telecommunications 1

1.1.1 History of Fiber-Optic Telecommunications 1

1.1.2 Overview of Erbium-Doped Fiber Amplifiers 4

1.2 Importance of Aluminum-Free 980-nm Lasers 8

1.2.1 Semiconductors for Pumping EDFAs 8

1.2.2 Status of AlGaAs/GaAs-Based Lasers 10

1.2.3 Advantages of InGaP/GaAs-Based Lasers 11

1.2.4 Requirements to 980-nm InGaP/GaAs-Based Lasers 12

1.3 Objectives of This Study 16

1.3.1 Objectives of This Study 16

1.3.2 Outline of This Thesis 16

References 18

Chapter 2 Design Consideration of Graded-InGaAsP Structures 25

2.1 Requirements of High-Power Lasers 25

2.2 Characterization of Band Discontinuity of InGaP/InGaAsP/GaAs System 27

2.2.1 Band Discontinuity of InGaP/GaAs Heterojunction 27

2.2.2 Estimation of Band Discontinuity of InGaP/InGaAsP/GaAs System 29

2.3 Design Consideration of Graded-InGaAsP Structures 35

2.3.1 Reduction of Heterojunction Spikes of InGaP/GaAs 35

2.3.2 Formation of Electric Field due to Graded-InGaAsP Structures 39

2.4 Summary 45

Appendix A Graded-GaAsP Base HBTs 46

References 51

Chapter 3 Fabrication and Characterization of Graded-InGaAsP Structures 54

3.1 Metal Organic Chemical Vapor Deposition Growth of Graded-InGaAsP Structures 54

3.1.1 MOCVD apparatus 54
3.1.2 Growth of InGaP Layers Lattice-matched to GaAs 56
3.1.3 Growth of InGaAsP Layers Lattice-matched to GaAs 57
3.1.4 Photoluminescence Study of InGaAsP Alloys on GaAs 61
3.1.5 Growth of InGaAsP/InP Single Quantum Wells 63
3.1.6 Growth of Graded-InGaAsP Structures 67
3.2 Fabrication and Characterization of Graded-InGaAsP Structures 69
3.2.1 Characterization Scheme of Graded-Structures Using HBTs 69
3.2.2 InP-Based D-HBTs 70
3.2.3 Concept of InP/InGaAs D-HBTs with Graded-InGaAsP Collector 71
3.2.4 Epitaxial Structures and Device Fabrication of D-HBTs 72
3.2.4 Characterization of Graded-InGaAsP Structures 73
3.2.5 Ultimate Graded-Structures : Continuous Grading 78
3.3 Summary 81
References 82

Chapter 4 Fabrication of High-Power Lasers with Graded-InGaAsP Structures 84
4.1 Fabrication Process of Polyimide Buried Ridge Waveguide Lasers 84
4.2 Performance of Basic Structures with Undoped (GRIN-)SCH 87
4.2.1 Epitaxial Structures 87
4.2.2 Performance 88
4.3 Advantages of Doped Graded Bandgap Structures 90
4.3.1 Low Series Resistance 90
4.3.2 High Carrier Injection Efficiency 91
4.3.3 High Power Operation 98
4.4 Controlled Graded Refractive Index Waveguides 99
4.4.1 High Coupling Efficiency into A Single Mode Fiber 99
4.4.2 High Reliability 107
4.5 Summary 108
Appendix B Beam Steering 109
References 113

Chapter 5 Improvement of Temperature Dependence of GRIN-SCH Lasers 115

5.1 Improvement of Temperature Dependence with Low Mirror Loss 115

5.2.1 Sample Preparation 115

5.2.2 Improvement in Lasing Performance 115

5.2 Consideration Using Current-Gain Relation 118

5.3 Summary 122

References 123

Chapter 6 Conclusions 124

Acknowledgment 126

List of publication 127

Chapter 1

Introduction

1.1 Background of Fiber-Optic Telecommunications

1.1.1 History of Fiber-Optic Telecommunications

In the recent years, the information traffic has been launching into a leap of increase where information-service networks have been accelerating in spread — internet and cable television (CATV), etc. It is expected that a trunk line for multimedia networks will soon need a transmission capacity of several hundred Gb/s (1 Gb/s = 1×10^9 bit/s). Against this background, the technology for fiber-optic telecommunications, which is upgrading year by year, is required to manipulate that demand of magnitude.

Glancing at Table 1-1, it is no exaggeration to say that the development of optical fibers can represent the history of fiber-optic telecommunications. In 1966, Kao and Hockham illustrated a perspective of possible glass-fiber medium communications [1]. The fiber-optics has since brought forward a revolution in the telecommunications, especially in two decades during the interim. In 1970, a fiber with a faint loss of round 20 dB/km came into existence at Corning Glass Works [2].

Then the first cw operation of GaAs-based semiconductor lasers was set in action [3,4]. The complex of optical devices operating around 850 nm and a low loss optical fiber was fabricated, forming the lead-off lightwave system in 1978 [5].

In the 1970s, the transmission distance was considerably lengthened with a wavelength region of 1300 nm that had been found to produce less loss than at 850 nm [6], in concurrence with zero dispersion [7]. Meanwhile, a great deal of effort was exerted on the development of InP-based semiconductor lasers. Treading the heels of the initial trial cw operation of InP-based lasers [8,9], there appeared in 1985, an installation of a Fiber-optic telecommunications System (named F-400M, equipped with a 1300-nm single-mode fibers, owned by NTT). The F-400M system formed the trunk lines, ranging all over the main islands of Japan, from the uppermost (Asahikawa) to the lowermost (Kagoshima) — a total of 3400 km in length. Even as recently as the 1980s, fiber loss set serious bounds on the maximum transmission distance in a region of 1300-nm wavelength. By contrast, the F-400M incurred least fiber losses, owing to the epoch-making technology for low-loss/long piece-length fiber fabrication — Vapor-phase Axial Deposition (VAD) method [10]. In effect, the repeater interval of the F-400M reached as long as 40 km.

In the year 1979, a record fiber loss of 0.2 dB/km (then theoretical threshold) emerged around 1550 nm of wavelength in a fiber made by the VAD method [11]. At the

same time, it was demonstrated that the dispersion to narrow down the bandwidth of the silica fiber could fully be controlled or suppressed [12,13]. This mechanics gave birth to Dispersion-shifted Fiber that is designed to minimize its loss at 1550 nm or thereabout.

Moreover, the successful cw operation of InGaAsP/InP semiconductor lasers in a 1500-nm region gave momentum to the R&D of fiber-optic telecommunications at round 1500 nm, in 1979 [14-16]. Those evolutions made the 1500-nm optical communication promising in the 1980s. In particular, DFB [17] and DBR [18], the powerful replacement of Fabry-Perot lasers, have paved a fairway for the single longitudinal mode operation in wavelength, which was thereby sharpened, turning out to argument the transmission capacity and stretch the interval of repeaters.

Table 1-1. Historical milestones of semiconductor laser and optical fiber.

Year	Semiconductor Laser	Opitical Fiber
1970	R.T. CW GaAs/AlGaAs Laser [3,4]	20dB/km [2]
1975		Zero Dispersion @1.3μm [7]
1976		0.47dB/km@1.3μm [6]
1977	R.T. CW 1.3μm GaInAsP/InP Laser [8,9]	
1979	R.T. CW 1.5μm GaInAsP/InP Laser [14-16]	0.2dB/km@1.5μm [11]
1981	R.T. CW 1.5μm GaInAsP/InP DBR Laser [18]	
1982	R.T. CW 1.5μm GaInAsP/InP DFB Laser [17]	

In step with the single-mode fiber technology under development, a rare-earth doped fiber amplifier arose from the R&D of fiber amplifiers. Erbium, one of the rare-earth dopants, had arrested the most attention, allowing for the 1500-nm region, since the pioneer report on a rare-earth-doped glass laser emerged in 1964 [19]. An erbium-doped fiber amplifier (EDFA) is capable of serving as a power amplifier to boost the output power of a transmitter, an optical repeater to recover fainting signals, or an optical

preamplifier to improve receiving sensitivity. EDFAs necessitate no detection, regeneration or retransmission of signal. Moreover, performance enhancement can readily be implemented in an EDFA-based network system, by alterations on the terminal station. Being equipped with EDFAs, independent of any bit rates of transmission, the network-wide transmission capacity can be increased, on the strength of many-fold modifications in the terminal station [20].

In the 1980's, the R&D of EDFAs was providing for fiber-optic telecommunications of the next generation [21-23]. What was especially noteworthy took place in 1989: an experimental 212 km repeater-free transmission line (at 1.8 Gb/s, with semiconductor laser pumped EDFAs) was detailed in a paper [24]. This trail transmission has since propelled the application of an EDFA-based transmission system into a rapid growth.

Figure 1-1 sheds light on trend in transmission capacities of fiber-optic networks built by NTT [25] in Japan, from 1980 onward. The traditional methodology for broadening the bandwidth of transmission in telecommunications relied on Time-Division-Multiplexing (TDM) and electronic and optical components which were racing for higher speed, namely, semiconductor lasers, photodetectors and semiconductor electronics circuits (ICs), etc. The TDM system has emphatic merits: scalability assurance and operation, administration and maintenance (OAM). Besides, the TDM unit is easy to compactify and to increase in a single-channel bit rate. With the aid of lessening fiber loss, the TDM-based transmission were doubling in capacity every year, throughout the 1980s. At length, the bit rate of a commercial model, put into practice in 1995, reaches a record level of 10 Gb/s [26]. Now already, transmission systems designed for 40 Gb/s, in combination with ultra-high-speed lasers, receivers and ICs, are under development [27]. But then, it is expected that a limit of transmission bandwidth might rest beyond 40 Gb/s [28].

In view of clearing out those electrical operating limits, Wavelength-Division-Multiplexing (WDM) technique does deserve attention, because the optical fiber has ultimately broad optical bandwidth (30 THz, 1 THz = 1×10^{12} Hz). By way of illustration, an early trial WDM transmission was reported in 1985 [29], utilizing 10-wavelength channels with aggregate capacities of 20 Gb/s. Also, it is of special note that TDM and WDM technologies very recently combined to create an overall capacity of more than 1 Tb/s (1 Tb/s = 1×10^{12} bit/s) [30-33]. The combination involved forefront EDFAs and sophisticated single-mode technologies. The next section describes 'EDFA' which forms one of the key components of fiber-optic telecommunication systems.

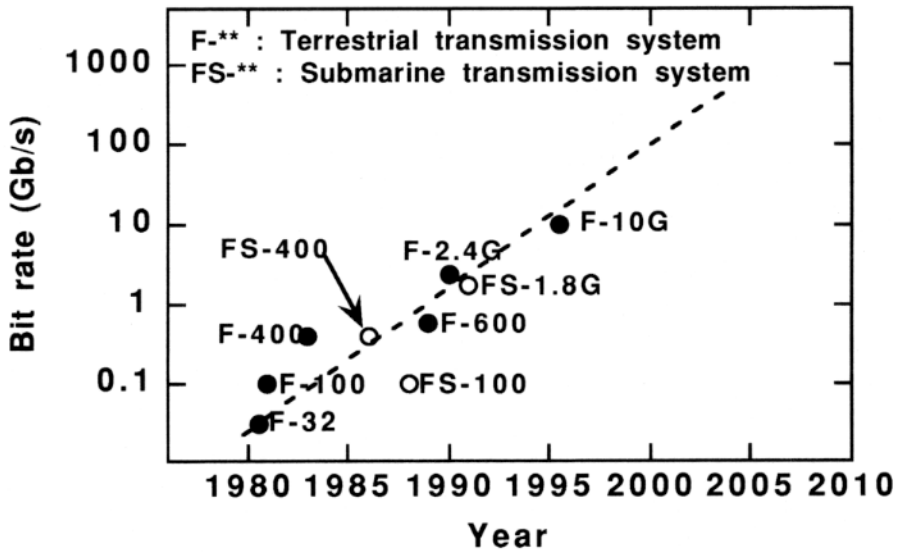

Fig. 1-1. Trend in transmission capacities of the fiber-optic networks built by NTT in Japan [25].

1.1.2 Overview of Erbium-Doped Fiber Amplifiers

In general, a current fiber-optic telecommunication system incorporates regenerative repeaters, located at specific intervals, in itself, which rejuvenate fading signals — remaining identifiable throughout the transmission line. Earlier than the advent of EDFAs, the conventional repeater converted, in a photodiode, input optical signals into the electronic counterparts, which were, in turn, amplified by ICs. The amplified electronic signals were reconverted into the optical counterparts by semiconductor lasers, which were finally injected into the regular transmission. What if optical signals could be directly amplified without any bypass? The optical reaper could be smaller and less costly than any electronic one, including less noise. Thus, branching loss would also be compensated with an optical amplifier. Here it is thinkable that more flexible communication networks will come into existence, owing to necessitating no conversion between optical and electronic signals — optical signals are handled without any transformation. On analysis, an all -optical communications system is judged to be promising to all intents and purposes, and expected to realize advanced telecommunication services at some handy price.

Manifold types of optical amplifiers have been proposed and investigated. Among others, what were used, on trial, for optical transmission purposes, are a

semiconductor laser amplifier using a semiconductor laser [34-36], a doped-fiber amplifier using an optical fiber with a special dopant [37-40], and a fiber Raman amplifier [41]. Figure 1-2 illustrates brief schemes of these amplifiers. A laser amplifier is pumped by current; a doped-fiber amplifier and a fiber Raman amplifier are pumped by light (laser light). A laser amplifier, being no doubt compact, can be integrated into a photonic IC, acting to great advantage. Conversely, a fiber Raman amplifier in need of ultra high driving power can never be made up of lasers diodes, acting to vital disadvantage to practical applications. Now, the EDFA, representative of doped-fiber amplifiers is very attractive in view of likely laser-diode pumping and superior characteristics.

Table 1-2 summarizes comparison of the typical optical amplifiers. The EDFA leads other rivals in gain and polarization independence, and is equipped with enough bandwidth and a preferable light-pumping source. It generalizes down to the result that the EDFA-based optical amplifier will be the most authentic approach to the realization of a powerful fiber-optic telecommunications system.

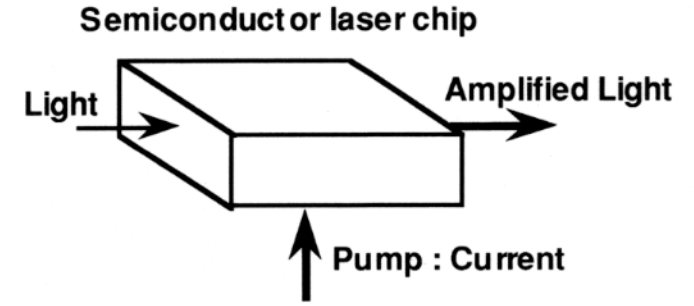

(a) Laser amplifier

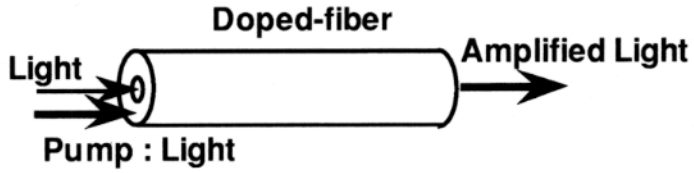

(b) Doped-fiber amplifier

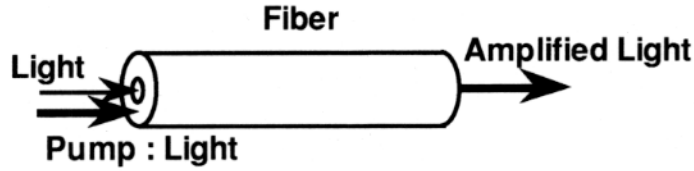

(c) Fiber Raman amplifier

Fig. 1-2. Configurations of optical amplifiers: (a) laser amplifier, (b) doped-fiber amplifier, and (c) fiber Raman amplifier.

Table 1-2. Comparison of optical amplifiers.

	LD amp.		EDFA	Fiber Raman
	TWA	FPA		
Typical Optical gain	30dB	20-30dB	30-45dB	20-45dB
Bandwidth (20-dB gain)	1THz	10GHz	500GHz	3THz
Saturation power	+10dBm	-5dBm	+10dBm	+30dBm
Polarization dependent	Yes	Yes	No	No
Pumping	Current	Current	LD light	Laser light

Figure 1-3. shows a typical EDFA configuration, consisting of an erbium-doped fiber, a pumping source, a wavelength multiplexing coupler, an isolator and an optical filter. The erbium-doped fiber, with a relative short length of less than 100 m, has its core doped with an erbium (an optical rare-earth element) of less than 0.1 %. At the outset of the search of the EDFA, an argon-ion laser or a dye laser was used as a pumping source. Yet, a high-power laser diode is preferable for similar practical purposes [24].

Let's touch on a brief function of the other components. An isolator is interposed to suppress the lasing oscillation and block out returns of the amplified spontaneous emission (ASE). Optical connectors, likely sources of reflection, should not be applied unless attached with enough reflectionproof. To maintain a stable high gain, fusion splice can preferably serve to connect fiber-optic components. An optical filter is also interposed to eliminate ASE. A narrow-band optical filter safeguards the EDFA against noise, a great deal.

Meanwhile, other dopants (Nd^{3+}, Sm^{3+}, Tu^{3+}, Pr^{3+}) as doped into fibers of amplifiers were examined, to determine whether or not to adapt themselves to some more regions including a wavelength of 1300 nm [42-44] and a wavelength of around 1700 nm [45]. Then, there has been growing much expectation for Pr^{3+}-doped fluoride glass fiber amplifiers (PDFA) for 1300 nm [46], abreast with the progress of a 980-nm high-power semiconductor laser under development. The PDFA for 1300 nm will be often used for analog optical transmission systems (e.g. CATV) in Japan, owing to its pumping by light of 1017 nm in wavelength.

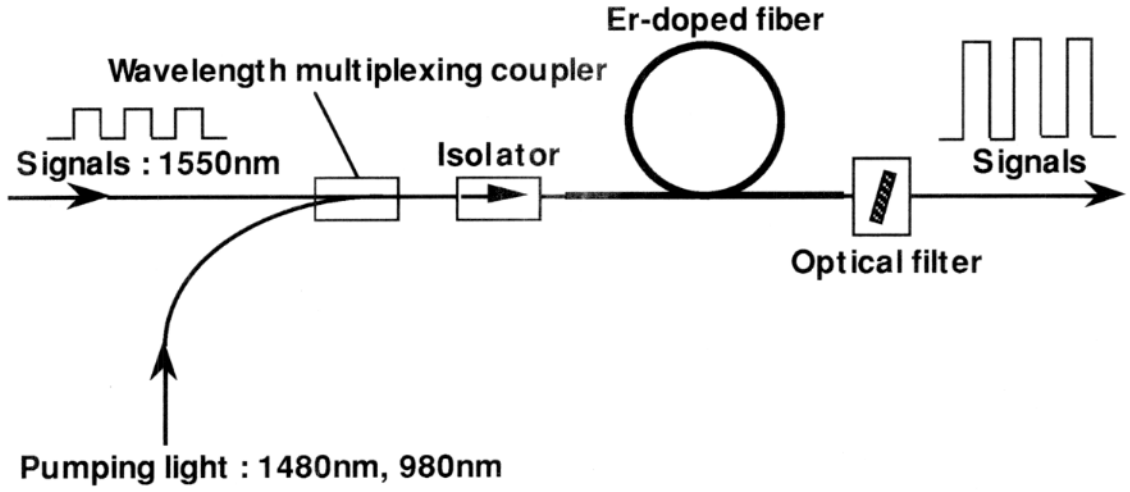

Fig. 1-3. Configuration of the EDFA.

1.2.1 Semiconductor Lasers for Pumping EDFAs

First, let's try grasping the EDFA in principle. Figure 1.4 shows the energy-level diagram of an erbium-doped fiber [47]. It has been demonstrated that erbium can be pumped directly into the $^4I_{13/2}$ metastable level or higher energy level (e.g. $^4I_{11/2}$, $^4I_{9/2}$, and $^4F_{9/2}$), which slide down to the metastable level, through nonradiative decay. During the transition to the ground state, photons spontaneously emit, or are stimulated to emission. It is considered that the EDFA can apply a three-level model shown in Fig. 1-5, except for 1480-nm pumping. The threshold of a three-level system corresponds to the initial state (ground state), where energy absorption takes place — called Ground-State Absorption (GSA) — thus pumping power will be absorbed or dissipated. Amplification is designed to occur, when the pump power exceeds a certain value (threshold power). Also, the EDFA, attaching to a three-level system, is of the optimum doped-fiber length. A 1480-nm-laser-pumped EDFA is other than ideal, because of not being located in an authentic three-level system but in a quasi-three-level system. Consequently, all ions can be inverted in energy from the $^4I_{15/2}$ to the $^4I_{13/2}$, which results in decrease in gain coefficient and increase in noise figure value.

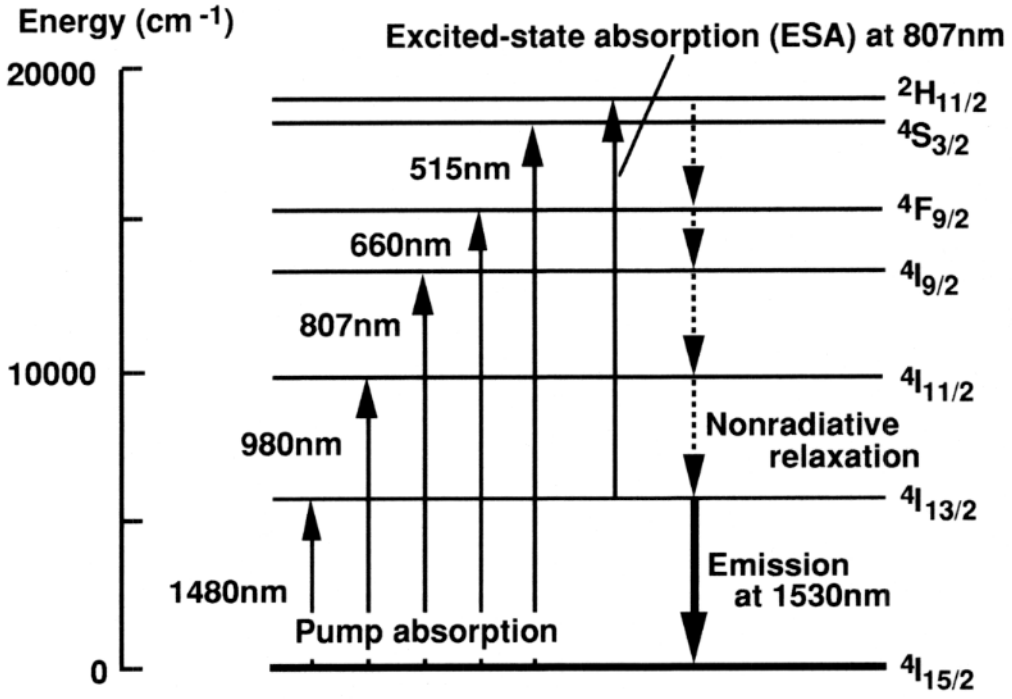

Fig. 1-4. Erbium energy-level diagram.

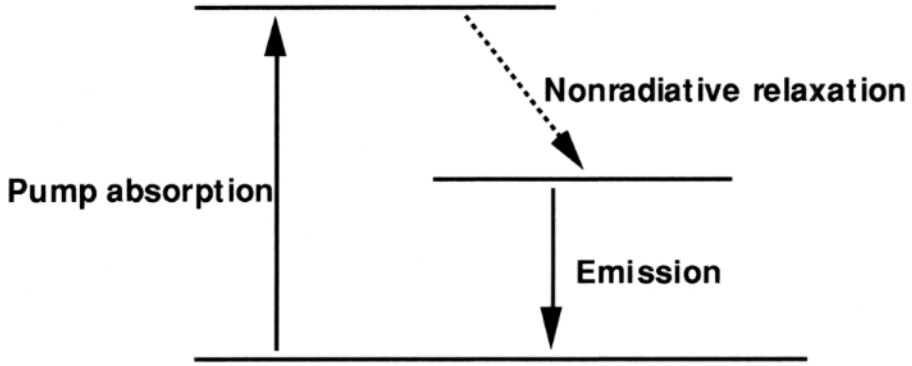

Fig. 1-5. Doped-fiber amplifier model : three-level system.

Practical wavelength for pumping purposes are 807 nm [48], 980 nm [49] and 1480 nm [50], for each of which a high-power semiconductor laser is available. Yet, a significant magnitude of unwanted absorption — Excited-State Absorption (ESA) — occurs at 807 nm, where ions can still more be excited and plunged into higher energy, from the densely populated metastable level. This phenomenon narrows down the gain coefficient at 807 nm in pumping power to as meager as round 0.3 dB/mW, one tenth of that at 980 nm or 1480 nm.

Today, InP-based 1480-nm pumping semiconductor lasers are in widespread use for EDFAs, because of their being handily available and considerably reliable. However, it is true that another laser with a shorter wavelength 980 nm can offer advantages over one with a longer wavelength of 1480 nm. Table 1-3 contrasts a few keypoints of 980-nm and 1480-nm pumping lasers. Emphatic factors in selecting a pumping semiconductor laser refer to an optical gain coefficient and a noise figure. Since an EDFA pumped by a 980-nm laser attaches to a three-level system, the optical gain coefficient with a 980-nm laser exceeds what to be produced with a 1480-nm laser remaining subjected to a quasi-two-level system [51,52]. Amplified Spontaneous Emission (ASE) can conceivably form a noise source. An erbium-doped fiber amplifies input signals, which are in turn attached with some ASE light, thereby forming sources of output shot-noises or beat-noises at the output. The ASE noise is theoretically more likely to be suppressed using a pumping wavelength of 980 nm, rather than 1480 nm [53,54]. Amplifiers, each equipped with a 980-nm pumping laser, also have a lower noise figure close to a quantum limit of 3 dB[55]. By contrast, the other's noise figure is 5 dB [56]. At the same time, emphasis should be laid on the temperature dependence of optical gain. An EDFA with a 980-nm pumping laser, exhibits less temperature-dependence of optical gain, than one with a 1480-nm pumping laser [57]. A window for 980-nm pumping is narrower than one for 1480-nm pumping. However, a fiber Bragg grating is applied to stabilize a lasing wavelength, with the result that the lasing wavelength of 980-nm laser can match with the pumping window of the EDFA [58,59].

Meanwhile, 980-nm pumping GaAs-based lasers are more efficient in operation and less sensitive to temperature, than 1480-nm InP-based lasers — necessitating less electric power and less cooling equipment. Now it is thinkable that 980-nm pumping GaAs-based lasers, and high-gain and low-noise EDFAs can combine to lay down a fairway for extremely effective and cost-saving performance. From the above perspective, EDFAs attached with 980-nm GsAs-based laser are most likely to serve to upgrade the fiber-optic telecommunications.

Table 1-3. Contrastive natures of 980-nm and 1480-nm pumping lasers.

	1480nm	980nm
Gain coefficient	5.1dB/mW [51]	11dB/mW [52]
Noise figure	5dB [56]	3dB [55]
Pumping window	30nm	10nm

1.2.2 Status of AlGaAs/GaAs-Based Lasers

Figure 1-6 casts on light on 'bandgap vs. lattice constant' for III-V compound semiconductors. An $Al_XGa_{1-X}As$/GaAs system is ready to vary its bandgap energy and refractive index with change in the mole fraction, without lattice-constant. This natural ability toward a perfect heterojunction in the AlGaAs/GaAs system, leads up to considerable flexibility in device design and fabrication. Besides, a direct transition is available from X=0 to X=0.4, thereby facilitating the fabrication of laser diodes emitting in a range of 700 to 880 nm. It was 1984 when the lead-off audio optical disks: CDs (compact discs) went on sale; they were of 780 nm in wavelength and with a long life of round 8000 hours at 5 mW of output. The production of laser chips has been on the increase and counts no fewer than one million a month. Here, the AlGaAs/GaAs-based semiconductor laser can be concluded to be one of the most successful industrial applications in terms of compound semiconductor devices.

In the mid-1980s, a quantum well laser was demonstrated with success [60], followed by a growing interest in extending the emission wavelength beyond 880 nm. By adding a small amount of indium to a GaAs quantum well, the emission wavelength can be extended up-to 980 nm, at which the EDFA can operate. It was suspected that built-in compressive strain in the active region could destroy the long-term reliability. The suspicion was frozen, one way or another [61-65]. In brief, assuming a strained layer never to exceed its critical layer thickness, the mismatch between InGaAs and GaAs can induce a trifle of strain, yielding scarcely any influence on the reliability.

The R&D in growth and fabrication of 980-nm lasers has been progressed rapidly. As a result, state-of-the-art AlGaAs cladding lasers are now commercially

available today [66,67]. Yet, AlGaAs/GaAs-based 980-nm lasers are not reliable, especially for undersea use. Should 980-nm lasers be upgraded up to an acceptable level, they will serve for pumping purposes in fiber-optic telecommunications.

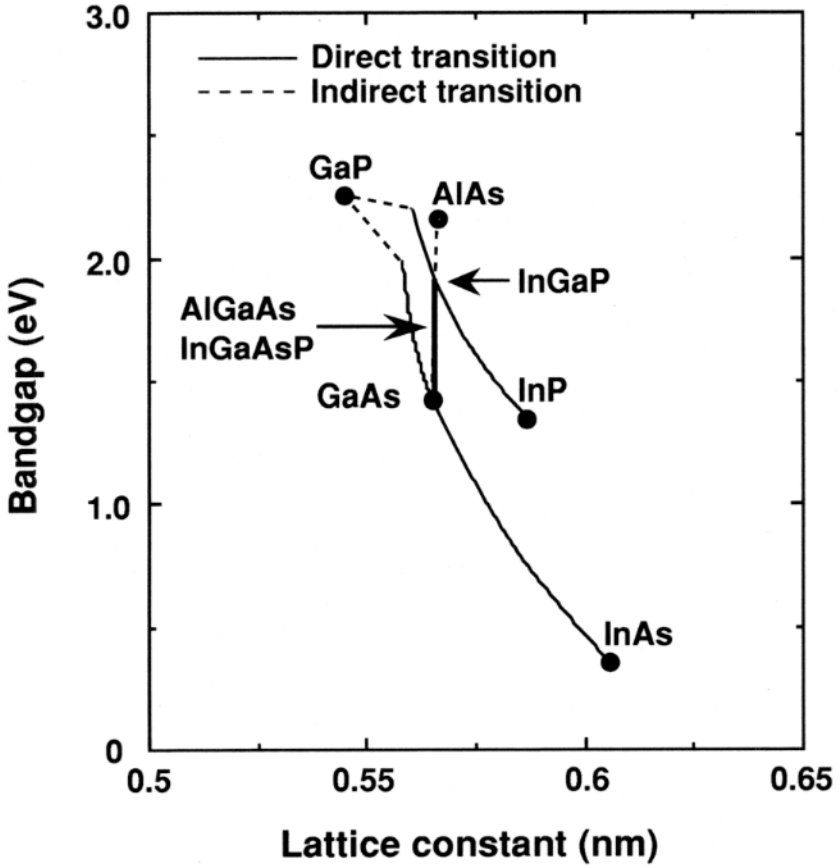

Fig. 1-6. Bandgap vs. lattice constant for III-V compound semiconductors.

1.2.3 Advantages of InGaP/GaAs-Based Lasers

First, let's consider the reliability issue of AlGaAs/GaAs-based lasers. The degradation of high-power AlGaAs/GaAs lasers is mainly caused by instability of the interface between the laser facet and anti-reflection coating film. It results from rapid facet-oxidation due largely to aluminum content [68]. In order to avoid the oxidation, trial aluminum-free material were contrived to replace the AlGaAs by $In_{1-X}Ga_XP$ (hereinafter represented by InGaP) which can be lattice-matched to GaAs at X=0.51, as is shown in Fig. 1-6. Not to mention that the facet-oxidation was decreased, InGaP brought out a several advantages, which seem to have virtually encouraged the fabrication of InGaP/GaAs-based devices.

Listed below are those advantages:

1) oxidation lessened enough,

2) selective chemical etching between GaAs and InGaP being available[69],

3) InGaP/GaAs interface exhibiting very low recombination velocity (1.5 cm/s) [70],
4) InGaP mass transport technique being available [71].
The feature 1) will lead up to far more stability than that of AlGaAs. Recombination centers increase, abreast with oxidation in progress; as a result, AlGaAs/GaAs-based laser devices continue degrading during fabrication. Also, it is desirable for the multiple-step growth [72]. The feature 2) makes the fabrication process simpler and raises fabrication yield. The feature 3) suppresses the space-charge recombination current at a base-emitter junction, when used for heterojunction bipolar transistors (HBTs) quipped with an InGaP emitter and a GaAs base. In particular, a dopant of carbon serves as p-type dopant in AlGaAs/GaAs for HBTs, and serves as n-type in InGaP. Being amphoteric, sharp p/n junction forms at the interface between InGaP and GaAs[73]. The feature 4) was applied to fabricate a buried heterostructure laser [74], which was demonstrated with success.

1.2.4 Requirements to 980-nm InGaP/GaAs-Based Lasers

In early stage of this study, much attention have been paid the pumping lasers for EDFAs at 980 nm, equipped with strained layer quantum wells. A fiber-optic communications system as a public utility necessitates ultimately reliable lasers and refuses any AlGaAs/GaAs-based lasers. In due course, we have been determined to use InGaP as a cladding material, which can offer the advantages as mentioned in the last section.

In 1990, we have demonstrated the first successful fabrication and high-power cw operation of aluminum-free InGaAs/GaAs/InGaP strained layer single quantum well ridge waveguide lasers [75]. Since then there have been followed a great deal of researchers to fabricate 980-nm lasers using this system [72,76-79]. Papers comparing AlGaAs and InGaP in reliability deserve attention [80,81]. These reports suggested that InGaP-based 980-nm and 800-nm lasers might have potential of better reliability than AlGaAs-based ones.

Fig. 1-7 shows the schematic drawing of first fabricated 980-nm ridge waveguide InGaAs/GaAs/InGaP lasers [75]. The layers consist of

i) n-GaAs buffer layer,
ii) n-InGaP cladding layer,
iii) undoped GaAs SCH layer,
iv) strained layer single quantum well active layer,
v) undoped GaAs SCH layer,
vi) p-InGaP cladding layer,
vii) heavily doped p^+-GaAs contact layer.

In the upper cladding layer, a 3-nm-thick p-GaAs layer is inserted for fabricating

a ridge waveguide lasers: the GaAs layer acts as an etching stop layer (E.S.L.) in the etching process to form a ridge waveguide structure by selective chemical etchant.

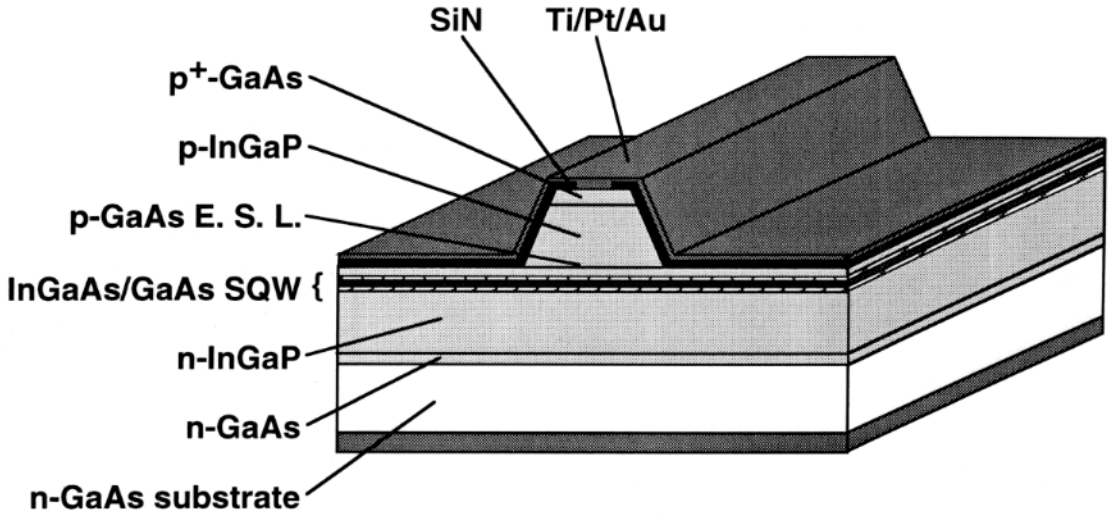

Fig. 1-7. Schematic drawing of first fabricated ridge waveguide InGaAs/GaAs/InGaP lasers [75].

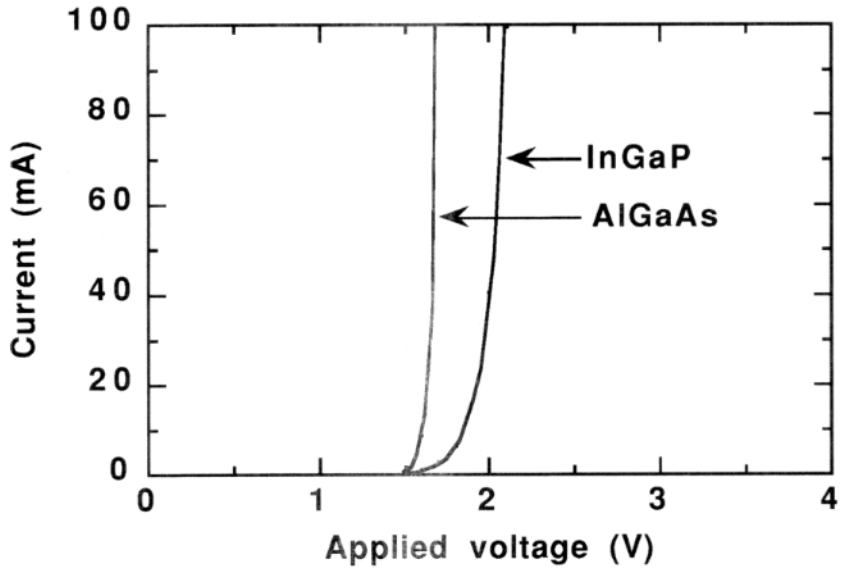

Fig. 1-8. Comparison of I-V characteristics of ridge waveguide lasers.

This laser is similar to the 980-nm AlGaAs cladding laser in most performance, except for power consumption. Actually, as shown in Fig. 1-8, an InGaAs/GaAs/InGaP SCH laser (with abrupt junction) exhibited nonlinear high series resistance, as contrasted with AlGaAs cladding lasers, having the same width of mesas. This drawback can be conceived as proceeding from the voltage drop across the InGaP/GaAs hetero-interface, especially where a large valence band discontinuity in the p-side junction.

It was studied out how effects of band discontinuity of InGaP/GaAs heterojunction could serve on current-voltage (I-V) characteristics of *Npn*- and *Pnp*-InGaP/GaAs heterojunction bipolar transistors [82]. Hole injection across the InGaP/GaAs hetero-interfaces needs much higher voltage than electron injection, which indicates that the valence band discontinuity affects the I-V characteristics of lasers seriously. A graded junction is a powerful approach to the suppression of heterojunction spikes caused by band discontinuity, [83,84]. On analysis, the optimization of GaAs/graded-InGaAsP/InGaP is capable of improving the I-V characteristics. Moreover, the graded-structure can form an electric field, due to variation in the bandgap, thereby enabling the carrier population in a quantum well to increase [85].

An InGaP/GaAs system exhibits other uncontrollable disadvantages over against an AlGaAs one: a lower hole mobility and a higher thermal resistivity. Figure 1-9 makes comparison in hole mobility between InGaP and $Al_{0.4}Ga_{0.6}As$ — the aluminum composition 0.4 is conventionally used to make 980 nm lasers [86]. It should be noted that the hole mobility of InGaP is lower by a factor of 1/3 than that of $Al_{0.4}Ga_{0.6}As$, resulting in a high series resistance of InGaP cladding lasers. Also, InGaP, with a higher thermal resistivity of InGaP of 20 cm℃/W than $Al_{0.4}Ga_{0.6}As$'s 9 cm℃/W [87], has to bring out less reliability in high-power operation — some restriction in need.

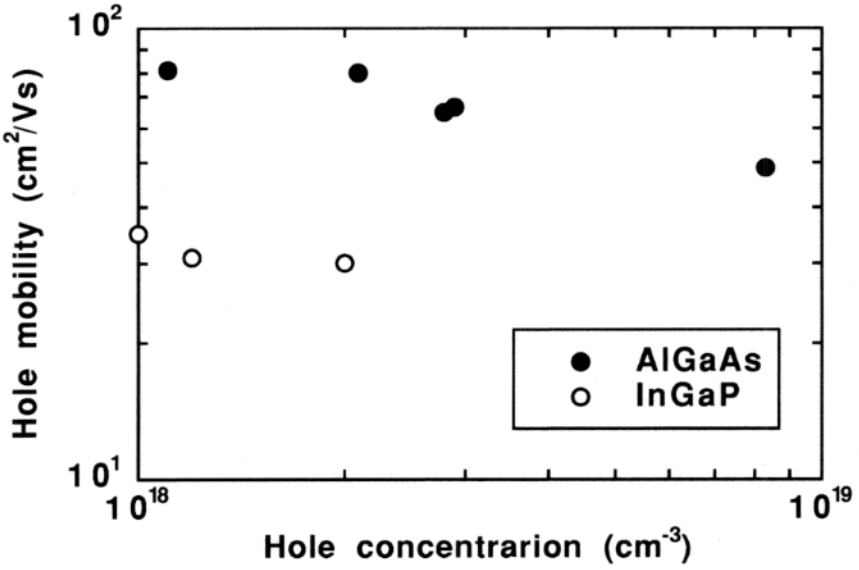

Fig. 1-9. Comparison of the hole mobility of InGaP and $Al_{0.4}Ga_{0.6}As$.

Again listed below are disadvantages of an InGaP/GaAs system over against a AlGaAs/GaAs system:

1) Larger valence band discontinuity,

2) Lower hole mobility,

3) Higher thermal resistivity.

1.3 Objectives of This Study

1.3.1 Objectives of This Study

As touched on from phase to phase in the text of 'Introduction', this study was intent on lasing performances of aluminum-free 980-nm lasers in combination with InGaP cladding layers with graded-InGaAsP materials lattice-matched to GaAs. The study applied Metal-Organic Chemical Vapor Deposition (MOCVD) to grow an InGaP/InGaAsP/GaAs system.

The purpose of this study are listed below:

1. Design optimization of graded-structures of aluminum-free 980-nm GRIN-SCH lasers.
2. Investigation and establishment of MOCVD growth of InGaAsP layers on GaAs.
3. Realization and characterization of aluminum-free 980-nm GRIN-SCH lasers.

1.3.2 Outline of This Thesis

This paper consists of six chapters:

Chapter 1 introduces the intent of this paper.

Chapter 2 discusses the band lineup of InGaP/InGaAsP/GaAs system. Here I remark on advantages and effects of the graded bandgap structure aluminum-free 980-nm lasers.

Chapter 3 describes the MOCVD apparatus used for this study, and the growth of InGaAsP lattice-matched to GaAs Here, I demonstrate the fabrication and characterization of graded-structures.

Chapter 4 discusses the advantages and lasing characteristics of 980 nm lasers provided with the graded-structures around an active layer — so-called GRIN-SCH lasers.

Chapter 5 discusses temperature dependence of lasing characteristics along with mirror loss.

Chapter 6 concludes this paper.

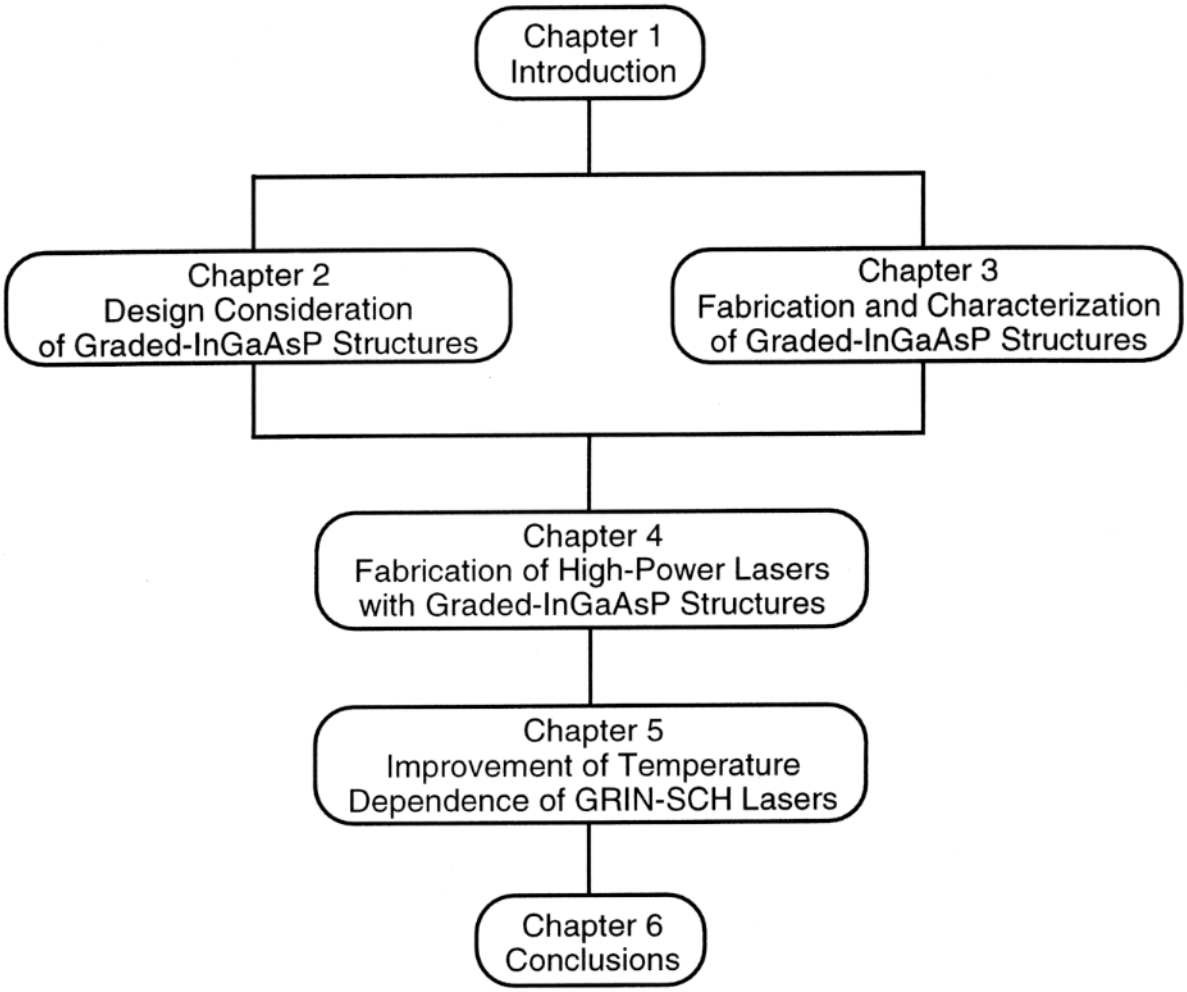

Fig. 1-10. Outline of this thesis.

References

[1] K. C. Kao and G. A. Hockham, "Dielectric-fibre surface waveguide for optical frequencies," *Proc. IEE*, vol. 113, pp. 1151, 1966.

[2] F. P. Kapron, D. B. Keck and R. D. Maurer, "Radiation losses in glass optical waveguides," *Appl. Phys. Letters*, vol. 17, pp. 423, 1970.

[3] I. Hayashi, M. B. Panish, P. W. Foy and S. Sumski, "Junction lasers which operate continuously at room temperature," *Appl. Phys. Lett.*, vol. 17, pp. 109-111, 1970.

[4] Zh. I. Alferov, V. M. Andreev, D. Z. Garbuzov, Yu. V. Zhilyaev, E. P. Morozov, E. L. Portnoi and V. G. Trofim, "Investigation of the influence of AlAs-GaAs heterostructure parameter on the threshold current and the realization of continuous emission at room temperature," *Soviet Phys. Semiconductors*, vol. 4, pp. 1573-1575, 1971.

[5] D. L. Baldwin, T. A. Eppes, J. M. Holland, H. R. Kuehler and P. D. Steensma, "Optical fiber transmission system demonstration over 32 km with repeaters data rate transparent Up to 2.3 Mbits/s," *IEEE Trans. Commun*, vol. COM-26, pp. 1045-1055, 1978.

[6] M. Horiguchi and H. Osanai, "Zero material dispersion in optical fibers," *Electron. Lett.*, vol. 11, pp. 8-9, 1975.

[7] D. N. Pane and W. A. Gambling, "Spectral losses of low-OH content optical fibers," *Electron. Lett.*, vol. 12, pp. 310-311, 1976.

[8] J. J. Hsieh, J. A. Rossi and J. P. Donnelly, "Room temperature cw operation of GaInAsP/InP double-heterostructure diode lasers emitting at 1.3 μm," *Appl. Phys. Lett.*, vol. 28, pp. 709-711, 1976.

[9] K. Oe, S. Ando and K. Sugiyama, "1.3 μm cw operation of GaInAsP/InP DH lasers at room temperature," *Jpn. J. Appl. Phys.*, vol. 16, pp. 1273-1274, 1977.

[10] T. Izawa, S. Kobayashi, S. Sudo and F. Hanawa, "Continuous fabrication of high silica fiber preforms," *Integrated Optics and Optical Commu. (IOOC)*, C1-1, Tokyo, 1977.

[11] T. Miya, Y. Terunuma, H. Hosaka and T. Miyashita, "Ultimate low-loss single-mode fiber at 1.55 μm," *Electron. Lett.*, vol. 15, pp. 106-108, 1979.

[12] L. G. Cohen, C. Lin and W. G. French, "Tailoring zero chromatic dispersion into 1.5-1.6 μm low-loss spectral region of single-mode fibers," *Electron. Lett.*, vol. 15, pp. 334-335, 1979.

[13] H. Tsuchiya and N. Imoto, "Dispersion-free single-mode fibers in 1.5 μm wavelength region," *Electron. Lett.*, vol. 15, pp. 476, 1979.

[14] S. Akiba, K. Sakai, Y. Matsushita and T. Yamamoto, "Room temperature CW operation of InGaAsP/InP heterostructure lasers emitting at 1.56 μm," *Electron. Lett.*, vol. 15, pp. 606-607, 1979.

[15] H. Kawaguchi, K. Takahei, Y. Toyoshima, H. Nagai and G. Iwane, "Room-temperature CW operation of InP/InGaAsP/InP double heterostructure diode lasers emitting at 1.55 μm," *Electron. Lett.*, vol. 15, pp. 669-670, 1979.

[16] S. Arai, M. Asada, Y. Suematsu and Y. Itaya, "Room-temperature CW operation of GaInAsP/InP DH laser emitting at 1.51 μm," *Jpn. J. Appl. Phys.*, vol. 18, pp. 2333-2334, 1979.

[17] T. Matsuoka, H. Nagai, Y. Itaya, Y. Noguchi, Y. Suzuki and T. Ikegami, "CW operation of DFB-BH GaInAsP/InP lasers in 1.5 μm wavelength region" *Electron. Lett.*, vol. 18, pp. 27-28, 1982.

[18] K. Utaka, K. Kobayashi, K. Kishino and Y. Suematsu, "1.5-1.6 μm GaInAsP/InP integrated twin-guide lasers with first-odrer distributed Bragg reflectors," *Electron. Lett.*, vol. 16, pp. 455-456, 1980.

[19] C. J. Koester and E. Snitzer, "Amplification in a fiber laser," *Appl. Opt.*, vol. 3, pp. 1182, 1964.

[20] K. Iwatsuki, K. Suzuki, S. Nishi and M. Saruwatari, "80 Gb/s optical transmission over 80 km with time/polarization division multiplexing," *IEEE Photon. Technol. Lett.*, vol. 5, pp. 245-247, 1993.

[21] S. B. Poole, D. N. Payne and M. E. Fermann, "Fabrication of low-loss optical fibers containing rare-earth ions," *Electron. Lett.*, vol. 21, pp. 737-738, 1985.

[22] L. Reekie, I. M. Jauncey, S. B. Poole and D. N. Payne, "Diode-laser-pumped operation of Er^{3+}-doped single-mode fiber laser," *Electron. Lett.*, vol. 23, pp. 1076-1078, 1987.

[23] R. J. Mears, L. Reekie, S. B. Poole and D. N. Payne, "Low noise erbium-doped fiber amplifier operating at 1.54 μm," *Electron. Lett.*, vol. 23, pp. 1026-1028, 1987.

[24] K. Hagimoto, K. Iwatsuki, A. Takada, M. Nakazawa, M. Saruwatari, K. Aida, K. Nakagawa and M. Horiguchi, "A 212 km non-repeated transmission experiment at 1.8 Gb/s using Er^{3+}-doped fiber amplifier in an IM/direct-detection repeater system," *Optical Fiber Commu. (OFC)*, PD-15, 1989.

[25] K. Sato, "Advances in transport technologies-photonic networks, ATM, and SDH," Artech House, Norwood, MA, 1996.

[26] K. Hagimoto, Y. Kobayashi and Y. Yanabayashi, "Multi-gigabit-per-second optical transmission system," *Integrated Optics and Optical Commu. (IOOC)*, WC1-1, 1995.

[27] K. Hagimoto, M. Yoneyama, A. Sano, A. Hirano, T. Kataoka, T. Otsuji, K. Sato and K. Noguchi, "Limitation and challenges of single-carrier full 40-Gbit/s repeater system based on optical equalization and new circuit design," *Optical Fiber Commu., (OFC)*, , 1997.

[28] E. Sano, "Electron device technologies for high-speed lightwave communication systems," *IEICE, Technical Report of IEICE*, OCS97-41, ED97-131, OPE97-86, LQE97-86, 1997.

[29] N. A. Olsson, J. Hegarty, R. A. Logan, L. F. Johnson, K. L. Walker, L. G. Cohen, B. L. Kasper and J. C. Campbell, "68.3 km transmission with 1.37 Tbit・km/s capacity using wavelength division multiplexing of ten single-frequency lasers at 1.5 μm," *Electron. Lett.*, vol. 21, pp. 105-106, 1985.

[30] H. Onaka, H. Miyata, G. Ishikawa, K. Otsuka, H. Ooi, Y. Kai, S. Kinoshita, M. Seino, H. Nishimoto and T. Chikama, "1.1 Tbit/s WDM transmission 150 km 1.3 μm zero-dispersion of single-mode fibers," *Optical Fiber Commu., (OFC)*, San Jose, PD-19, 1996.

[31] A. H. Gnauck, R. W. Tkach, F. Forghieri, R. M. Derosier, A. R. McCormick, A. R. Chraplyvy, J. L. Zyskind, J. W. Sulhoff, A. J. Lucero, Y. Sun, R. M. Jobson and C. Wolf, "One terabit/s transmission experiment," *Optical Fiber Commu., (OFC)*, San Jose, PD-20, 1996.

[32] T. Morioka, H. Takara, S. Kawanishi, O. Kamatani, K. Takiguchi, K. Uchiyama, M. Saruwatari, H. Takahashi, M. Yamada, T. Kanamori and H. Ono, "1 Tbit/s (100 Gbit/s × 10 channel) OTDM/WDM transmission using a single supercontinuum WDM source," *Optical Fiber Commu., (OFC)*, San Jose, PD-21, 1996.

[33] Y. Yano, T. Ono, K. Fukuchi, T. Ito, H. Yamazaki, M. Yamaguchi and K. Emura "2.6 Terabit/s WDM transmission experiment using optical duobinary coding," *European Conf. on Optical Commu., (ECOC)*, Oslo, Norway, ThB3.1, 1996.

[34] J. C. Simon, "GaInAsP semiconductor laser amplifiers for single-mode fiber communications," *IEEE J. of Lightwave Technol.*, vol. LT-5, pp. 1286, 1987.

[35] T. Saito and T. Mukai, "Recent progress in semiconductor laser amplifiers," *IEEE J. of Lightwave Technol.*, vol. LT-6, pp. 1656, 1988.

[36] N. A. Olsson, "Lightwave systems with optical amplifiers," *IEEE J. of Lightwave Technol.*, vol. LT-7, pp. 1071, 1989.

[37] C. J. Koester and E. Snitzer, "Amplification in a fiber laser," *Appl. Opt.*, vol. 3, pp. 1182, 1964.

[38] J. M. Hegarty, M. Broer, B. Golding, J. R. Simpson and J. B. MacChesney, "Photon echoes below 1 K in a Nd^{3+}-doped glass fiber," *Phys. Lev. Lett.*, vol. 51, pp. 2033, 1983.

[39] S. B. Poole, D. N. Payne, R. J. Mears, M. E. Fermann and R. I. Laming "Fabrication and characterization of low-loss optical fibers containing rare-earth ions," *IEEE J. of Lightwave Technol.*, vol. LT-4, pp. 870, 1986.

[40] L. Reekie, R. J. Mears, S. B. Poole and D. N. Payne, "Tunable single-mode fiber lasers," *Electron. Lett.*, vol. 23, pp. 1076-1078, 1987.

[41] M. Ikeda, "Stimulated Raman amplification characteristics in long span single-mode silica fibers," *Optic Comm.*, vol. 39, pp. 148, 1981.

[42] P. Urquhart, "Review of rare earth doped fiber lasers and amplifiers," *IEE Proc.*, vol. 135, pp. 385, 1988.

[43] Y. Miyajiam, T. Komukai and K. Sugawa, "1.31-1.36 μm optical amplification in Nd^{3+}-doped flourozirconate fiber," *Electron. Lett.*, vol. 26, pp. 194, 1990.

[44] J. E. Pedersen and M. Brierley, "High saturation output power from a neodymium-doped fluoride fiber amplification operating in the 1300 nm telecommunication window," *Electron. Lett.*, vol. 26, pp. 819, 1990.

[45] R. Reisfield and Y. Eckstein, "Dependence of spontaneous emission and nonradiative relaxation of Tm^{3+} and Er^{3+} on glass host and temperature" *J. of Chem. Phys.*, vol. 63, pp. 4001, 1975.

[46] W. J. Gignac, J. S. Major, Jr, W. E. Plano, D. W. Nam, D. F. Welch and D. Scifres, "High power InGaAs/GaAs singlemode laser diodes suitable for pumping Pr^{3+}-doped fluoride fiber optic amplifier," *Electron. Lett.*, vol. 28, pp. 1232-1233, 1992.

[47] R. I. Laming, S. B. Poole and J. Tarbox, "Pump excited-state absorption in erbium-doped fibers," *Optic Lett.*, vol. 13, pp. 1084-1086, 1988.

[48] K. Suzuki, Y. Kimura and M. Nakazawa, "High gain Er^{3+}-doped optical fiber amplifier pumped at 800 nm band," *Appl. Phys. Lett.*, vol. 26, pp. 948, 1990.

[49] R. S. Vodhanel, R. I. Laming, V. Shah, L Curtis, D. P. Bour, W. L. Barnes, J. D. Minelly, J. Tarbox and F. J. Favire, "Highly efficient 978 nm dioded-pumped erbium-doped fiber amplifier with 24 dB gain," *Electron. Lett.*, vol. 25, pp.1386, 1989.

[50] M. Nakazawa, Y. Kimura, and K. Suzuki, "Efficient Er^{3+}-doped optical fiber amplifier pumped by a 1.48 μm InGaAsP laser diode," *Appl. Phys. Lett.*, vol. 54, pp. 295, 1989.

[51] M. Nakazawa, Y. Kimura, and K. Suzuki, "Ultra-efficient erbium-doped fiber amplifier," *Appl. Phys. Lett.*, vol. 57, pp. 2635-2637, 1990.

[52] M. Shimizu, M. Yamada, T. Takeshita, M. Horiguchi and M. Okayasu, "Erbium-doped fiber amplifier with an extremely high gain coefficient of 11.0 dB/mW," *Electron. Lett.*, vol. 26, pp. 1641-1643, 1990.

[53] E. Desurvire, "Spectral noise figure of Er^{3+}-doped fiber amplifiers," *IEEE Photon. Technol. Lett.*, vol. 2, pp. 208-210, 1990.

[54] E. Desurvire, "Analysis of noise figure spectral distribution in of erbium-doped fiber amplifiers pumped near 980 and 1480 nm ," *Appl. Phys. Lett.*, vol. 54, pp. 295, 1989.

[55] R. I. Laming and D. N. Payne, "Noise characteristics of erbium-doped fiber amplifiers pumped at 980 nm," *IEEE Photon. Technol. Lett.*, vol. 2, pp. 418-421, 1990.

[56] C. R. Giles, E. Desurvire, J. L. Zyskind and J. R. Simpson, "Noise performance of erbium-doped fiber amplifiers pumped at 1.49 μm, and application to signal preamplification at 1.8 Gb/s," *IEEE Photon. Technol. Lett.*, vol. 1, pp. 367-369, 1990.

[57] M. Yamada, M. Shimizu, M. Okayasu and M. Horiguchi, "Temperature insenstive Er^{3+}-doped optical fiber amplifiers," *Top. Meet. Opt. Amp.*, Pdp 7, 1990.

[58] C. R. Giles, T. Erdogant and V. Mizarhi, "Reflection-induced changes in the optical spectra of 980 nm QW lasers," *IEEE Photon. Technol. Lett.*, vol. 6, pp. 903-904, 1994.

[59] B. F. Vertrudo, G. A. Rogers, G. S. Lick, D. Hargreaves and T. N. Demayo, "Wavelength and intensity stabilization of 980 nm diode laser coupled to fibre Bragg gratings," *Electron. Lett.*, vol. 30, pp. 2147-2149, 1994.

[60] W. T. Tsang, "Extremely low threshold (AlGa)As modified multiquantum well heterostructure lasers brown by molecular-beam epitaxy," *Appl. Phys. Lett.*, vol. 39, pp. 786-788, 1981.

[61] N. Chand, N. K. Dutta, S. N. G. Chu, W. S. Hobson, J. Lopata and R. Wetzel, "Fabrication, performance, and reliability of strained QW lasers," in *Fiber Optic Components and Reliability*, P. M. Kopera and D. K. Paul, Ed., Proc. *SPIE 1580*, D-2, pp. 22-33, 1992.

[62] D. P. Bour, D. B. Gilbert, K. B. Fabian, J. P. Bednarz and M. Ettenberg, "Low degradation rate in strained InGaAs/GaAs single quantum well lasers," *IEEE Photonic Technol. Lett.*, vol. 2, pp. 173-175, 1990.

[63] R. G. Waters, D. P. Bour, S. L. Yellen and N. F. Ruggieri, "Inhibited dark-line defect formation in strained InGaAs/AlGaAs QW lasers," *IEEE Photonic Technol. Lett.*, vol. 2, pp. 531-533, 1990.

[64] R. G. Waters, R. L. Dalby, J. A. Baumann, J. L. De Sanctis and A. H. Shepard, "Dark-line-resistant diode laser at 0.8 μm comprising InAlGaAs strained quantum well," *IEEE Photonic Technol. Lett.*, vol. 3, pp. 409-411, 1991.

[65] S. E. Fischer, R. G. Waters, D. Fekete, J. M. Ballantyne, Y. C. Chen and B. A. Solz, "Long-lived InGaAs quantum well lasers," *Appl. Phys. Lett.*, vol. 54, pp. 1861-1862, 1989.

[66] Spectra Diode Lab. Inc., U.S.A..

[67] Laser Enterprise Inc., Switzerland.

[68] M. Fukuda, M. Okayasu, J. Temmyo and J. Nakano, "Degradation behavior of 0.98 μm strained quantum well InGaAs/AlGaAs lasers under high-power operation," *IEEE J.Quantum Electron.*, vol. 30, pp. 471-476, 1994.

[69] J. R. Lothian, J. M. Kuo, F. Ren and S. J. Pearton, "Plasma and wet chemical etching of InGaP," *Electron Mater.*, vol. 21, pp. 441-445, 1992.

[70] J. M. Olson, R. K. Ahrenkiel, D. J. Dunlavy, Brian Keyes and A.E. Kibber, "Ultralow recombination velocity at $Ga_{0.5}In_{0.5}P$/GaAs heterointerfaces," *Appl. Phys. Lett.*, vol. 55, pp. 1208-1210, 1990.

[71] S. H. Groves, Z. L. Liau, S. C. Palmateer and J. N. Walpole, "GaInP mass transport and GaInP/GaAs buried-heterostructure lasers," *Appl. Phys. Lett.*, vol. 56, pp. 312-314, 1990.

[72] Y. K. Shin, H. Horikawa, K. Yamada and T. Kamijoh, "InGaAs-GaAs-InGaP channel guide strained QW lasers with output powers 300 mW," "InGaAs/GaAs/InGaP MQW lasers by gas source MBE," *Electron. Lett.*, vol. 28, pp. 1234-1235, 1992.

[73] C. R. Abernathy, F. Ren, P. W. Wisk, S. J. Pearton and R. Esagui, "Improved performance of carbon-doped GaAs base heterojunction bipolar transistor through the use of InGaP," *Appl. Phys. Letters*, vol.61, pp. 1092-1094, 1992.

[74] Z. L. Liau, S. C. Palmateer, S. H. Groves, J. N. Walpole and L. J. Missaggia, "Low-threshold InGaAs strained-layer quantum-well lasers (λ=0.98 μm) with GaInP cladding layers and mass-transported buried heterostructure," *Appl. Phys. Lett.*, vol. 60, pp. 6-8, 1992.

[75] T. Ijichi, M. Ohkubo, N. Matsumoto and H. Okamoto, "High power CW operation of aluminum-free InGaAs/GaAs/InGaP strained layer single quantum well ridge waveguide lasers," *12th IEEE Int. Semiconductor Laser Conf.*, Davos, Switzerland, D-2, pp. 44-45, 1990.

[76] J. -M. Kuo, Y. K. Chen and M. C. Wu, "InGaAs/GaAs/InGaP MQW lasers by gas source MBE," *Appl. Phys. Lett.*, vol. 59, pp. 2781-2783, 1991.

[77] Y. K. Chen, M. C. Wu, J. M. Kuo, M. A. Chin and A. M. Sergent, "Self-aligned InGaAs/GaAs/InGaP quantum well lasers prepared by gas-source molecular beam epitaxy with two growth steps," *Appl. Phys. Lett.*, vol. 59, pp. 2929-2931, 1991.

[78] R. M. Kapre, W. T. Tsang, Y. K. Chen, M. C. Wu, M. A. Chin and F. S. Choa, "CBE of GaInP on GaAs (100) substrates and its application to 0.98 μm lasers," *J. Crystal Growth*, vol. 124, pp. 176-180, 1992.

[79] M. Sagawa, K. Hiramoto, T. Tsuchiya, S. Tsuji and K. Uomi, "Advantages of InGaAsP separate confinement layer in 0.98 μm InGaAs/GaAs/InGaP strained DQW lasers for high power operation at high temperature," *Electron. Lett.*, vol. 28, pp. 1639-1640, 1992.

[80] M. C. Wang, D. M. Hwang, P. S. D. Lin, L. Dechiaro, C. E. Zah, S. Ovadia and T. P. Lee, "Facet degradation of aged strained quantum-well lasers studied by high-voltage electron-beam-induced current," *Appl. Phys. Lett.*, vol. 64, pp. 3145-3147, 1994.

[81] S. L. Yellen, A. H. Shepard, C. M. Harding, J. A. Baumann, R. G. Waters, D. Z. Garbuzov, V. Pjataev, V. Kochergin and P. S. Zory, "Dark-line-resistant, aluminum-free diode laser at 0.8 μm," *IEEE Photonic Technol. Lett.*, vol. 3, pp. 409-411, 1991.

[82] H. Kawai, T. Kobayashi, F. Nakamura and K. Taira, "Npn and Pnp heterojunction bipolar transistors grown by MOCVD," *Electron. Lett.*, vol. 2, pp. 609-610, 1989.

[83] M. Ohkubo, A. Iketani, T. Ijichi and T. Kikuta, "InGaAs/InP double-heterojunction bipolar transistors with step graded InGaAsP between InGaAs base and InP collector grown by metalorganic chemical vapor deposition," *Appl. Phys. Lett.*, vol. 59, pp. 2697-2699, 1991.

[84] M. G. Young, U. Koren, B. I. Miller, G. Raybon and C. A. Burrus, "InGaAs/GaAs 0.98 μm semi-insulating blocked planar buried heterostructure lasers employing InGaAsP cladding layers," *IEEE Photonic Technol. Lett.*, vol. 4, pp. 116-118, 1990.

[85] H. Hirayama, Y. Miyake and M. Asada, "Analysis of injection efficiency of separate-confinement-heterostructure quantum-film Lasers," *IEEE J. Quantum Electron.*, vol. 28, pp. 68-74, 1992.

[86] S. Ishikawa, K. Fukagai, H. Chiba, T. Miyazaki and K. Endo, "0.98-1.02 μm strained InGaAs/AlGaAs double quantum-well high-power lasers with GaInP buried waveguides," *IEEE J. Quantum Electron.*, vol. 29, no. 6, pp. 1936-1942, 1993.

[87] M. A. Afromowitz, "Thermal conductivity of $Al_{1-X}Ga_XAs$," *J. Appl. Phys.*, vol. 44, pp. 1290-1295, 1973.

Chapter 2

Design Consideration of Graded-InGaAsP Structures

This chapter deals with the InGaP/InGaAsP/GaAs system, in light of the band lineup. The findings enable me to clarify the advantages of graded-InGaAsP structures to reduce hetero-interface spikes in heterojunction. A unique advantage comes up for discussion, i.e., a change in bandgap forms an electric field that concentrates carriers in a quantum well active region.

2.1 Requirements of High-Power Lasers

EDFAs can more or less unload a repeater composed of electronic circuits. However, pumping semiconductor lasers are required to perform in high-power operation with high-reliability, so as to pump up Er ions onto an upper level. A Substantial optical gain in an EDFA results from dozens mW of optical power charged into Er-doped fiber. Moreover, a booster amplifier needs an optical input-power of at least 200 mW.

Figure 2-1 shows a typical high-power operation of a semiconductor laser, over against electrical to optical power conversion efficiency. An electrical to optical power conversion efficiency η is convenient figure-of merit for estimating high-power lasers, and defined as:

$$\eta=\frac{P_{out}}{P_{in}}, \tag{2.1}$$

$$P_{in}=I_f V_f, \tag{2.2}$$

where P_{in} and P_{out} are electrical input-power and optical output-power, I_f and V_f are operating current and applied voltage. As a general rule, the voltage drop in a laser forms across the semiconductor heterojunction. Reduction of excess voltage on the heterojunction is remarkably at issue in case of high-power operation of a laser, as Section 2.3.1 details.

An active layer and waveguide layers in a semiconductor laser incur self-absorption of light energy, thereby raising the laser in temperature — called self-heating. Any temperature increase in a laser decreases its external differential quantum efficiency. As a result, the electrical to optical power conversion efficiency decreases as the operating current of the laser increases (see Fig. 2-1). External differential quantum efficiency η_d is expressed as:

$$\eta_d = \eta_i \frac{\alpha_m}{\alpha_m + \alpha_i}, \qquad (2\text{-}3)$$

where η_i, α_i and α_m is internal differential quantum efficiency, internal loss and mirror loss. The decrease of an external differential quantum efficiency can be moderated, especially where the internal differential quantum efficiency and internal loss are less dependent on temperature — crucial factors as Section 2.3.2 details.

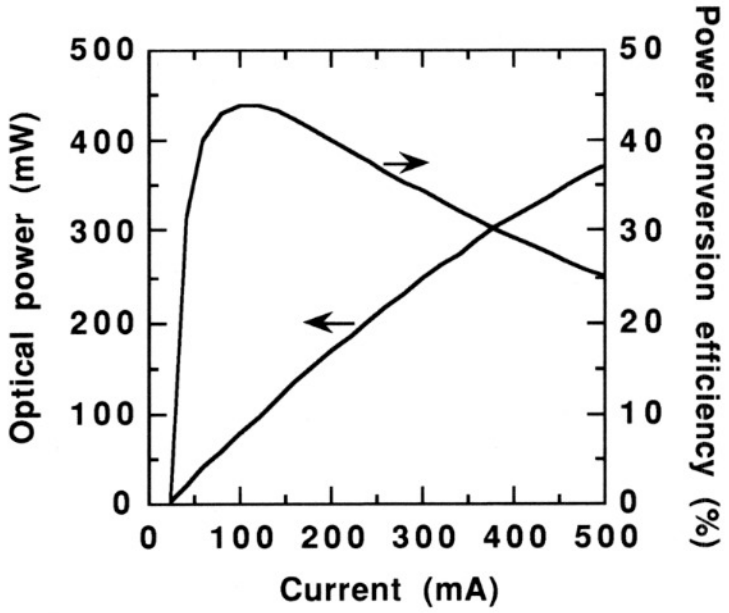

Fig. 2-1. High-power operation of semiconductor laser with electrical to optical power conversion efficiency.

2.2 Characterization of Band Discontinuity of InGaP/InGaAsP/GaAs System

2.2.1 Band Discontinuity of InGaP/GaAs

It is a major premise required by design work for semiconductor devices, to have a grip on the discontinuity in the conduction or valence band at a heterointerface. In the recent two decades, a number of semiquantitative approaches have been proposed to theorize the band edge discontinuity. Harrison's Linear Combination Atomic Orbital (LCAO) model [1] and Anderson's electron affinity rule model [2] have been used for binary alloys, among other ones.

As for the Harrison's model, the valence band maxima are calculated for a bulk semiconductor, in accordance with the LCAO approach. The valence band maximum for a semiconductor is given by:

$$E_v=\frac{1}{2}(e^c+e^a)-\sqrt{\frac{1}{4}(e^c-e^a)^2+V_{xx}^2}, \qquad (2\text{-}4)$$

where e^c and e^a are the p-atomic energy states of the anion and cation of semiconductors. The term V_{xx} is interatomic matrix element, defined as:

$$V_{xx}=\frac{b}{d^2}, \qquad (2\text{-}5)$$

where b is a constant detrained by fitting the values to the theoretical bands of the two semiconductors, and d is the interatomic distance. The valence band discontinuity is defined as:

$$\Delta E_v=E_v^1-E_v^2, \qquad (2\text{-}6)$$

where E_v1 and E_v2 are the calculated valence band maxima of the two semiconductors 1 and 2.

As for Anderson's model, conduction band discontinuity can be represented by the difference in electron affinity between two semiconductors with heterojunctions:

$$\Delta E_c=\chi_1-\chi_2, \qquad (2\text{-}7)$$

where χ_1 and χ_1 are the electron affinities of the two semiconductors 1 and 2.

Figure 2-2 shows the calculated band lineup of InGaP/GaAs heterojunctions with the aide of both models. A ratio of 0.5 results from 'conduction to valence' in band

discontinuity, where Harrison's model is applied. Meanwhile, the Anderson's model indicates a type II heterojunction.

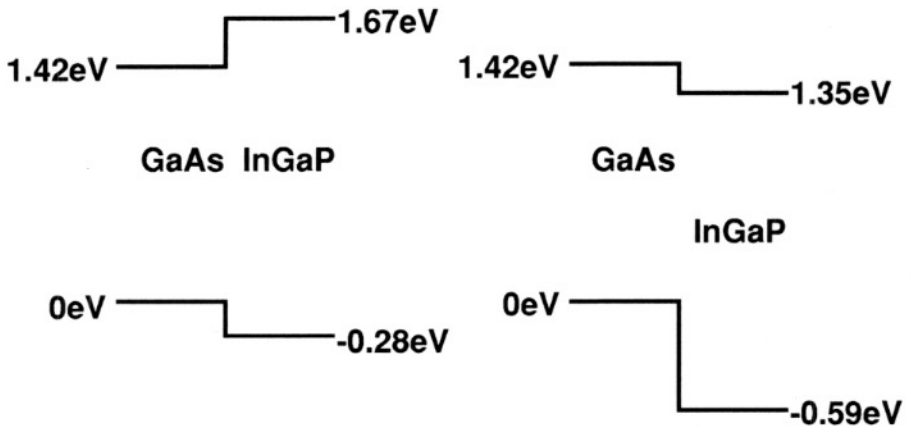

(a) Harrison's model [1]. (b) Anderson's model [2].

Fig. 2-2. Calculated band lineup of InGaP/GaAs heterojunction.

As if demonstrating what is described above, several reported papers concur in describing a mass of measured disagreement: conduction band discontinuity ΔE_C across an InGaP/GaAs heterojunction. A Capacitance-Voltage profiling method was repeated to yield ΔE_C=0.22 eV [3] and ΔE_C=0.19 eV [4]; a deep-level transient spectroscopy on quantum wells unveiled ΔE_C=0.198 eV [5]; a photoemission measurement resulted in ΔE_C =0.108 eV [6]. On the contrary, a current-voltage (I-V) measurement of HBTs inferentially pointed to a ΔE_C value of as small as 30 meV [7] at most; a photoluminescence measurement of InGaP/GaAs multiquantum wells as a function of pressure indicated ΔE_C=60 meV [8]. At present, a theoretical calculation linked with a first-principles pseudopotential method deduces that large scatter in the measured ΔE_C as described above, may be attributed to the ordering phenomenon of InGaP [9].

Unfortunately, no report have ever dealt with the band discontinuity of the InGaP/InGaAsP/GaAs system. Consequently, we have no other choice, but to rely on estimation by some instrumental technique. As a transistor-based model of the band discontinuity contains no adjustable parameter (e.g., heterojunction position, interface charge used in the C-V profile method [10]), this method is believed to be a powerful approach for the purpose.

At the outset of the next section, I describe the fabrication of InGaAsP/GaAs and InGaP/GaAs HBTs grown by MOCOD; then, I remark on the band lineup of the InGaP/InGaAsP according to the I-V measurements of those two types of HBTs.

2.2.2 Estimation of Band Discontinuity of InGaP/InGaAsP/GaAs System

In an attempt to model the band discontinuity of InGaP/InGaAsP/GaAs system, two types of epitaxial layers were prepared for emitter-up HBT structures grown onto GaAs substrates with two-step MOCVD (Metal Organic Chemical Vapor Deposition, see Section 3.1.1). Table 2-1(a) refers to one of the two: $In_{0.38}Ga_{0.62}As_{0.22}P_{0.78}$ emitter, Table 2-2(b) refers to the other: $In_{0.49}Ga_{0.51}P$ emitter. The InGaAsP emitter was proven to have a bandgap of 1.77 eV with the room-temperature photoluminescence measurement; the InGaP emitter had the bandgap energy of 1.87 eV. The first growth was carried out at atmospheric pressure [11] for the collector and base layers, and the second growth was at a reduced pressure of 80 Torr for emitter and cap layers. The base layer was 70 nm thick with carbon doped to $p=4\times10^{19}$ cm^{-3}. No spacer layer was prepared at the regrown emitter/base interface. The emitter layers of both the HBTs were 200 nm thick with Si doped to $n=5\times10^{17}$ cm^{-3}.

After epitaxial growth, both the HBT devices were fabricated in the same process, where a wet chemical selective etching process was applied to form emitter mesas, each having a square of 110×110 μm^2. Those devices employed Ti/Au non-alloyed contact to the base layers, and AuGe/Au alloyed contact onto the emitter cap and subcollector layers.

Figures 2-3(a) and 2-3(b) show the I-V characteristics of InGaAsP/GaAs HBT and InGaP/GaAs HBT. The measured current gain of InGaAsP/GaAs HBT was 14 at a collector current density of 700 A/cm^2, being the same as the InGaP/GaAs HBT. The offset voltage of both I-V characteristics were 0.09 V for InGaAsP/GaAs and 0.1 V for InGaP/GaAs.

Table 2-1. Epitaxial layer structure of HBTs.

(a) $In_{0.38}Ga_{0.62}As_{0.22}P_{0.78}$ emitter.

Layer	Material	Thickness (nm)	Doping (cm^{-3})
Cap	n^+-GaAs	100	$>2\times10^{18}$
	n-InGaAsP (Eg=1.57eV)	50	5×10^{17}
Emitter	N-InGaAsP (Eg=1.77eV)	200	3×10^{17}
Base	p^+-GaAs	70	4×10^{19}
Collector	n^--GaAs	500	3×10^{16}
Subcollector	n^+-GaAs	500	$>2\times10^{18}$
Substrate	S.I. GaAs		

(b) $In_{0.49}Ga_{0.51}P$ emitter.

Layer	Material	Thickness (nm)	Doping (cm^{-3})
Cap	n^+-GaAs	100	$>2\times10^{18}$
	n-InGaAsP (Eg=1.57eV)	25	5×10^{17}
	n-InGaAsP (Eg=1.77eV)	25	5×10^{17}
Emitter	N-InGaP (Eg=1.87eV)	200	3×10^{17}
Base	p^+-GaAs	70	4×10^{19}
Collector	n^--GaAs	500	3×10^{16}
Subcollector	n^+-GaAs	500	$>2\times10^{18}$
Substrate	S.I. GaAs		

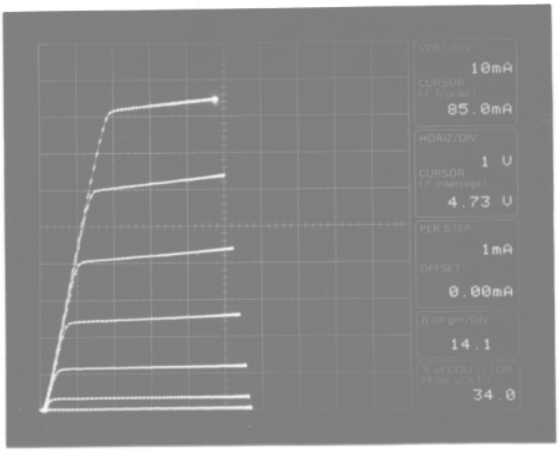

(a) InGaAsP/GaAs HBT.

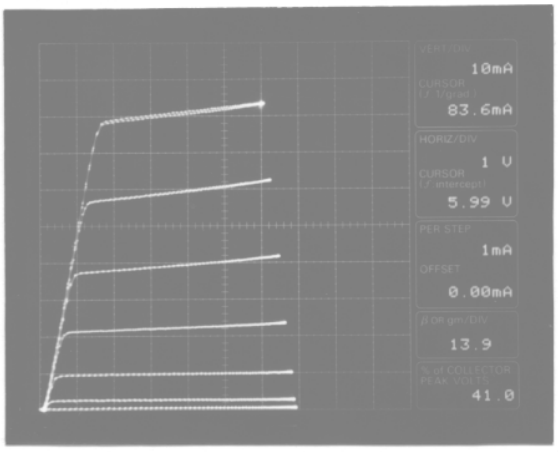

(b) InGaP/GaAs HBT.

Fig. 2-3. I-V characteristics of (a) InGaAsP/GaAs HBT and (b) InGaP/GaAs HBT.

Figure 2-4 shows the Gummel plot of collector current (I_C) for the InGaAsP/GaAs HBT and InGaP/GaAs HBT. The ideality factors 'n' for the HBTs resulted in the same value of 1.06, which is in good agreement with what the classical model of an abrupt heterojunction figures out.

$$n=1+\frac{\varepsilon_E N_E}{\varepsilon_B N_B}, \tag{2.8}$$

where ε_E and ε_B are dielectric constants of emitter and base, and N_E and N_B are carrier densities of emitter and base, respectively. In the course of defining a turn-on voltage with the emitter-base voltage (V_{be}) at a collector current of 6×10^{-6} A, ten devices were examined so as to extract the values of average turn-on voltage and the standard deviation. The average turn-on voltage was 0.955 V for the InGaP/GaAs HBT with a standard deviation of 0.003 V and 0.943 V for the InGaAsP/GaAs HBT and with a standard deviation of 0.002 V. On analysis, the InGaAsP/GaAs HBT is 12 meV less than the InGaP/GaAs HBT in turn-on voltage.

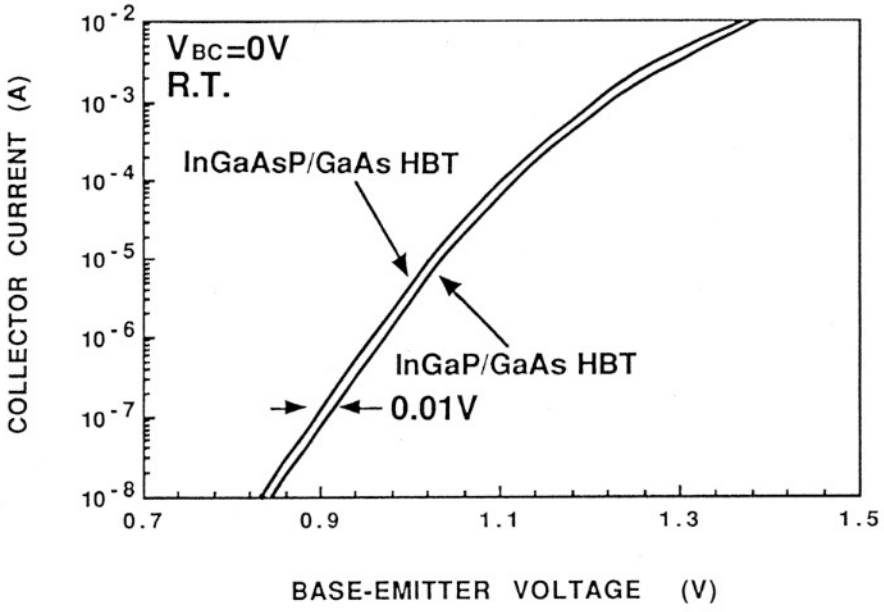

Fig. 2-4 Gummel plot of collector current of HBT.

Figure 2-5 shows schematic band diagram at emitter/base heterojunction. Assuming that thermionic electrons from the emitter are injected into the base and diffuse toward the collector, ΔE_c of the emitter/base heterojunction can be derived from the I_C-V_{be} relation [7], which is given by:

$$\ln(I_C/A^*T^2)=-[Eg(GaAs)-\delta_B+\Delta E_c-V_{be}]/nk_BT, \tag{2.9}$$

where A^* are δ_B the effective Richardson constant and the Fermi level in the base. Eg(GaAs) includes the shrinkage of bandgap energy due to the hole concentration (4×10^{19} cm^{-3}), which is estimated to be 95 meV at 300 K [12]. In this expression, the Fermi level in the emitter is neglected because electron density in the emitter was 5×10^{17} cm^{-3} corresponding to zero condition at room temperature.

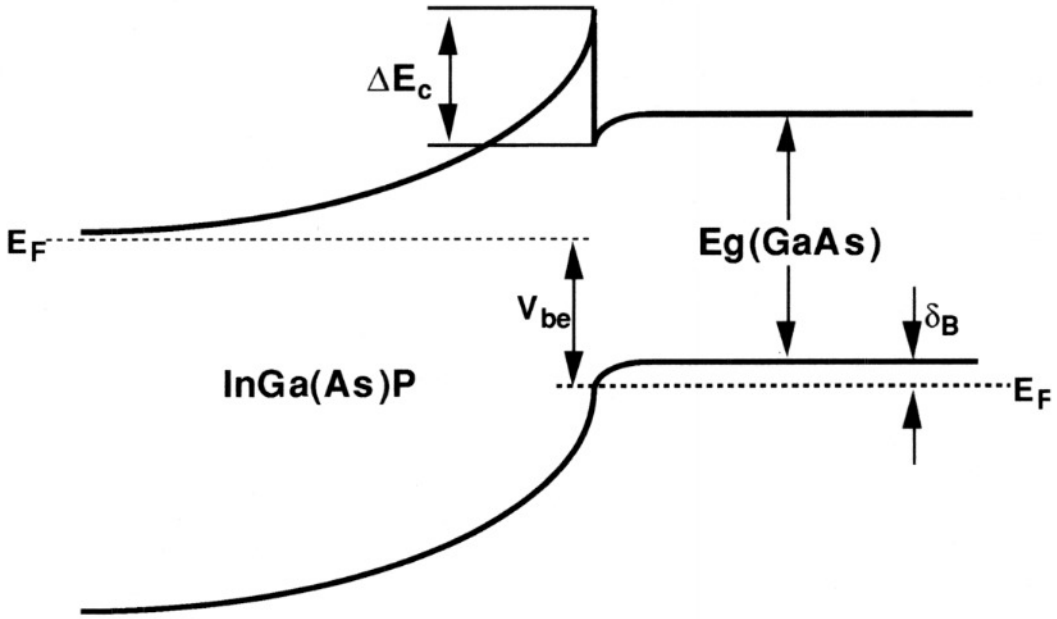

Fig. 2-5. Schematic band diagram at emitter/base heterojunction.

According to expression (2.9), 33 meV of ΔE_c was derived for the InGaP/GaAs heterojunction ($\Delta E_{c,T/B}$) and 18 meV of ΔE_c, of the InGaAsP/GaAs heterojunction ($\Delta E_{c,Q/B}$). The $\Delta E_{c,T/B}$ of 33 meV corresponds well to the data of Ref.7. Moreover, it can be conceived that ΔE_c of InGaP/InGaAsP heterojunction ($\Delta E_{c,T/Q}$) may represent the difference in $\Delta E_{c,T/Q}$ between InGaP/GaAs and InGaAsP/GaAs, as shown in Fig. 2-7. It generalizes down to:

$$\Delta E_{c,T/Q}=\Delta E_{c,T/B}-\Delta E_{c,Q/B}. \qquad (2.10)$$

Accordingly, $\Delta E_{c,T/Q}$ of InGaP/InGaAsP was approximated at 15 meV.

The valence band discontinuity (ΔE_v), is estimated as:

$$\Delta E_v=\Delta Eg-\Delta E_c, \qquad (2.11)$$

where ΔEg is the difference in the bandgap. Here the difference in the bandgap turns clear, thereby enabling me to figure out the valence band discontinuity of a InGaP/InGaAsP/GaAs system as a function of composition of As, which is shown in Fig. 2-7. The solid linear line extrapolates the two lower left plots.

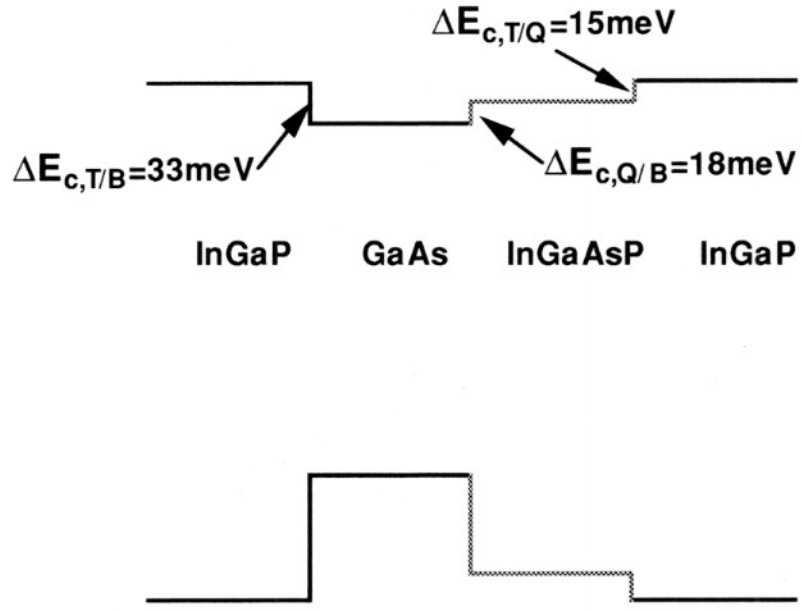

Fig. 2-6. Measured band lineup of InGaP/InGaAsP/GaAs heterojunction.

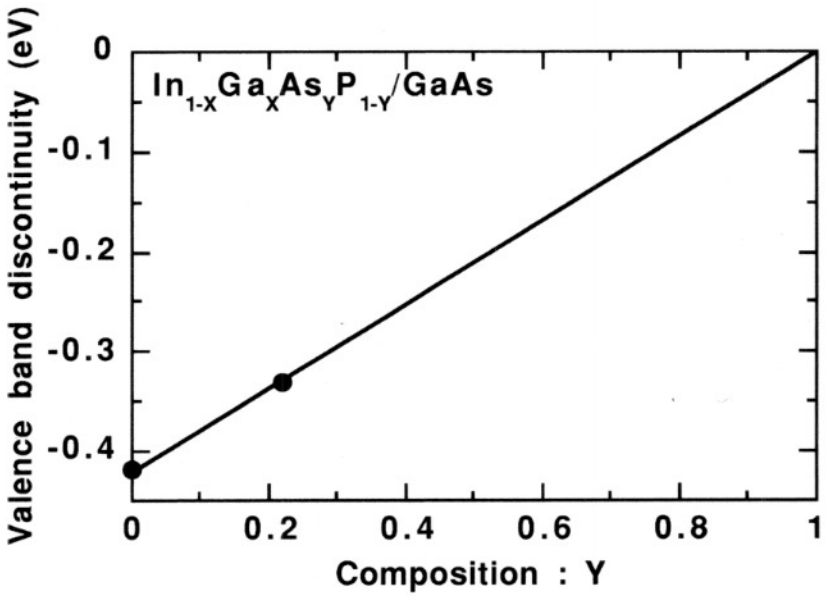

Fig. 2-7. Valence band discontinuity of the InGaP/InGaAsP/GaAs system as a function of composition of As. The solid lines show a fitted linear approximation.

2.3 Design Consideration of Graded-InGaAsP Structures

2.3.1 Reduction of Heterojunction Spikes of InGaP/GaAs

The last section revealed that in the GaAs/InGaAsP/InGaP system, the valence band discontinuity is much larger than the conduction band discontinuity, according to the I-V characteristics of the heterojunction. Here let's give consideration to lasers with an InGaP cladding layers. Listed below are the epitaxial layers [13] of the first demonstration of 980-nm InGaAs/GaAs strained layer single quantum well lasers with InGaP cladding layers.

The layers consist of

i) n-GaAs buffer layer,
ii) n-InGaP cladding layer,
iii) undoped GaAs SCH layer,
iv) strained InGaAs single quantum well active layer,
v) undoped GaAs SCH layer,
vi) p-InGaP cladding layer,
vii) heavily doped p^+-GaAs contact layer.

This structure is likely to allow hole injection to be retarded past two abrupt GaAs/InGaP interfaces (vi/v, vii/vi), where a large valence band spike subsists shown in Fig. 2-8; hole injection needs much applied voltage — leading to even more power-dissipation of the lasers.

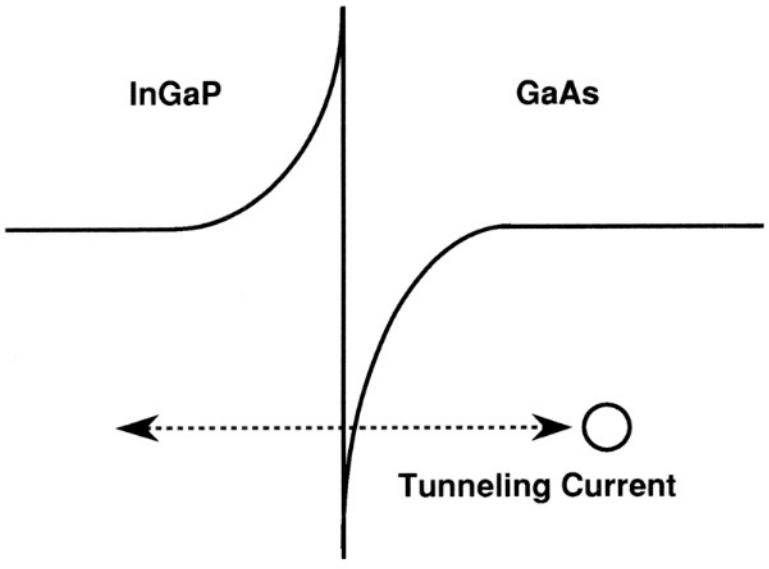

Fig. 2-8. Schematic valence band diagram at p-InGaP/p-GaAs heterojunction.

Over against the drawback, two countermeasures are thinkable: doping control on the periphery of a heterojunction and inserting the grading layers in a hetero-interface. The doping control was demonstrated with success in a mode of modulation doping [14], delta doping [15] or some other doping, on the basis of a GaAs/AlAs heterojunction. Yet absorption loss arose in free carriers, owing to heavy doping near an active layer — degradation of lasing performance. The latter countermeasure can be implemented, by inserting InGaAsP layers in a GaAs/InGaP hetero-interface. It requires unrealistic manipulation to insert a continuous graded-InGaAsP layers between layers of GaAs and InGaP. Then it is no doubt handy to locate a stepped or step-like one, between them, instead.

I show theoretical approach to the I-V characteristics of InGaP/InGaAsP/GaAs heterojunction with various graded-InGaAsP structures, so as to optimize the graded-structures. The calculation was performed by means of a tunneling model [16] in Fig. 2-8, which was proved to be in excellent agreement with the experimental results applied to a GaAs/AlAs heterojunction [17].

The I-V characteristics are calculated based on the transmission probability [18]. Assuming a hole energy E_Z with effective mass m*, which means the longitudinal energy for slanting incidence to the hetero-interface, the current density for each E_Z is given as:

$$J(E_Z)=\frac{4\pi m^* k_B T}{h^3} D(E_Z) \ln\left(\frac{f_2}{f_1}\right), \qquad (2\text{-}12)$$

where $D(E_Z)$ is transmission probability for the energy E_Z, and f_1 are f_2 Fermi-distribution functions for the wide and narrow bandgap material, respectively. For all valence band energy, the current density sums into:

$$J=\int_{-\infty}^{Ev} J(E_Z)dE_Z \qquad (2\text{-}13)$$

Table 2-2 shows the sample of material parameters used in the calculation. Literature have dealt with scarcely any information about InGaAsP materials lattice-matched to GaAs. Therefore, I was forced to have recourse to interpolation means [19, 20], so as to line up all values, required for the integration, which includes mlh, mhh (hole effective mass in the light and heavy hole bands respectively) and ε (static dielectric constant).

Table 2-2. Example of material parameters used in the calculation.

Material	Eg	m_{lh}	m_{hh}	ε
GaAs	1.42	0.074	0.620	13.2
	1.58	0.087	0.703	12.7
InGaAsP	1.65	0.093	0.729	12.6
	1.76	0.102	0.781	12.2
InGaP	1.87	0.113	0.849	11.8

Figure 2-9 plots the J-V curves, which resulted from a p-InGaP/p-GaAs heterojunction, with a varied doping concentration. The homogenous acceptor-doping-concentration was set across the heterojunction. For InGaP cladding lasers, 'forward-bias' denotes the current flow from the InGaP cladding layer to the GaAs active region; 'reverse-bias' denotes the current flow from the GaAs cap layer to the InGaP cladding layer. It is evident that the reverse-bias heterojunction needs to be applied with much higher voltage than the forward-bias heterojunction, But then, it is practical to dope the reverse-bias heterojunction with a high concentration, where absorption loss — free carrier absorption — is designed to lead into zero, considering how to manipulate the optical field distribution.

Should it be desirable to minimize the doping concentration of the forward-bias heterojunction, so as to suppress absorption loss around the active layer, multiple-steps InGaAsP layers will be inserted into the forward-bias heterojunction to reduce the excess bias voltage.

Fig. 2-10 plots dependence of the calculated excess bias voltage on the number of InGaAsP layers. A acceptor doping concentration of 1×10^{18} cm^{-3} was set across the heterojunction; a current density was set at 3.3 kA/cm^2. The total excess bias of a p-InGaP/p-GaAs with multiples of p-InGaAsP layers is calculated from the sum of number of a heterojunction of p-InGaAsP/p-InGaAsP. The excess bias voltage decreases as the number of steps drastically. The voltage drop across a p-InGaP/p-GaAs with three p-InGaAsP layers is negligibly small.

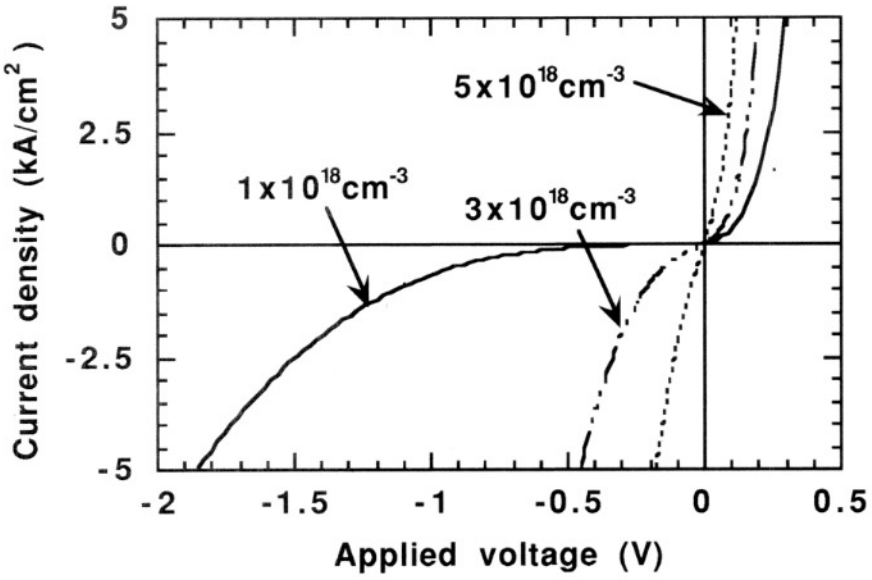

Fig. 2-9. Calculated J-V characteristics of p-InGaP/p-GaAs heterojunction with various doping concentration.

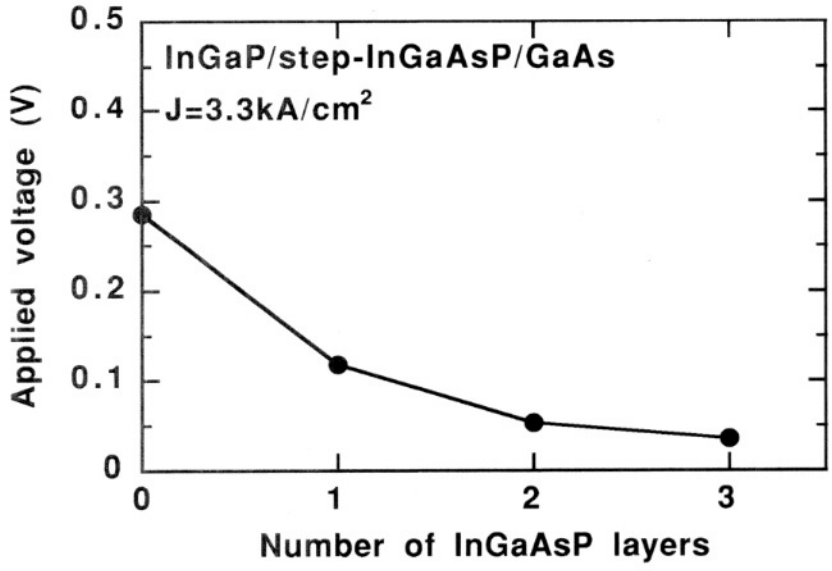

Fig. 2-10. Dependence of the calculated excess bias voltage on the number of steps of InGaAsP layers. Doping concentration is fixed as 1×10^{18} cm^{-3} through the heterojunction.

2.3.2 Formation of Electric Field due to Graded-InGaAsP Structures

The preceding section topicalizes an advantage of the graded-composition structure — suppressing effect on heterojunction spikes. Here I remark on a second advantage: a change of bandgap forms an electric field.

As Fig. 2-11(a) shows, a uniform-structure, with a constant bandgap, has two edges of constant slopes, where forces exerted on electrons and holes are of the same magnitude, but diametrical in polarity. In fact they are quantified with an electrostatic force $\pm qE$ exerted on a charge of magnitude $\pm$q (coulomb) in an electric field E. Now, a graded-structure, with a change of bandgap, has two band edge of which slopes cannot necessarily be of one accord. Nor can they be correlated with any electrostatic force exerted by a electronic field E. Consequently, those slopes could be opposite in gradient and unequal in intensity, as shown in Fig. 2-11(b). Here forces exerted on electrons or holes are formulated as:

$$F_e=-\frac{dE_c}{dz}, \quad F_h=+\frac{dE_v}{dz} \tag{2.14}$$

where E_c and E_v are conduction and valence-band edges. In terms of a p-type graded-bandgap structure as given in Fig. 2-11 (c), the thermodynamical equilibrium state is in flat valence band, where an electron is subjected to a total effective field. The state is expressed:

$$F_e=-\left(\frac{dE_c}{dz}+\frac{dE_v}{dz}\right)=-\frac{dEg}{dz}. \tag{2.15}$$

Thus, we are enabled to control the distribution and flow of electrons and holes, both separately, where adequate coordination is set between a bandgap change (graded-bandgap structure) and impurity doing. It can serve bipolar devices (e.g. lasers, HBTs) in a great capacity.

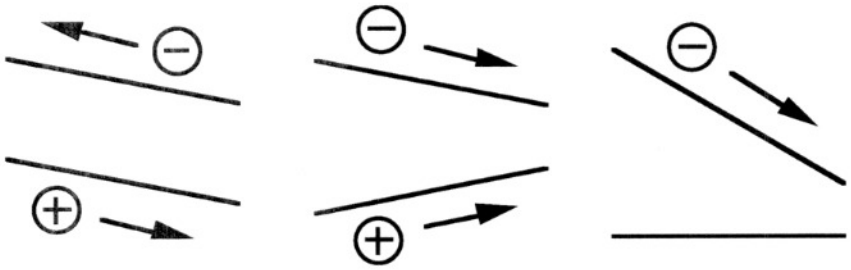

(a) uniform-structure. (b) graded-structure. (c) p-type graded-structure.

Fig. 2-11. Schematic energy band diagram.

The graded-structure can involve a graded base in HBTs [21-23, see appendix A] as one of the most successful application. In a HBT, the majority carrier conductivity flattens the majority carrier quasi-Fermi level effectively across the base, of which bandgap change, in turn, induces gradients in minority carrier energy. These gradients form an electric field that drives carriers injected from the emitter toward the collector, with the result that carriers have their base transit time shortened, for instance.

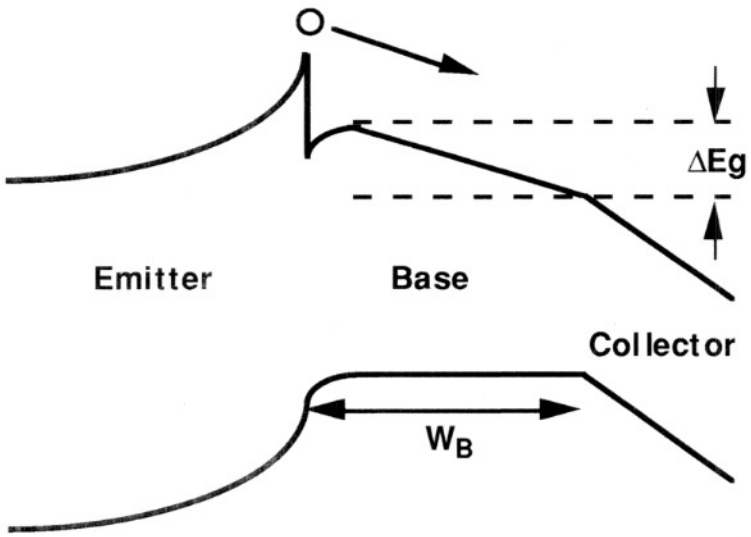

Fig. 2-12. Schematic band diagram of the graded base HBTs.

The graded-bandgap structure application to lasers includes a successful graded-index separate-confinement-heterostructure (GRIN-SCH) for quantum well lasers which are historical instances for an AlGaAs/GaAs system [22] and an InP/InGaAsP system [23]. The GRIN-SCH structure around the active region causes an index change, while the graded-bandgap structure forms an electric field. The latter effect serves to increase the carrier population in the quantum well active layer [24, 25]. Fig. 2-13 shows calculated results of the carrier distribution of a quantum well with an SCH and GRIN-SCH structure, by means of a self-consistent solution of the Poisson equation according to Ref. 24. This diagram shows that the carrier density in the GRIN-SCH layer is much lower than that of SCH layer, where carriers concentrate in the active region in the GRIN-SCH, due to the potential profile by GRIN structure.

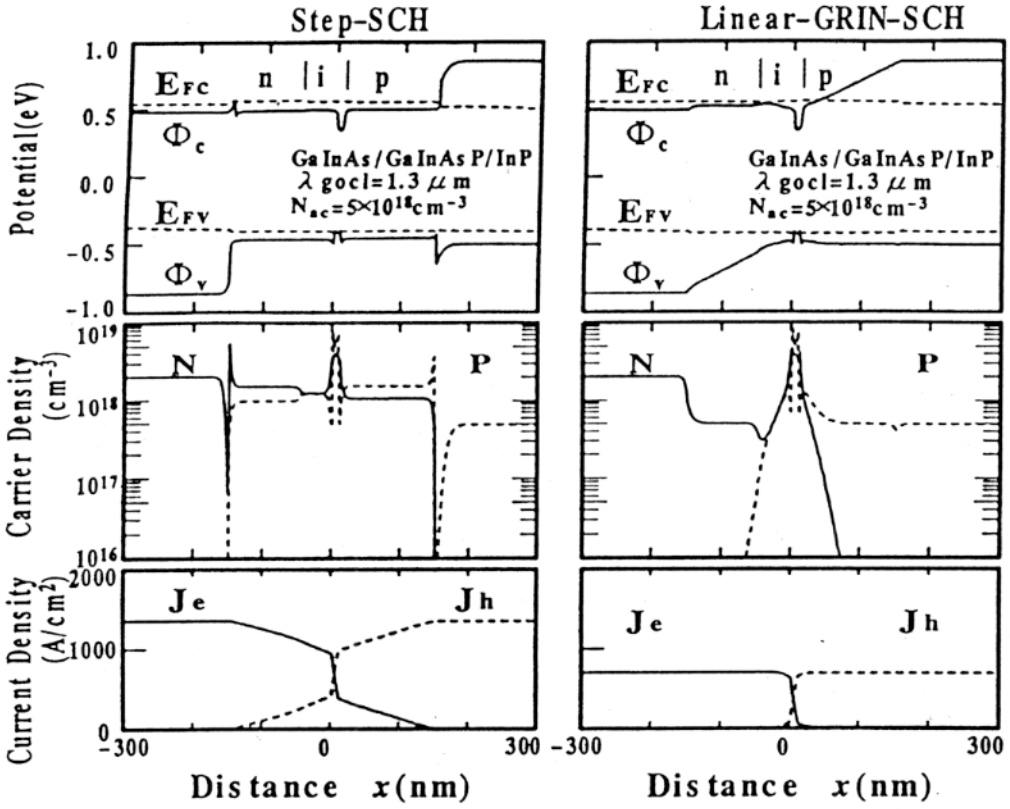

Fig. 2-13. Calculated results of the potential distribution, Fermi level and current density distribution for SCH and GRIN-SCH structure [24].

Now the validity of a GRIN-SCH waveguide around a quantum well comes up for discussion and is characterized by a simplified model as to the temperature dependence of carrier population in lasers [23]. Figure 2-14 shows schematic band diagram of GRIN-SCH lasers. Due to the graded-structure of p-type side, electrons overflowed out of the well may be forced to go back to the quantum well, which enables to improve the temperature characteristics of lasers.

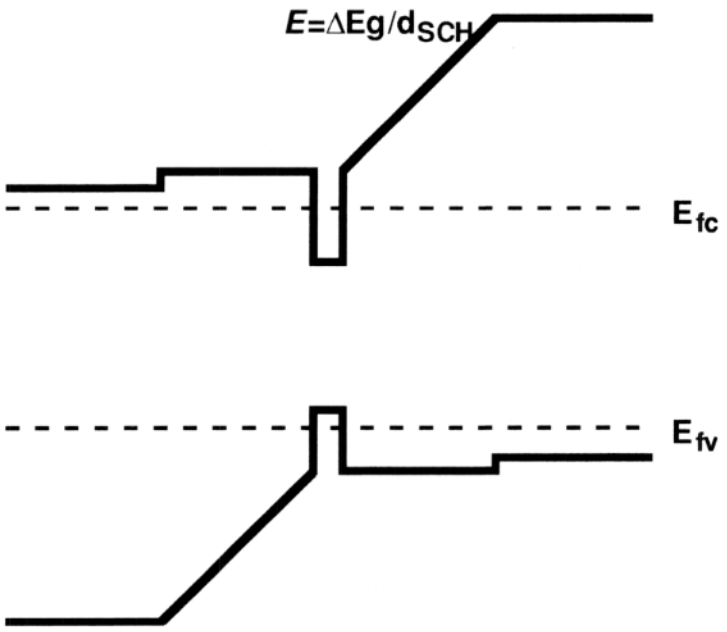

Fig. 2-14. Schematic band diagram of GRIN-SCH lasers.

The carrier density confined to the quantum well, n_{QW} is expressed as follows:

$$n_{QW}=\frac{4\pi m k_B T}{h^2 W_{well}}\sum_j \log\{1+\exp(E_Q+E_F-E_j)/k_B T\}, \qquad (2\text{-}16)$$

where W_{well}, E_Q, E_F and E_j are the thickness of the quantum well, the depth below the bottom of the GRIN layer, the Fermi level and energy eigenvalue in quantum well, and the summation is over the few bound states in the quantum well. On the other hand, When SCH structure have a general forward-bias power-law energy profile:

$$V(x)=\Delta E\left(\frac{|x|}{W_{SCH}}\right)^{\alpha}, \qquad (2\text{-}17)$$

where ΔE and W_{SCH} are energy barrier by SCH structure and a thickness of SCH region. For instance, $\alpha = 1$ indicates a linear grading of bandgap, which is defined as linear-

GRIN-SCH. Carrier density confined in the SCH region, n_{SCH} is expressed as follows:

$$n_{SCH}=\int_0^{\infty}\frac{\rho_\alpha(E)}{\exp\{(E-E_F)/k_BT\}+1}dE$$

,

$$\rho_\alpha(E)=2\left(\frac{4\pi m}{h^2}\right)^{3/2}E^{1/2}\left(\frac{E}{\Delta E}\right)^{1/\alpha}\frac{1}{\alpha}\sqrt{\frac{2}{\pi}}\frac{\Gamma(3/2)\Gamma(1/\alpha)}{\Gamma(3/2+1/\alpha)}, \qquad (2\text{-}18)$$

where Γ is the gamma function.

Figure 2-15 shows the calculated ratio of carrier (electron) population in quantum well as a function of temperature. Virtual values were substituted into the formula: E_Q=0.2 V, E_F=0 eV, E_j=0.1 eV, ΔE=0.45 eV, W_{well} =10 nm, W_{SCH}=80 nm. At lower temperatures, the carrier population ratio of Step-SCH structure shows lowest of the three. But then, carriers overflow out of the quantum well as temperature increases. GRIN-SCH structure, laid out near the quantum well active region, stabilizes the population of electron in there. Consequently, the laser performance turns less dependent on temperature, namely, threshold current density; moreover, linear-GRIN-SCH structure improves the temperature dependence of lasers.

A laser's optical loss α consists of mirror loss and internal loss: $\alpha=\alpha_m+\alpha_i$. Free carriers in a quantum well and a waveguide region induce light absorption. The internal loss arising from free-carrier absorption formulated, neglecting the absorption in the cladding layers:

$$\alpha_i=\sigma_n(\Gamma_{QW}n_{QW}+\Gamma_{SCH}n_{SCH})+\sigma_p(\Gamma_{QW}p_{QW}+\Gamma_{SCH}p_{SCH}), \qquad (2\text{-}19)$$

where Γ_{QW} and Γ_{SCH} are the optical confinement factor in the quantum well and SCH region, and p_{QW} and p_{SCH} indicate the carrier density in quantum well and SCH region. Free electron and hole absorption loss is expressed as σ_n and σ_p.

Figure 2-16 shows normalized $\Gamma_{QW}n_{QW}+\Gamma_{SCH}n_{SCH}$ correlating the internal loss as a function of temperature. The formula involves no effect of absorption loss caused by overflown holes. The internal loss was caused to increase, because the carriers overflowing toward the SCH region increased in population. These results indicate that a laser's temperature-increase decreases its differential quantum efficiency. It can be learned that the linear GRIN-SCH structure is less dependent on temperature in terms of differential quantum efficiency, than the SCH, parabolic GRIN-SCH structure.

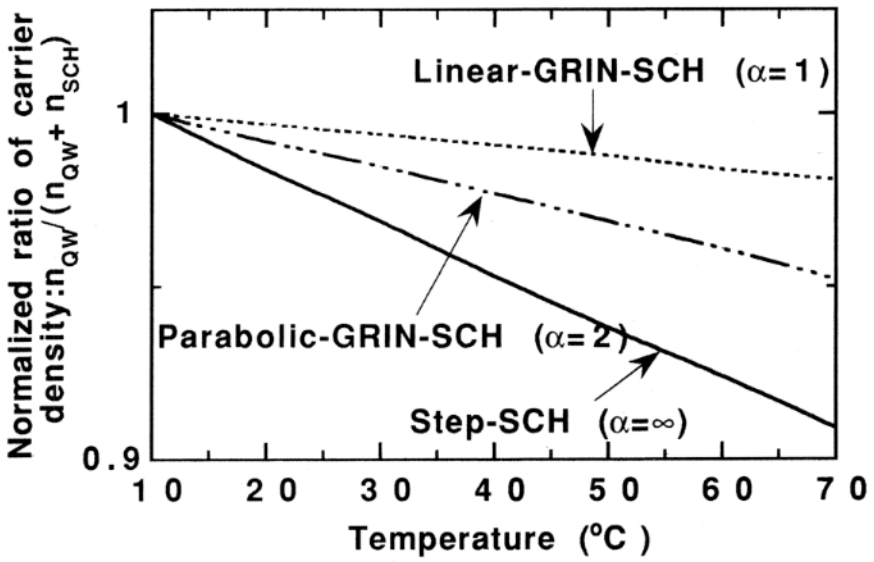

Fig. 2-15. Calculated ratio of the electron population as a function of temperature. n_{QW} and n_{SCH} indicate the carrier density of carrier in quantum well and SCH region.

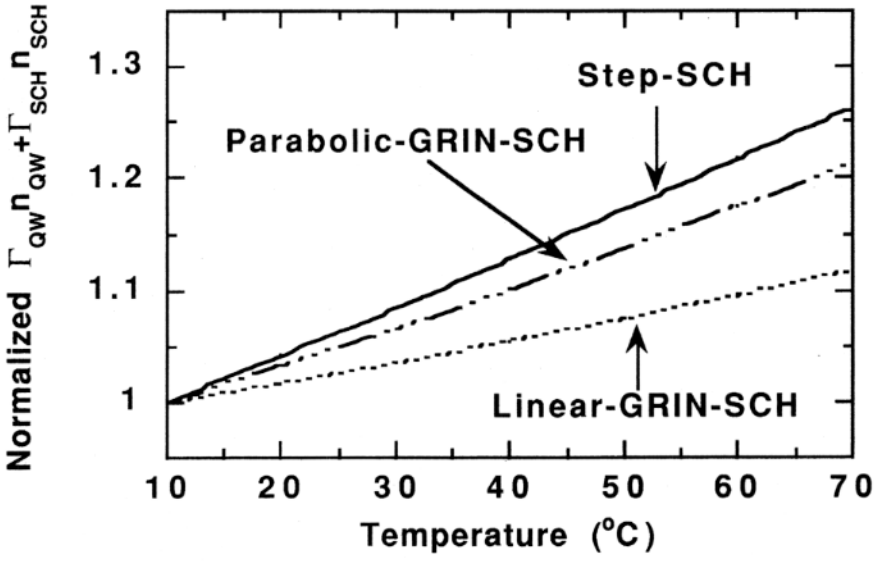

Fig. 2-16. Normalized $\Gamma_{QW}n_{QW}+\Gamma_{SCH}n_{SCH}$ as a function of temperature.

2.4 Summary

The first made clarified from the I-V characteristics of a heterojunction is that conduction band discontinuity was much smaller than valence band discontinuity, in the InGaP/InGaAsP/GaAs system. This finding, which is hindrance to hole injection, is a serious problem to realize practical high-power aluminum-free 980-nm lasers. The intent of this research is to propose a counteraction against the problem: inserting the graded-InGaAsP into a GaAs/InGaP interface, and to show desirable step-like graded-InGaAsP structures to reduce the excess voltage of the InGaP/GaAs heterojunction.

The second made clarified is another advantage of graded-structure that the increasing carrier population in quantum well active layer improves temperature dependence of lasing characteristics.

Appendix A

Graded-GaAsP Base HBTs

Advantages of Graded Base HBTs

Hers let's give consideration about a base of a HBT, having a width of W_B, which is linearly graded from one material with bandgap Eg1 to another with a bandgap Eg2. Electric field exerted on electrons E_{bi} is defined: $E_{bi} = (Eg1 - Eg2)/qW$. The electric field has the advantage of an increased base transport factor, due to reduced recombination of carriers in the base. In case of drift motion due to the electric field is dominant over the electron transport in there, the current gain (β) of the graded-base HBTs can be expressed, assuming a unity emitter injection efficiency, as:

$$\beta = \frac{\alpha}{1-\alpha}$$

$$\alpha = \frac{\exp(\eta)}{\cosh\phi + \frac{\eta}{\phi}\sinh\phi}$$

$$\phi = \left\{(\eta^2 + (W_B/L_e)^2\right\}^{0.5}$$

$$\eta = \frac{q}{2k_BT}E_{bi}W_B \qquad \text{(A-1)}$$

where L_e is minority electron diffusion length in base. The last term denotes a drift motion induced by electric field in graded base, increasing current gain.

The second important advantage is reduction of the base transit time of carriers. Neglecting the diffusion effects, the transit time, τ_b is expressed as:

$$\tau_{b,graded} = \frac{qW_B^2}{\mu(Eg1 - Eg2)} = \frac{qW_B^2}{\mu\Delta Eg}, \qquad \text{(A-2)}$$

where μ is mobility in graded base. Now it carries a significant meaning to compare the above and the diffusion-limited base transit time of a transistor with a uniform (ungraded) base, each being equal in thickness and doping concentration:

$$\tau_{b,uniform} = \frac{W_B^2}{2D}, \qquad \text{(A-3)}$$

where D is the diffusion coefficient for electrons in base. With reference to formula 2-16 and 2-17, and using the Einstein relationship ($D=\mu k_B T/q$), the base transit time can be reduced for a graded base, by the factor:

$$\frac{\tau_{b,graded}}{\tau_{b,uniform}} = \frac{\Delta Eg}{2k_B T}, \qquad \text{(A-4)}$$

For instance, given $\Delta Eg = 0.2$ eV, the reduction factor turns out to be about 4 at 300 K, which can be a worthy tradeoff to the base resistance R_B, raising the margin of base thickness, lessening R_B, and still maintaining the base transit time in a reasonable range.

Demonstration of Graded-GaAsP Base HBTs

Epitaxial layer structure for the first fabrication of graded-GaAsP HBT [15] is shown in Table A-1. Thickness of compositionally graded-$GaAs_{1-X}P_X$ ($X = 0 \Rightarrow 0.05$) base layer (W_B) was 120 nm with carbon-doped to $p = 2\times10^{19}$ cm^{-3}. Graded-bandgap in the base (ΔEg) was 0.06 eV, which gives a built-in field ($\Delta Eg/W_B$) is 5 kV/cm for the electrons.

Table A-1 Epitaxial layer structure for the graded-GaAsP HBT [15].

Layer	Material	Thickness (nm)	Doping (cm^{-3})
Cap	n^+-GaAs	100	$>5\times10^{18}$
	n^+-InGaP	50	3×10^{18}
Emitter	N-InGaP	200	5×10^{17}
Base	p^+-$GaAs_{1-X}P_X$ ($X=0\rightarrow0.05$)	120	2×10^{19}
Collector	n^--GaAs	500	$<1\times10^{16}$
Subcollector	n^+-GaAs	500	1×10^{18}
Substrate	S.I. GaAs		

Figure A-1 shows the SIMS profiles of P^-, As^- and C^- in the vicinity of the base layer. It can be seen that a carbon-doped graded-GaAsP base structure has come into existence. For characteristic comparison, conventional uniform-GaAs base HBT epi-wafers were grown and equipped with the same emitter and collector structure and the same hole concentration of the base.

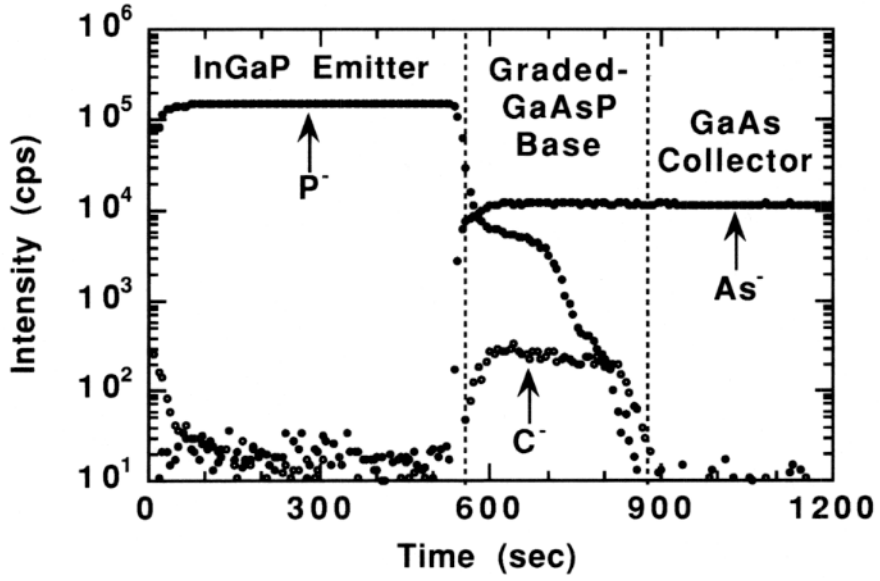

Fig. A-1. SIMS profiles of P, As and C in the vicinity of the base layer.

Figure A-2 shows the common emitter I-V characteristics of the graded-GaAsP base HBT with 110×110 μm^2 emitter area. A measured current gain was about 70 at a collector current density of 700 A/cm^2.

Figure A-3 shows the maximum current gain of the 12×12 μm^2 emitter area HBT devices as a function of the electric field in the base with a parameter of a minority electron diffusion length (L_e), assuming that recombination process in the base is dominant (see expression (A-1)). The graded-GaAsP HBT doubles the uniform-GaAs base HBT in current gain. Measured L_e of the graded-GaAsP base HBT and the uniform-GaAs base HBT agreed with their estimated one, which indicates that both HBTs have identical number of recombination centers.

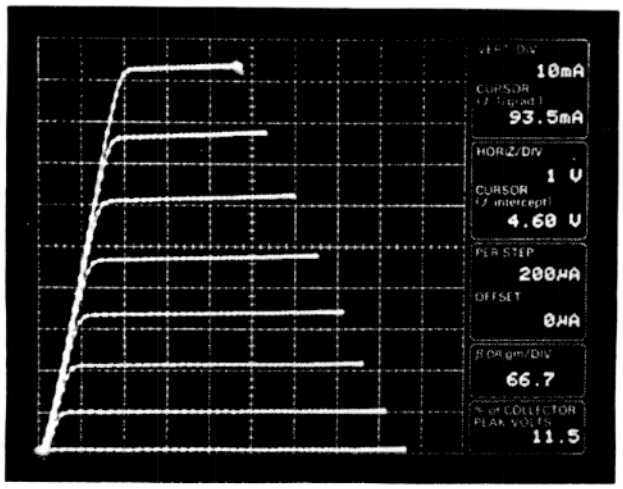

Fig. A-2. Common emitter I-V characteristics of the graded-GaAsP base HBT with 110 $\times$110 μm^2 emitter area.

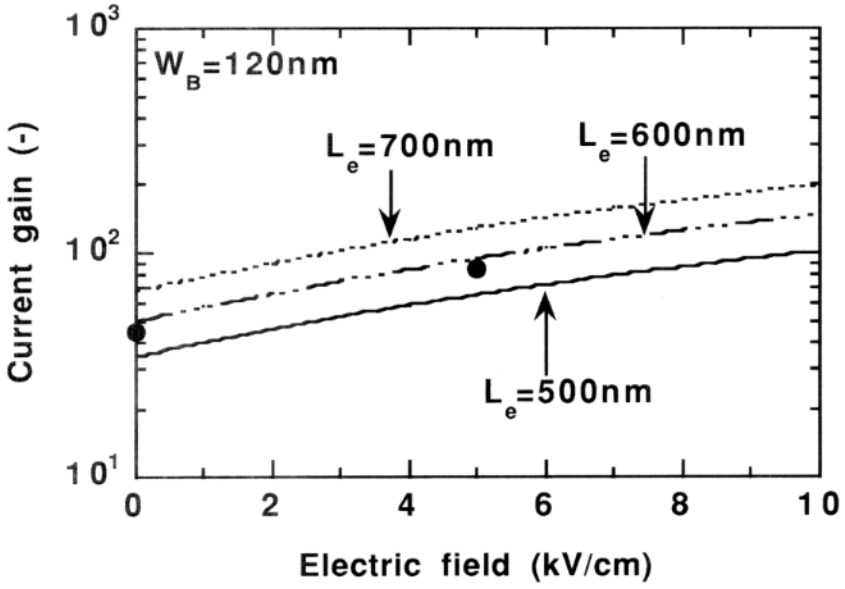

Fig. A-3. Maximum current gain of the 12$\times$12 μm^2 emitter area HBT devices as a function of the electric field in the base with a parameter of a minority electron diffusion length (L_e).

A *S* parameter was also measured to evaluate a cutoff frequency (f_T)— one of the high-frequency characteristics of HBTs. Devices, with a 4×20 μm^2 emitter area, measured 5 to 20 GHz of cutoff frequency at 4 V of V_{CE}. A maximum value of 20 GHz was measured, over against 17 GHz of the GaAs uniform-base HBT: the device was made faster performance, by shortening the delay time due to the electric field of the base layer. Figure A-4 shows the total delay time of the HBTs ($1/(2\pi f_T)$) as a function of an inverse collector current. The delay time is shorter for the graded- GaAsP base HBT for the uniform-GaAs base device. Since the collector and emitter layers have the same structure, this difference corresponds to the difference in the base delay time, which was found to be some 1 ps.

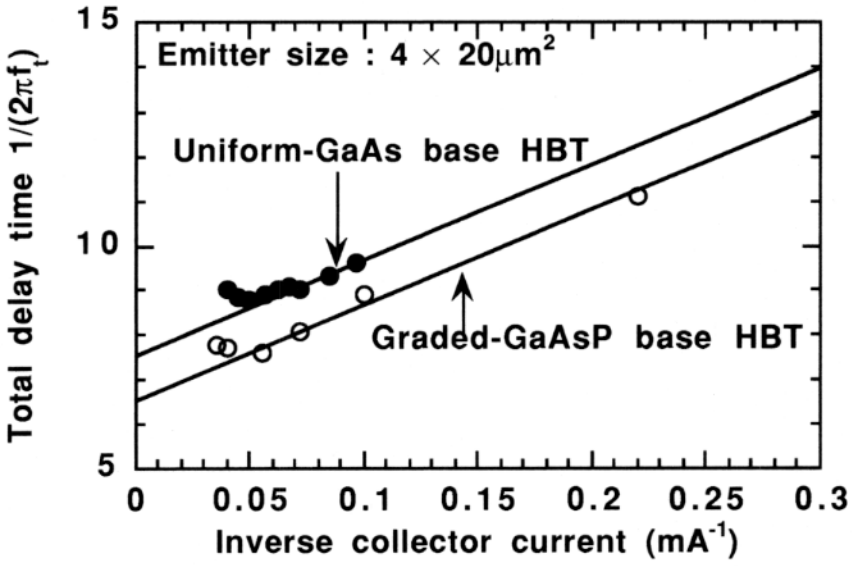

Fig. A-4. Total delay time of HBTs ($1/(2\pi f_T)$) as a function of an inverse collector current.

References

[1] W. A. Harrison, "Elementary theory of heterojunction," *J. Vac. Sci & Technol.*, vol. 14, pp. 1016-1025, 1977.

[2] R. L. Anderson, *Solid-State Electron.*, vol. 5, pp. 341, 1962.

[3] M. A. Rao, E. J. Caine H. Kroemer, S. I. Long and D. I. Babic, "Determination of Valence and conduction-band discontinuity at the (Ga, In)P/GaAs heterojunction by C-V profiling," *J. Appl. Phys.*, vol. 61, pp. 643-649, 1987.

[4] M. O. Watanabe and Y. Ohba, "Interface properties for GaAs/InGaAlP heterojunctions by the capacitance-voltage profiling technique," *Appl. Phys. Lett.*, vol. 50, pp. 906-980, 1987.

[5] D. Biswas N. Debbas, P. Bhattacharya. M. Razeghi, M. Defour and F. Omnes, "Conduction- and valence band offsets in GaAs/ $Ga_{0.51}In_{0.49}P$ single quantum well grown by metaloganic chemical vapor deposition, *Appl. Phys. Lett.*, vol. 56, pp. 833-835, 1990.

[6] M. A. Hasse, M. J. Hafich and G. Y. Robinson, "Internal photoemission and energy-band offsets in GaAs-GaInP *P-I-N* heterojunction photodiodes," *Appl. Phys. Lett.*, vol. 58, pp. 616-618, 1991.

[7] T. Kobayashi, K. Taira, F. Nakamura and H. Kawai, "Band lineup for GaInP/GaAs heterojunction by a high-gain Npn heterojunction bipolar transistors grown by metalorganic chemical vapor deposition," *J. Appl. Phys.*, vol. 65, pp. 4898-4902, 1989.

[8] J. Chen, J. R. Sites, I. L. Spain, M. J. Hafich and G. Y. Robinson, " Band offset of GaAs/$In_{0.48}Ga_{0.52}P$ measured under hydrostatic pressure," *Appl. Phys. Lett.*, vol. 58, pp. 744-746, 1991.

[9] S. Froyen, A. Zunger and A. Masacarenhas, "Polarization fields and band offsets in GaInP/GaAs and ordered/disorder GaInP supperlattices," *Appl. Phys. Lett.*, vol. 66, pp. 2852-2854, 1996.

[10] K. Kazmierski, P. Philippe, P. Poulain and B. deCremoux, "C-V measurement and modelization of GaInAs/InP heterointerface with traps," *J. Appl. Phys.*, vol. 61, pp. 1941-1946, 1987.

[11] S. Tanaka, M. Ito, M. Ikeda and T. Kikuta, "AlGaAs/GaAs heterojunction bipolar transistors with C-doped base grown by AP-MOVPE," *J. Cryst. Growth*, vol. 124, pp. 812-816, 1992.

[12] K. Saito, E. Tokumitsu, M. Konagai and K. Takahashi, "Theoretical analysis of AlGaAs/GaAs HBT including doping effects," 37th Spring Meeting of Japan Society of Applied Physics, 1a-T-4, March 1990.

[13] T. Ijichi, M. Ohkubo, N. Matsumoto and H. Okamoto, "High power CW operation of aluminum-free InGaAs/GaAs/InGaP strained layer single quantum well ridge waveguide lasers," *12th IEEE Int. Semiconductor Laser Conf.*, Davos, Switzerland, 1990, D-2, pp. 44-45.

[14] E. F. Shubert, L. W. Tu, G. J. Zydzik, R. F. Kopf, A. Benvenuti and M. R. Pinto, "Elimination of heterojunction band discontinuities by modulation doping," *Appl. Phys. Lett.*, vol. 60, pp. 466-468, 1992.

[15] K. Kojima, R. A. Morgan, T, Mullaly, G. D. Guth, M. W. Focht, R. E. Leibenguth and M. T. Asom, "Reduction of p-doped mirror electrical resistance of GaAs/AlAs vertical-cavity surface-emitting lasers by delta doping," *Electron. Lett.*, vol. 29, pp. 1771-1772, 1993.

[16] T. Miyamoto, K. Mori, H. Maekawa, Y. Inaba, F. Koyama and K. Iga, " Carrier transport p-type GaInAsP/InP distributed Bragg reflector," *Jpn. J. Appl. Phys. Lett.*, vol. 33, pp. 4614-4616, 1994.

[17] E. Zeeb and K. J. Ebeling, "Potential barriers and current-voltage characteristics of p-doped AlAs-GaAs heterojunctions," *J. Appl. Phys.*, vol. 72, pp. 993-999, 1992.

[19] S. Adachi, "Physical Properties of III-V Semiconductor Compounds," JOHN WILEY & SONS, 1992.

[20] M. P. C. M. Krijn, "Heterojunction band offsets and effective masses in III-V Quaternary Alloys," *Semicon. Sci. Technol.*, vol. 6, pp. 27, 1992.

[21] H. Ito, T. Ishibashi and T. Sugeta, "Current gain enhancement in graded base AlGaAs/GaAs heterojunction bipolar transistors," *Jpn. J. Appl. Phys.*, vol. 24, pp. L241, 1985.

[22] M. Ohkubo, S. Tanaka, M. Irikawa and T. Kikuta, "Heavily Zn-doped graded-base AlGaAs/GaAs HBT's," *IEEE Trans. Electron Devices*, vol. 38, No. 6, pp. 1557-1560, 1991.

[23] M. Ohkubo, N. Ikeda and T. Ninomiya, "Graded $GaAs_{1-X}P_X$ bases in heterojunction bipolar transistors with InGaP emitters," *Microwave and Optical Technology Letters*, vol. 11, no. 3, pp.150-153, 1996.

[24] W. T. Tsang, "A graded-index waveguide separate-confinement laser with very low threshold and a narrow Gaussian beam," *Appl. Phys. Lett.*, vol. 39, pp. 134-137, 1981.

[25] A. Kasukawa, Y. Imajo and T. Makino, "1.3 mm GaInAsP/InP buried heterostructure graded index separate confinement multiple quantum well (BH-GRIN-SC-MQW) lasers entirely grown by metalorganic chemical vapor deposition (MOCVD)," *Electron. Lett.*, vol. 25, pp. 104-105, 1989.

[26] S. R. Chinn, P. S. Zory and A. R. Reisinger, "A model for GRIN-SCH-SQW diodes lasers," *IEEE J. Quantum Electron.*, vol. 24, no. 11, pp. 2191-2214, January, 1992.

[27] H. Hirayama, Y. Miyake and M. Asada, "Analysis of injection efficiency of separate-confinement-heterostructure quantum-film lasers," *IEEE J. Quantum Electron.*, vol. 28, no. 6, pp. 68-74, January, 1992.

Chapter 3

Fabrication and Characterization of Graded-InGaAsP Structures

This chapter deals with a metal organic chemical vapor deposition technique, dedicated to the present study. InGaAsP layers lattice-matched to GaAs are described about the condition of their growth, along with the crystalline quality. In addition, 'graded-structure' is described regarding fabrication and characterized last.

3.1 Metal Organic Chemical Vapor Deposition Growth of Graded-InGaAsP Structures

3.1.1 MOCVD apparatus

A low-pressure Metal Organic Chemical Vapor Deposition (MOCVD) apparatus was used to accomplish this study, as shown in Fig. 3-1. Our MOCVD apparatus [1] is equipped with a vertical reactor, and a carbon succeptor coated SiC that is heated by an RF coil. The reactor, with a preparation chamber, can never be exposed to the ambient air, in the process of loading a wafer. The MOCVD is capable of growing a single two-inch wafer.

This MOCVD apparatus is carefully designed to minimize the dead volume in the stainless steel pipework and valves, while employing quick run-vent switching systems for sharp interfaces of epitaxial layers. Moreover, two or three source materials are provided in the process of growing InGaAsP layers. Each source material is under control, using its own mass flow controller (MFC): those materials need to be controlled at unique rates. In view of reproducibility, computer-control articulates the process primaries: growing pressure (Automatic Power Control), growth temperature (Automatic Temperature Control), gas flow rate and gas switching.

Epitaxial growth is carried out at 500 ℃ to 750 ℃ under a reduced pressure of 80 Torr. The Group III source materials are trimethylindium (TMIn), triethylgallium (TEGa) and trimethylgallium (TMGa); the Group V source materials are phosphine (PH_3) and arsine (AsH_3). The n-type dopant are hydrogen selenide (H_2Se) and silane (SiH_4); the p-type dopant is diethylzinc (DEZn).

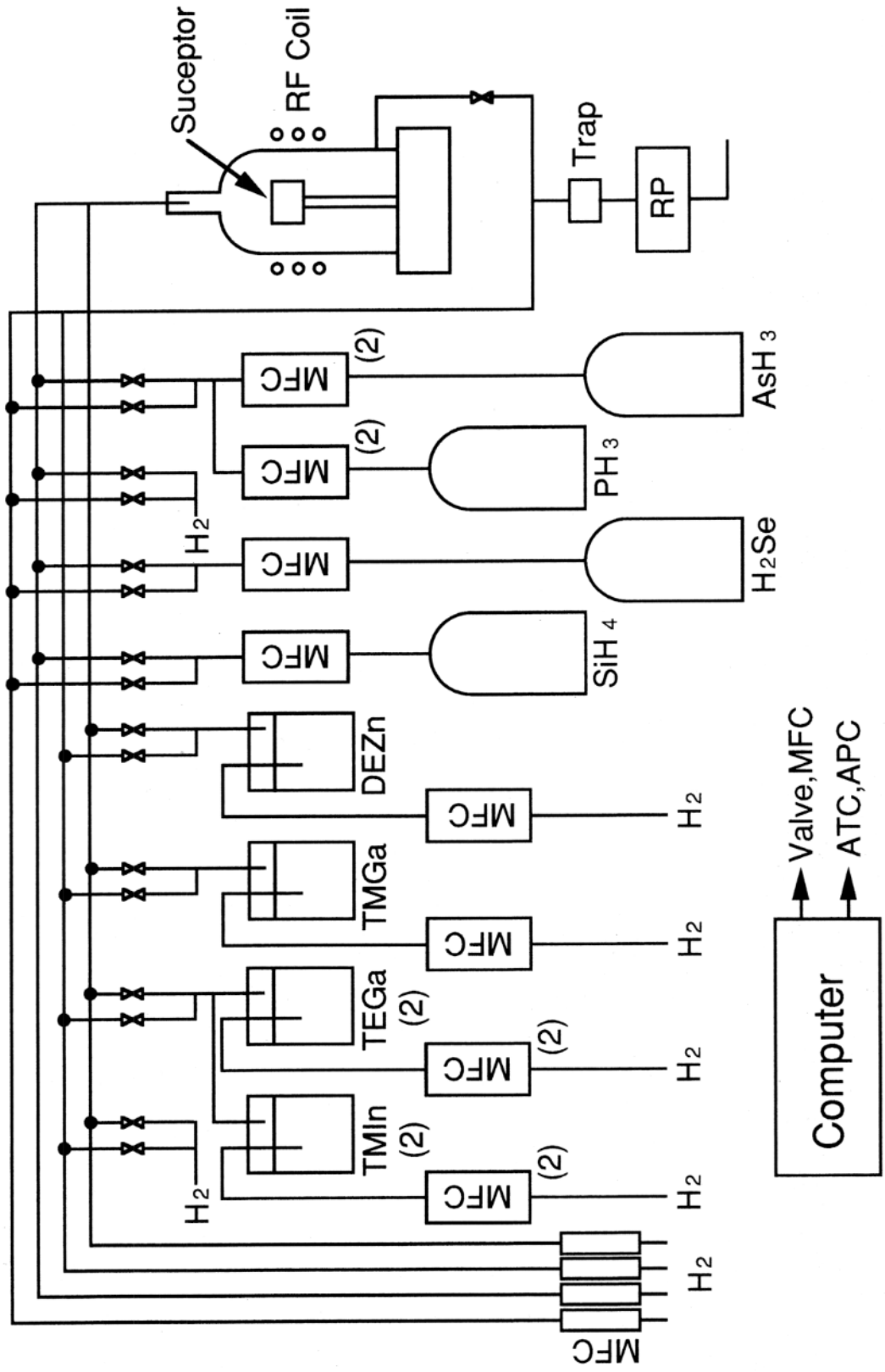

Fig. 3-1. Growth control of the MOCVD apparatus used in this study. Parenthesized figures: numbers of sources and MFCs.

3.1.2 Growth of InGaP Layers Lattice-matched to GaAs

In an attempt to grow InGaAsP layers on GaAs, we set about investigating the dependence of growth temperature on the growth of InGaP. The Ga composition X of $In_{1-X}Ga_XP$ can be correlated with the growth rate of InP (Rg_{InP}) and GaP (Rg_{GaP}), as follows:

$$X=\frac{Rg_{GaP}}{Rg_{InP}+Rg_{GaP}}. \qquad (3\text{-}1)$$

Figure 3-2 plots the relative growth rate of GaP as a function of growth temperature. The relative growth rate is standardized with a reference of GaP growth rate at 750 ℃. The growth rate of InP remains unchanged in a temperature range of 500 ℃ to 750 ℃ as in Fig. 3-2, as a proof that the MOCVD growth of InP with TMIn has been Mass-Transported-Limited effectually even at 500 ℃. But the growth of GaP with TEGa was kinetically limited below 600 ℃, because of a decrease in the TEGa decomposition. Of course, it is advisable to carry on the MOCVD growth at 600 ℃ constancy.

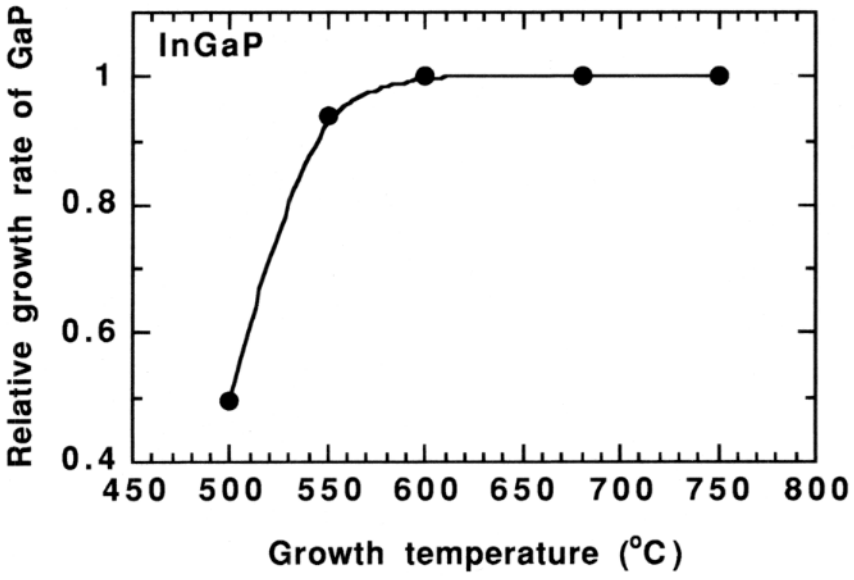

Fig. 3-2. Relative growth rate of GaP as a function of growth temperature.

Figure 3-3 plots Full Width at Half Maximum (FWHM) of photoluminescence (PL) spectra of InGaP at 77 K with reference to growth temperature. The FWHM of the PL spectra is rather broad at a kinetically limited temperature of 600 ℃ and draws a drastic curve of drop on the whole; the optimum value seems to be at 680 ℃ or thereabout.

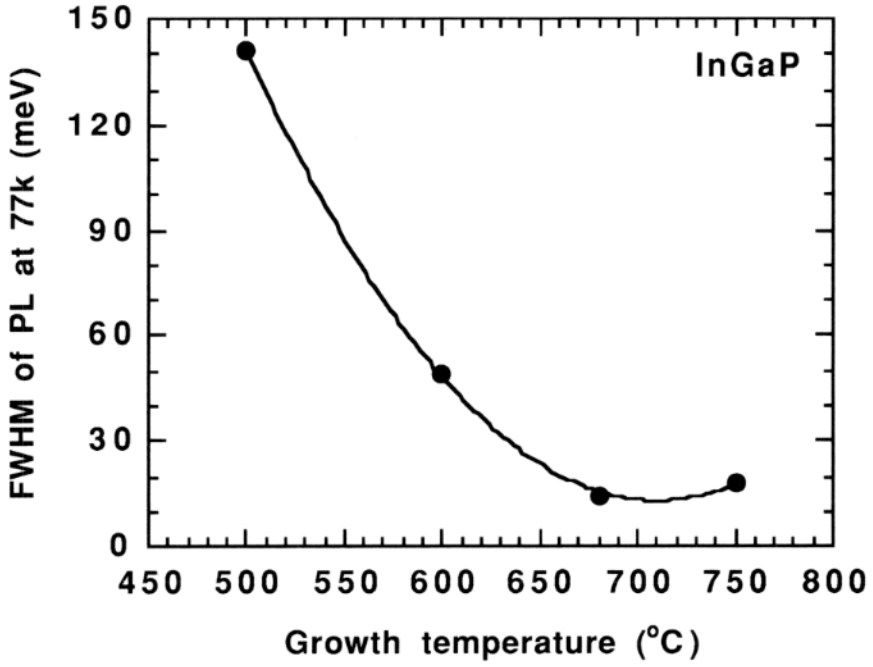

Fig. 3-3. FWHM of the PL spectra of InGaP at 77 K as a function of the growth temperature.

3.1.3 Growth of InGaAsP Layers Lattice-matched to GaAs

It is a more elaborate task to grow a material containing some Group V elements (e.g. InGaAsP), than containing a single Group V element. Now I explain findings from the growth conditions in Table 3-1, which were applied to grow InGaP layers with different bandgaps.

Figure 3-4 (a), (b) plots the experimental relationship between the molar flow rate and solid composition of $In_{1-X}Ga_XAs_YP_{1-Y}$ at 680 ℃, where Group III elements (Ga, In) and Group V elements (As, P) are dealt with. It can be learned that Ga/(In+Ga): X correlates proportionally with [TEGa]/([TMIn]+[TEGa]), and that log{As/(P+As)}: logY correlates proportionally with $[AsH_3]/([PH_3]+[AsH_3])$. The square brackets denote the molar flow rate of each source material. The relationship can be expressed for Group

III elements and Group V elements, as follows [2]:

$$\text{Group III} : X=\frac{[TEGa]}{[TMIn]+[TEGa]} \tag{3.2}$$

$$\text{Group V} : Y=\left\{\frac{[AsH_3]}{[PH_3]+[AsH_3]}\right\}^{0.3} \tag{3.3}$$

The logarithmic relation of Group V is most likely to support the solid-vapor composition diagrams from a model of chemical equilibrium calculated by Seki and Koukitsu [3-5] in Fig. 3-5. The exponentially-approximated relation of Group V seems to be interpreted by an incomplete PH_3 pyrolysis.

Table 3-1. MOCVD growth conditions for InGaAsP layers on GaAs.

Growth Temperature	**680～700 ℃**
Growth Pressure	**80 Torr**
Total Flow Rate	**8 slm**
Group III	**TMIn, TEGa**
Group V	**PH_3, AsH_3**
V/III Ratio	**180～340**
Dopant	**DEZn (p-type)** **H_2Se (n-type)** **SiH_4 (n-type)**

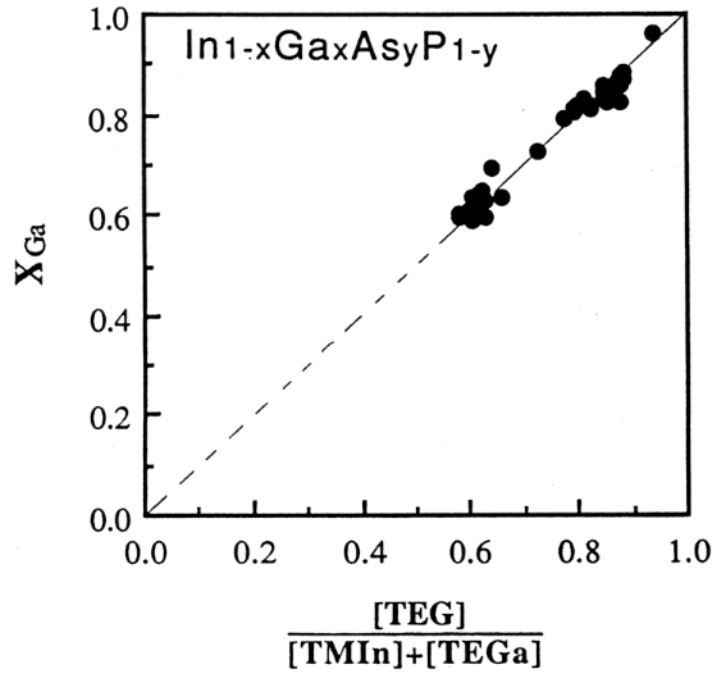

(a) Group III element.

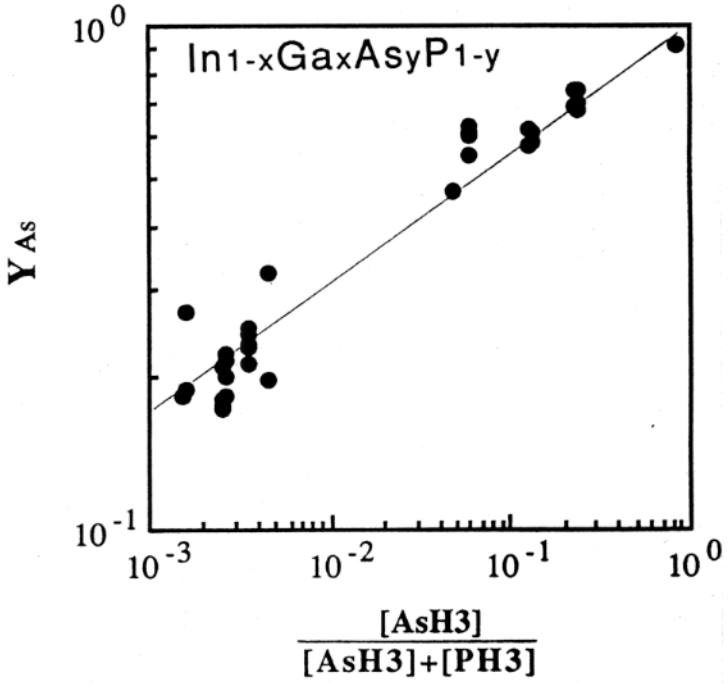

(b) Group V element.

Fig. 3-4. Experimental relationship between the molar flow rate and solid composition of $In_{1-X}Ga_XAs_YP_{1-Y}$.

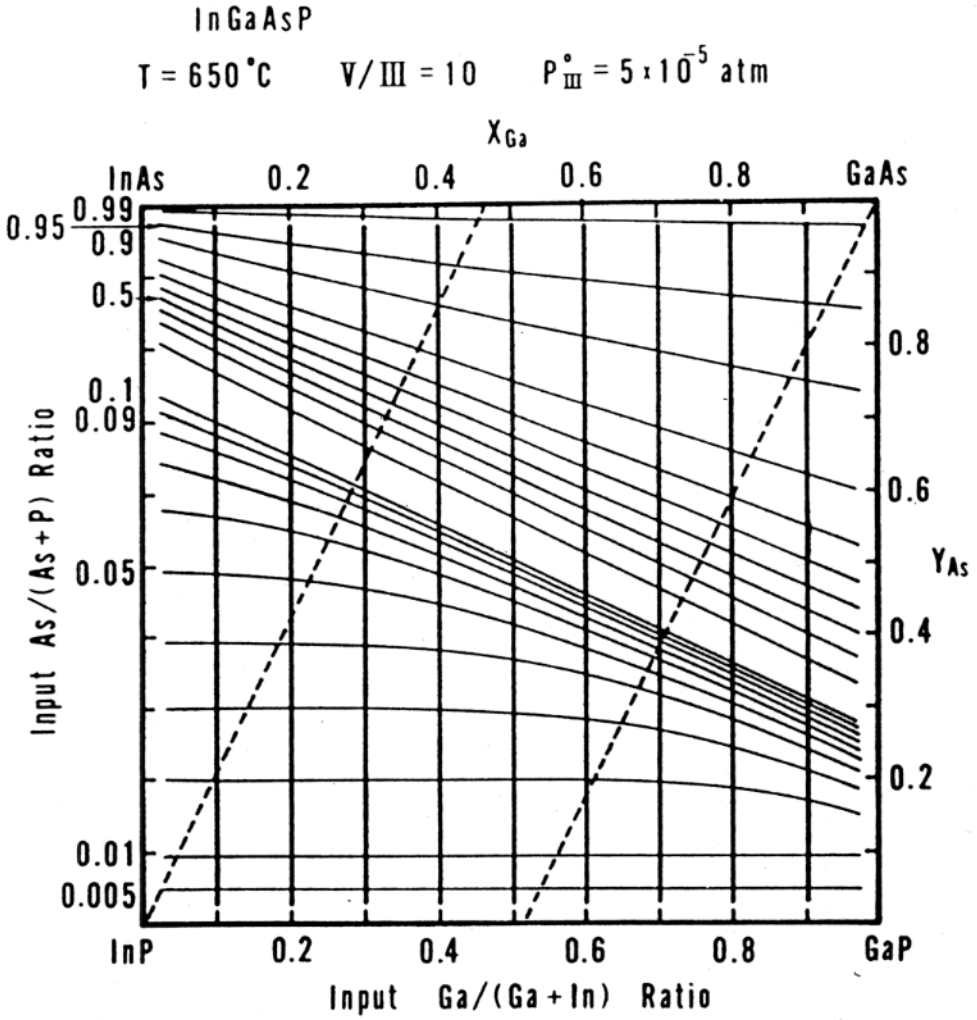

Fig. 3-5. Diagram of solid composition versus input ratio for $In_{1-X}Ga_XAs_YP_{1-Y}$ alloys. The dashed lines indicate the alloy compositions lattice-matched to InP and GaAs substrates [5].

3.1.4 Photoluminescence Study of InGaAsP Alloys on GaAs

Growth techniques (e.g., MOCVD or MBE method) have facilitated making an InGaAsP alloy on an InP substrate with ease. Quality of InGaAsP layers needs to be grown under thermodynamically stable conditions or in a miscible region. It was reported that a compositionally immiscible region existed in LPE grown layers under typical growth conditions, in the process of growing InGaAsP layers on GaAs [6]. Figure 3-6 shows spinodal curves for $In_{1-X}Ga_XAs_{1-Y}P_Y$ [7]. The straight lines denote the compositions of InGaAsP lattice-matching to InP and GaAs. The InGaAsP/GaAs system is more susceptible to immiscibility than the InGaAsP/InP. Consequently, the former needs to be under tighter control over the growth temperature.

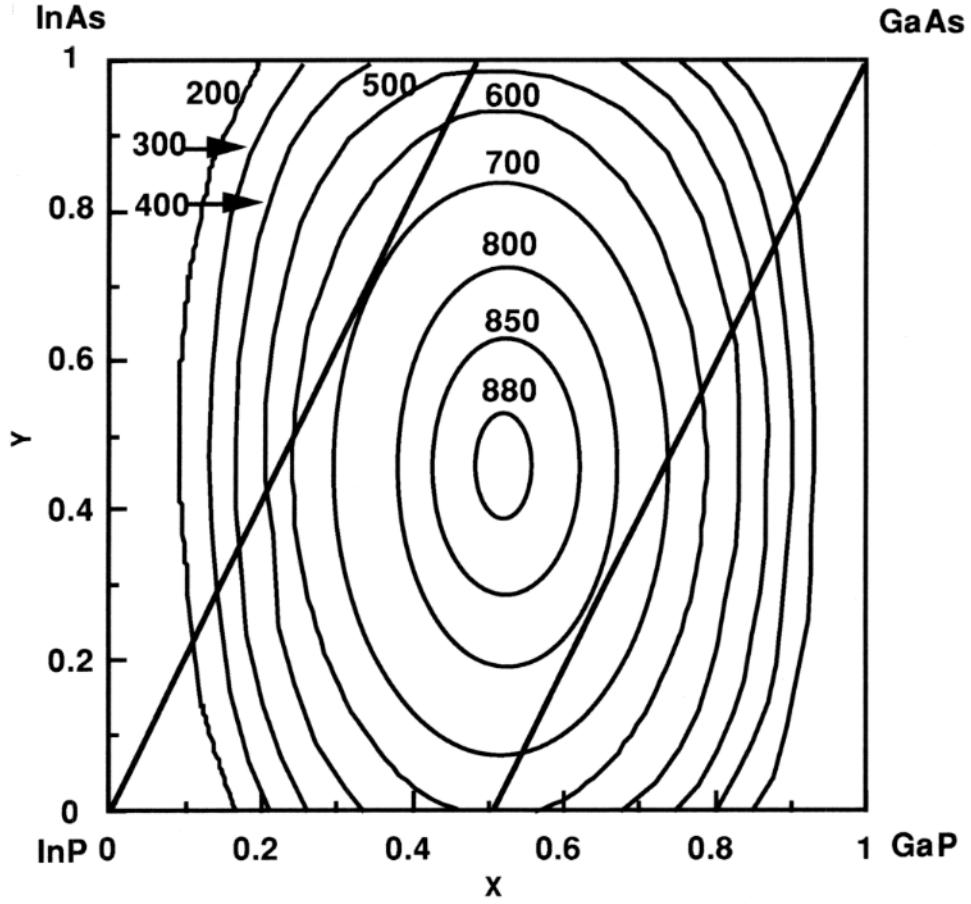

Fig. 3-6. Spinodal curves for $In_{1-X}Ga_X\ As_{1-Y}\ P_Y$ (solid line) [7]. The straight lines denote compositions for lattice matching to InP and GaAs, and number indicates the growth temperature.

Subsequently, it was planned to search out the immiscible phenomenon in MOCVD-grown InGaAsP layers at the optimum temperature of 680 ℃ for InGaP, where 500-nm-thick InGaAsP epitaxial layers on GaAs substrates were prepared; the epitaxial layers were typically at a rate of 5 nm/sec.

Figure 3-7 presents room-temperature PL spectra of InGaP, GaAs, and seven varied InGaAsP layers, excited with a 647 nm line of a Kr^+ laser. At 680 ℃, sharp PL-intensity and favorable surface morphology emerged in the both the regions of 660~710 nm and 760~870 nm, while some samples incurred faint PL-intensity in the middle region of InGaAsP (710~760 nm). These results point to the fact that a compositional immiscible region exists as theoretical thermodynamic calculations predicted [7]. Yet it seemed likely from the prediction [7], that the immiscible region would shrink at higher temperature. In effect, at an increased temperature of 700 ℃, strong PL intensity and a mirror-like surface morphology came into existence, even in the middle region, specifically (715 nm and 756 nm), as in Fig. 3-7.

Figure 3-8 shows the FWHM of PL spectra as a function of a Ga composition. In the middle region (0.65<[TEGa]/([TMIn]+[TEGa])<0.75), that is influenced by the immscible phenomenon seriously, the FWHM of the PL spectra of InGaAsP layers measured 60~70 meV at 700 ℃, and deserved to be utilized as graded-InGaAsP layers.

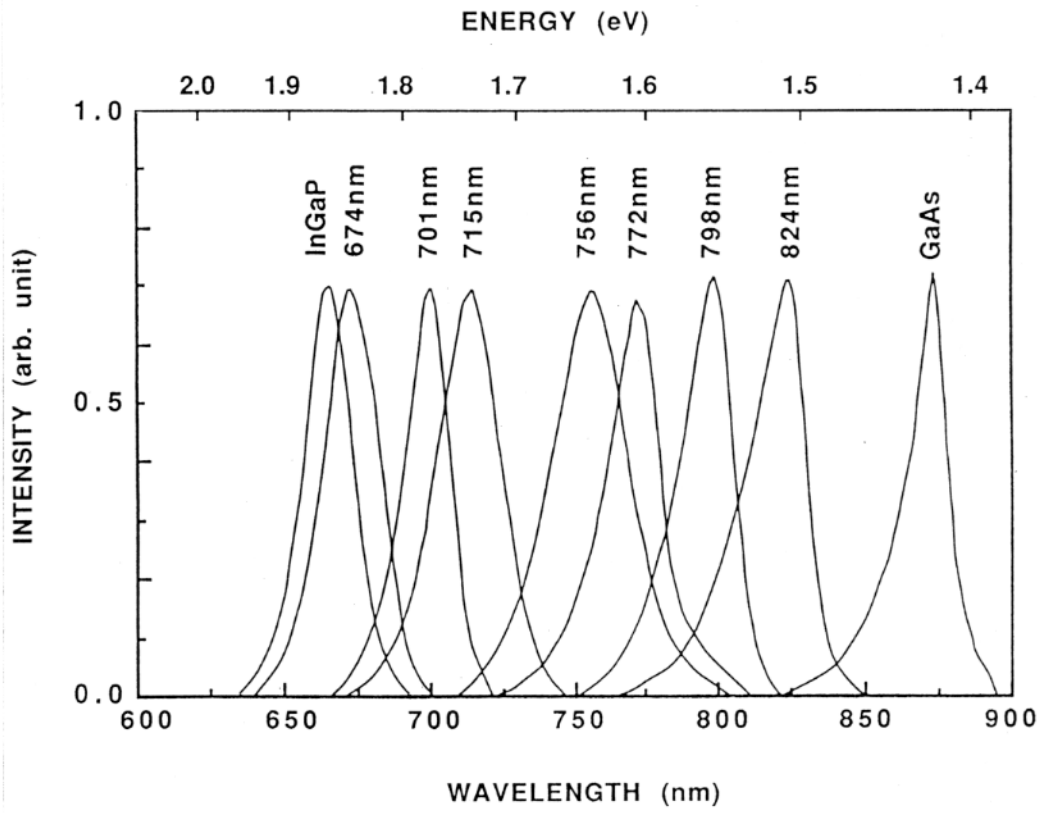

Fig. 3-7. Room temperature PL spectra of InGaP, GaAs and InGaAsP layers

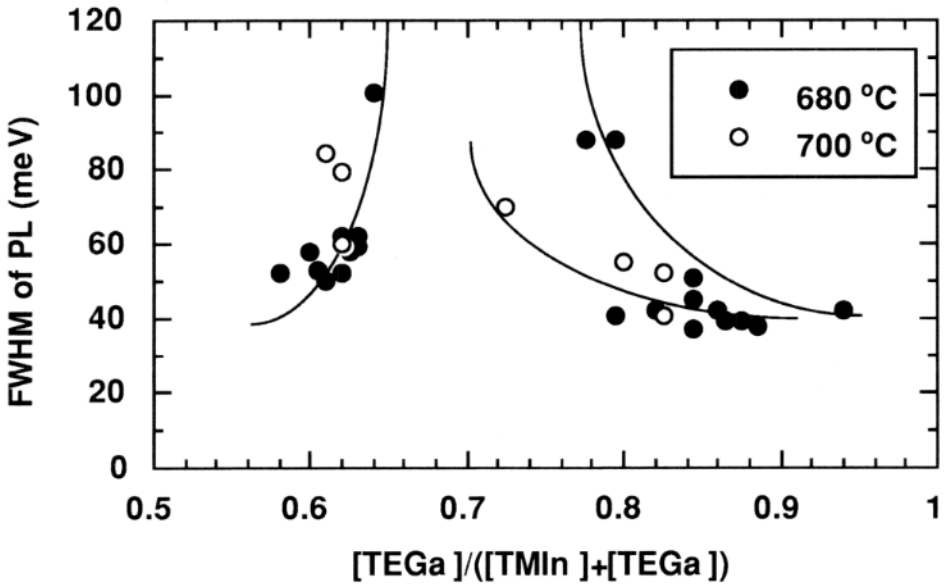

Fig. 3-8. FWHM of PL spectra as a function of a Ga composition.

3.1.5 Growth of InGaAsP/InP Single Quantum Wells

The heterointerface quality is a vital factor in growing a graded-InGaAsP structure. PL measurement of single quantum wells (SQWs) is regarded as being a powerful method to study heterointerface quality. MOCVD method requires optimization of the growth-interruption at the heterointerface to obtain sharp interfaces. Then, InGaAsP/InP SQWs were prepared to estimate interface quality and the effect of the growth-interruption.

Figure 3-9 shows a structure of SQWs on an InP substrate. These SQWs are, in thickness, 1.2, 2.5, 5.0 and 10.0 nm, and alternated with 500-nm-thick InP layers. Figure 3-10 shows a timing chart to alternate sources of Group III and Group V: TMIn, TEGa and AsH_3, PH_3. Growth interruption (t_p) was timed at 0, 20 and 240 sec for the respective heterointerfaces, without any Group III precursors, but as overpressured with Group V gases. Group V gases are switched in the middle of each growth interruption.

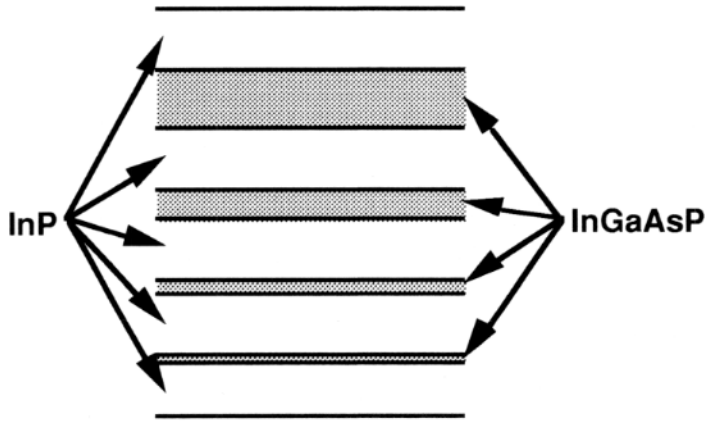

Fig. 3-9. Structure of SQWs on InP substrate.

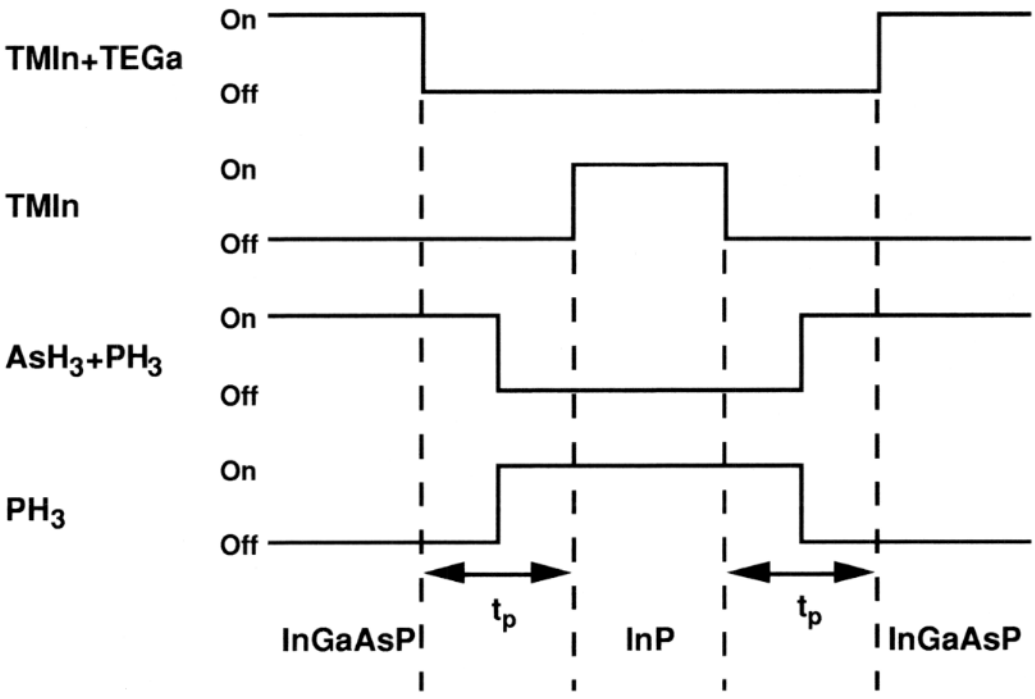

Fig. 3-10. Timing chart of alternate supply of the Group III (TMIn and TEGa) and Group V sources (AsH_3 and PH_3).

Figure 3-11 shows 4.2 K PL spectra of InGaAsP/InP SQWs, which resulted from (a) a growth interruption of 20 sec. and (b) no interruption. Inset (c) shows FWHM of the PL peak of the thinnest QWs as a function of growth-interruption time. A split peak of the thinnest QW layers arising from sample (a) attributes monolayer (ML) fluctuation in the well thickness. The true thickness of the thinnest QW measured 1.0 nm with a 10 % error, under TEM observation. That error stems from variation in thickness across the sample, with the result that the double-peak corresponds to 3 ML and 4 ML. Figure 3-11(c) presents FWHM values of PL peaks of the thinnest QWs of the samples, with which interruptions timed at 0, 20 and 240 sec. The 240 and 20-sec samples gave between 16 and 20 meV in FWHM of PL peaks of 3 and 4 ML, while the sample without any interruption gave between 21 and 28 meV. A single peak and increased FWHM values of the uninterrupted-growth sample indicate that the heterointerfaces do not have extended flat terraces. That is, the terrace falls short of the diameter of the exciton, where the PL peak does not split and FWHM broadens. It is considered that the difference between the samples with the growth-interruption time of 0 and 20 sec is due to the occurrence of surface diffusion. The 20-sec interrupted-growth sample had its interface flattened by surface diffusion, and had its average terrace stretched longer than the exciton diameter. The uninterrupted-growth sample incurred enough surface diffusion for making the interfaces flatted and the average terrace diameter less than that of the exciton. It was also determined that 2-sec interrupted growth sample was able to have a practical minimum split on the PL peak of the thinnest well.

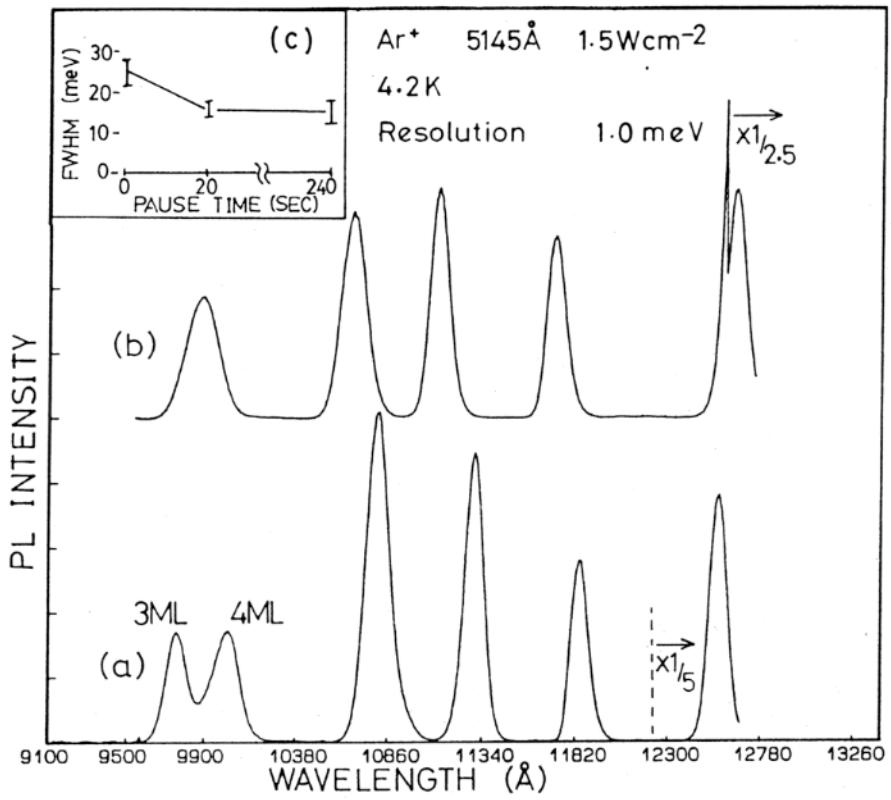

Fig. 3-11. 4.2 K PL spectra of InGaAsP/InP SQWs grown with (a) the growth-interruption time of 20 s and (b) no interruption. The inset (c) shows the FWHM of the PL peaks of the thinnest QWs as a function of growth-interruption time.

3.1.6 Growth of Graded-InGaAsP Structure

A multiple-step InGaAsP layer, requiring lattice matching and composition to be under simultaneous control, can hardly be grown repeatedly, unlike an AlGaAs/GaAs system. Worse, an InGaP/InGaAsP/GaAs system is far more seriously to suffer from immiscibility than any InP/InGaAsP/InGaAs system, as mentioned just before in last section. It is desirable to make epitaxial-growth temperature unchangeable in forming a graded structure, especially in working on a laser's active layer. Thus, the growth temperature of 680 ℃ was chosen to grow step-graded InGaAsP layers and maintained, so as to determine the readiness of adapting InGaAsP layers in an SCH region.

Figure 3-12 presents a Transmission Electron Microscope (TEM) observation of an InGaP/InGaAsP/GaAs epitaxial-layer structure. The InGaAsP layers consisted of three layers with bandgap wavelengths (or bandgaps) of λg (Eg) =700 nm (1.77 eV), 750 nm (1.65 eV) and 785 nm (1.58 eV), and had a unitary thickness of 20 nm. A lattice defect was located in the InGaAsP layer with =750 nm (1.65 eV) of λg (Eg), which was under the influence of the immiscible phenomenon at 680 ℃. The crystalline quality was improved by a halved growth rate of 2.5 nm/s instead of 5 nm/s and an increased V/III ratio of 340 instead of 180. Figure 3-13 presents a TEM observation of the above growth improvement on the InGaP/InGaAsP/GaAs structure. Neither a lattice defect nor a spot of immiscibility was located in the three InGaAsP layers, with the result that a layer thickness of 20 nm was less than of the critical thickness [8] where the domain growth started.

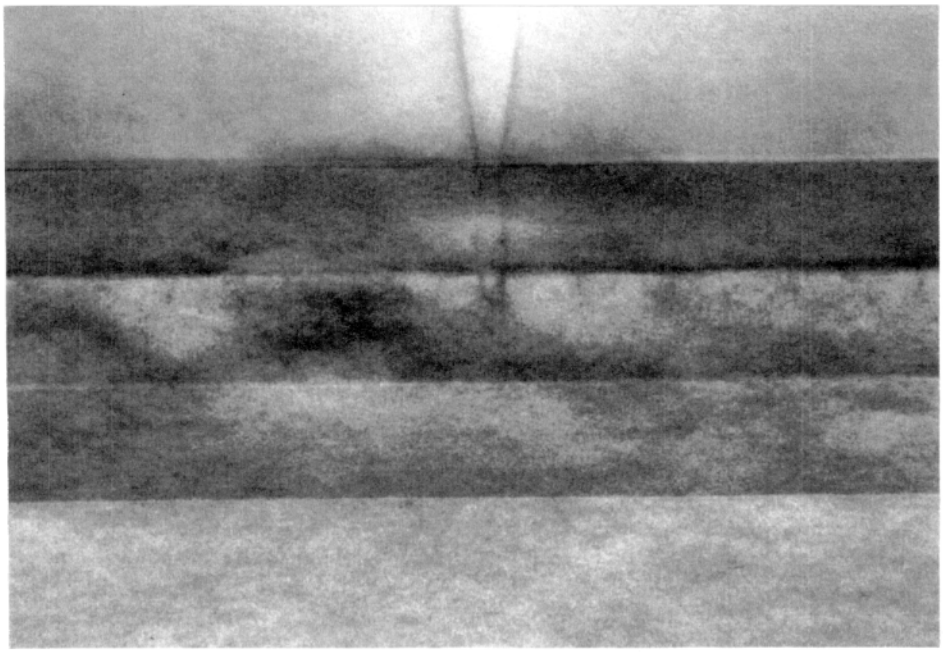

Fig. 3-12. TEM observation of InGaP/InGaAsP/GaAs structure with a lattice defect.

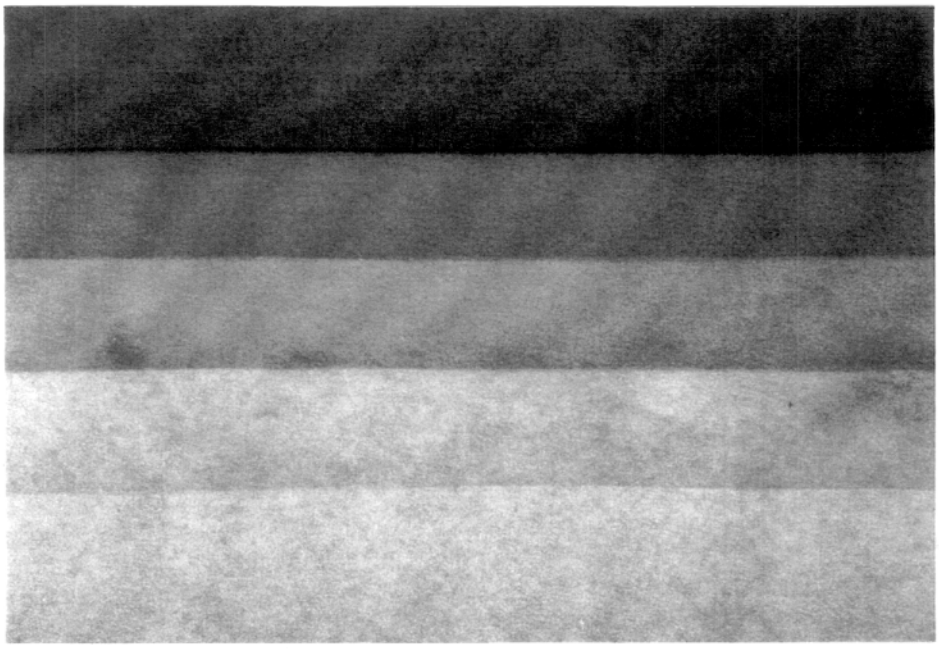

Fig. 3-13. TEM observation of improved growth of InGaP/InGaAsP/GaAs structure.

3.2 Fabrication and Characterization of Graded-InGaAsP Structures

Graded-bandgap structure technically serves as the key on the band-engineering concerned in every semiconductor device. This section characterizes graded-bandgap structures, by means of a current-voltage analysis of HBTs, and simultaneously offers a successful example of InP-based *Npn*-HBTs with graded-bandgap structures.

3.2.1 Characterization Scheme of Graded-Structures Using HBTs

The HBT has the makings of sorting out current components: with the approach of the transport yield in the base to unity, the collector current reflects the electron current (case of *NPN*) governed by the emitter/base heterojunction. This mechanics is sometimes utilized to characterize band discontinuity, as described in Section 2.2.

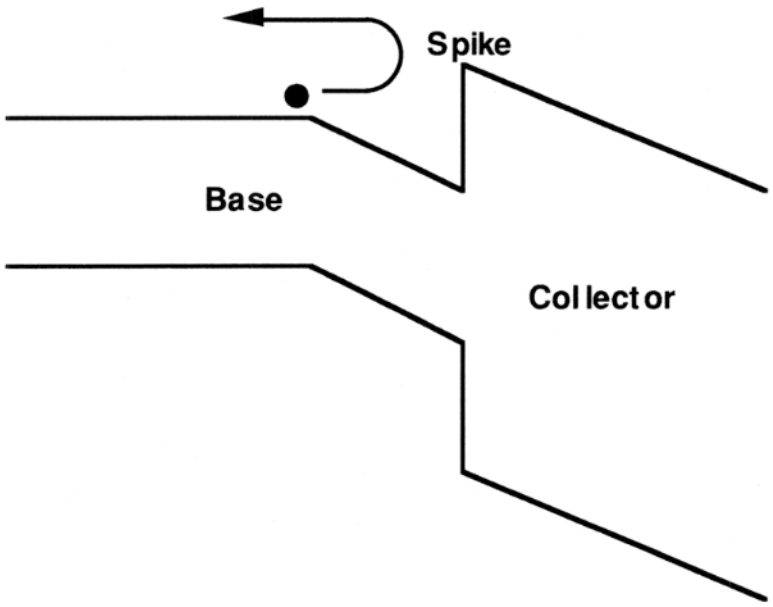

Fig. 3-14. Band diagram of base/collector heterojunction of D-HBTs; Formation of a conduction-band barrier (spike) blocks the electron injected toward the collector [9].

Now let's think over HBTs with other wide-bandgap materials in the collector, called as double-HBTs (D-HBTs). A conduction-band barrier (spike), arising out of the base/collector heterojunction, may block electron injected toward the collector [9], as shown in Fig. 3-14. Accordingly, the collector current of a D-HBT is governed by the structure of its base/collector heterojunction. The base/collector junction is structurally modified, where the modification can be characterized by measuring the change of a current-voltage relation of the D-HBTs. Section 2.3.1 characterizes the graded-structures

of two terminal devices with a p/p-heterojunction. Each of the two is biased to take control of current flow across the graded-structure, where current and voltage are dependent on each other. In the meantime, suppose that a D-HBT has its base/collector heterojunction attached with a graded-structure, the current flow can regulated, by adjusting discretely the emitter/base voltage and the voltage biased across the graded-structure. For instance, we can characterize the effect of a graded-structure, with a variable current density applied across there and a constant bias voltage. This sets access to detailed information about the graded-structure. The subsequent section deals with InP-based D-HBTs and highlights the effect of a graded-structure at a base/collector heterojunction.

3.2.2 InP-Based D-HBTs

InGaAs/InP HBTs are superior to AlGaAs/GaAs HBTs in lower-power dissipation and higher-frequency response. InP/InGaAs HBTs offer two choices of collector materials: InGaAs and InP. Single-HBTs (S-HBTs with an InGaAs collector) ideally match up to digital and low-power applications. InGaAs exhibits much higher low-field velocity than GaAs, InP or Si. The high velocity allows for very low collector doping and therefore very low collector capacitance. Since the peak velocity occurs at low field, the transit time is minimized at low collector voltages. By contrast, microwave and many analog applications operate at high power density (high voltage and high current). Narrow-bandgap InGaAs collectors have been somewhat leaky at high current densities, leading to a low collector-emitter breakdown voltage. Those leaky collectors can be reduced by replacing the narrow-bandgap InGaAs with wide-bandgap InP. The InP collector exhibits a high breakdown voltage and a high saturated velocity. Yet the base/collector heterojunction reduces current gain, because of the high and wide conduction-band spike at the hetero-interface — Electron Blocking Effect [9].

This study was preceded by solving the electron blocking, with inserting a thin n-InP layer (30 nm) [10] and a δ-doped n-InP layer (20 nm) [11] grown by MOCVD, and a single step InGaAsP layer (20 nm) grown by gas-source MBE [12] and chemical beam epitaxy [13] between base and collector. As described in Chapter 2, an ideal method of epitaxial growth ought to create smooth potential profile with compositional grading across the heterointerface. This section remarks on the effects of the graded InGaAsP layers inserted between the InGaAs base and InP collector of a D-HBT grown by MOCVD.

3.2.3 Concept of InP/InGaAs D-HBTs with Graded-InGaAsP Collector

Figure 3-15 shows schematic band structures (a) with and (b) without graded-InGaAsP layers. Graded layers inserted between InGaAs base and InP collector turn out to separate a large and wide spike at the base/collector interface into a number of lower and narrow spikes. As a result, tunneling may be suppressed through the spikes due to reduction of the electron blocking effect and improvement of collection efficiency of the electrons injected toward the collector is expected to be increased.

A key factor in designing a graded-collector is how to increase the number of InGaAsP layers, in an attempt to reduce conduction band spikes effectively, without increasing recombination current arising at InGaAsP/InGaAsP heterointerfaces. It may be advisable to set up three InGaAsP layers so as to make conduction band spikes on the decrease and recombination current on the increase.

A second key factor is to insert an n-InGaAs layer between the p^+-InGaAs base and first InGaAsP layer so as to relocate a first conduction spike to the base-collector space charge region. It is difficult to chose a rational thickness for this layer, where a thicker layer acts to reduce the electron blocking effect, concerning in lowering the breakdown voltage, on account of its high impact ionization coefficient. On analysis, I concluded that as thin as 10 nm in thickness could be applied with some reduction of spikes, but without sacrificing any appreciable drop in the breakdown voltage.

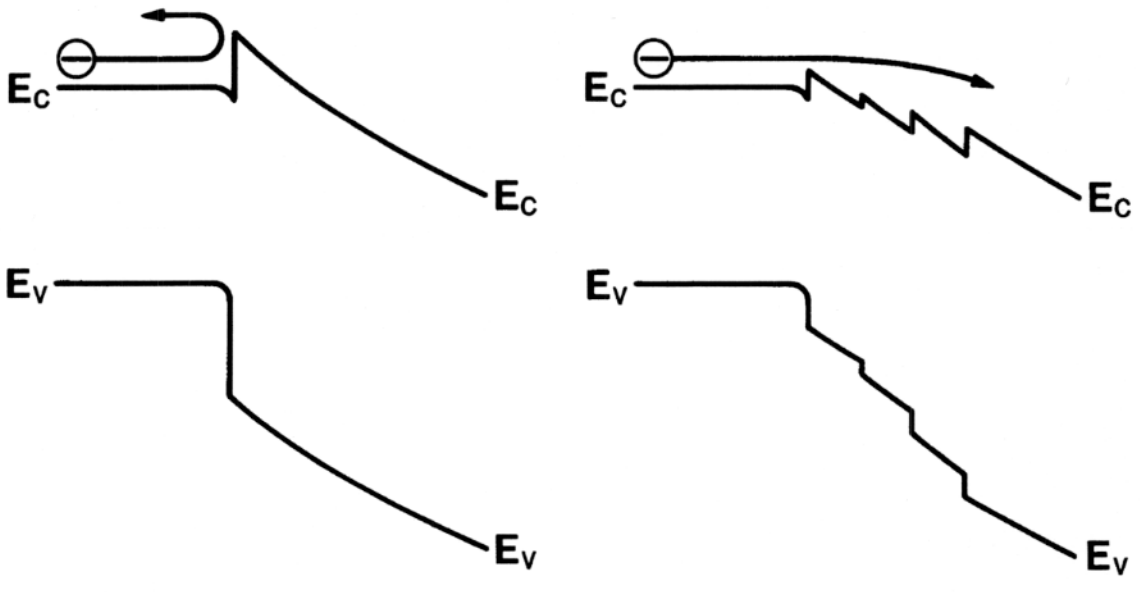

(a) With graded layers. (b) Without graded layers.

Fig. 3-15. Schematic band diagram of base/collector of D-HBTs.

3.2.4 Epitaxial Structure and Device Fabrication of D-HBTs

Two types of D-HBT epilayers, to demonstrate the foregoing theory, were prepared, each being lattice-matched to semi-insulating 2" (100) InP substrates grown by low-pressure MOCVD. One type had graded-InGaAsP layers between the InGaAs base and InP collector; the other did not have any graded-InGaAsP layers. Both were made to grow under a pressure of 80 torr and at a temperature of 665 ℃ in a vertical reactor.

Figure 3-16 shows a structure of D-HBTs epilayers with graded InGaAsP layers. The collector layer consists of an n^+-InGaAs contact layer, a 300-nm-thick n-InP layer and 60-nm-thick graded n-InGaAsP layers. Three-step InGaAsP layers were on trial applied to pride a grading effect, with a bandgap (Eg) of 1.24 eV, 1.04 eV and 0.95 eV. Each layer was adjusted a thickness of 20 nm. A 10-nm-thick, undoped InGaAs spacer-layer was inserted at the base/collector heterojunction. The base region was comprised of a 100-nm-thick InGaAs layer, doped with Zn by $p = 5\times10^{18}$ cm^{-3}; no spacer layer was prepared between the emitter and base. The emitter layer was comprised of a 300-nm-thick InP layer, doped with Si by $n = 5\times10^{17}$ cm^{-3}, and an n^+-InGaAs cap layer, doped with Se by $n = 1.5\times10^{19}$ cm^{-3}.

After epitaxial growth, mesa structure devices were fabricated by a wet chemical selective etching process and liftoff technique. Surface passivation was provided by depositing a 150-nm-thick SiN film. Those devices had heavily doped InGaAs layers of its emitter cap, base and sub-collector, processed into Ti/Pt/Au ohmic contacts.

Layer	Material	Thickness (nm)	Doping (cm^{-3})
Cap	InGaAs	100	Se : 1×10^{19}
Emitter	InP	300	Si : 5×10^{17}
Base	InGaAs	100	Zn : 5×10^{18}
Collector	InGaAs	10	
	Graded-InGaAsP	20×3	Si : 5×10^{16}
	InP	300	Si : 3×10^{16}
Sub Collector	InGaAs	500	Se : 1.5×10^{19}
Substrate	S.I. InP		

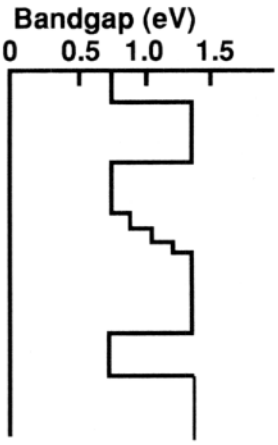

Fig. 3-16. Structure of D-HBTs epilayers with graded InGaAsP layers.

3.2.5 Characterization of Graded-InGaAsP Structures

The insertion of graded InGaAsP layers may allow more generation-recombination current to be induced by the InGaAsP interfaces. Consequently, the quality of these layers was determined as explained onward: First, the base/collector region was observed by a TEM image, which showed sharp interfaces — no transition layers in cross-sections as cleaved. Second, as Fig. 3-17 plots, current-voltage characteristics were measured for D-HBTs, which were attached with a few or no graded layers. An ideality factor turned out to be n_{BC}=1.04 in both devices as forward-biased. The value, being a approach to unity, suggests that quality of both interfaces is quite good enough for HBTs. Conversely, the devices as reverse-biased, incurred a similar leak current to the foregoing. This implies that the generation-recombination current is negligible in both HBTs.

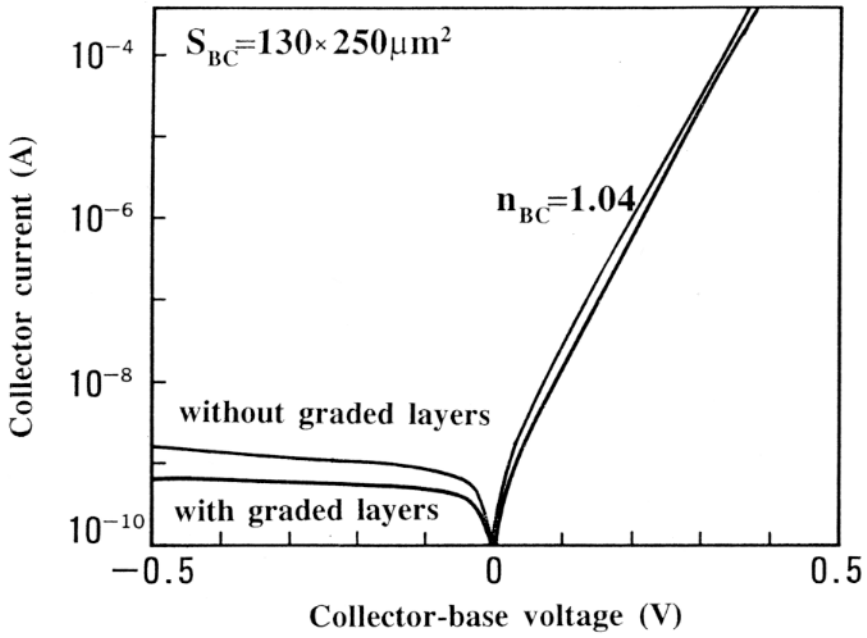

Fig. 3-17. Current/voltage characteristics of base/collector junction with and without graded layers.

Figure 3-18 shows Gummel plots of D-HBT with and without graded layers. For the sake of convenience, D-HBT with Graded Layers is called D-HBT/GL and D-HBT without Graded Layers is called D-HBT. At lower base/emitter voltage (V_{be}), the base current of D-HBT is higher than that of D-HBT/GL. This result indicates that electrons injected toward the collector are reflected by the conduction barrier, as shown in Fig. 3-15, increasing the recombination in the base layer. With increasing V_{be} for larger collector current density, the collector current of D-HBT decreases, more than the D-HBT/GL. This result indicates that the accumulation of electrons in the notch neighboring the spike of D-HBT does take place, and raise the conduction band spike (see Fig. 3-19), and thereby enhances the electron blocking effect [14].

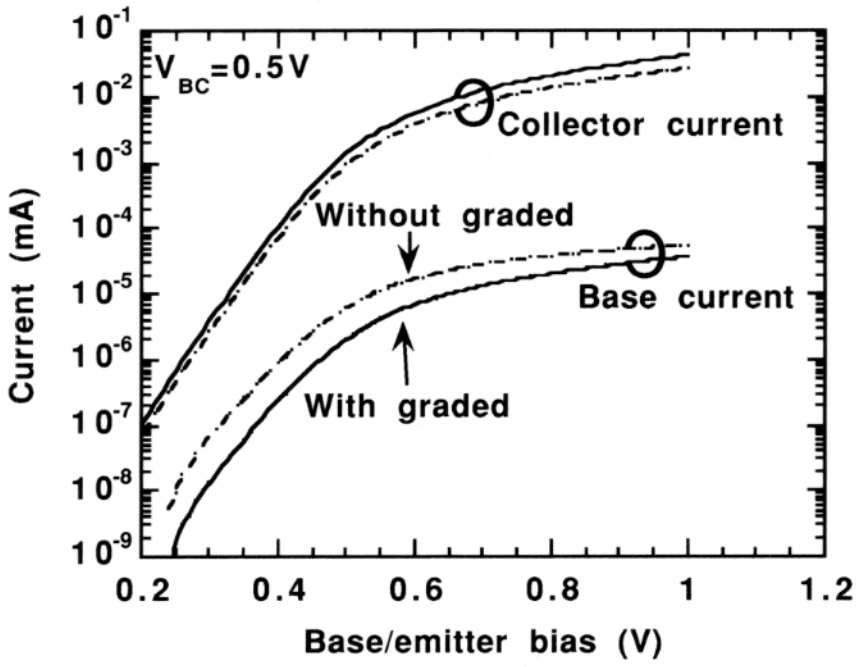

Fig. 3-18. Gummel plots of D-HBT with and without graded layers.

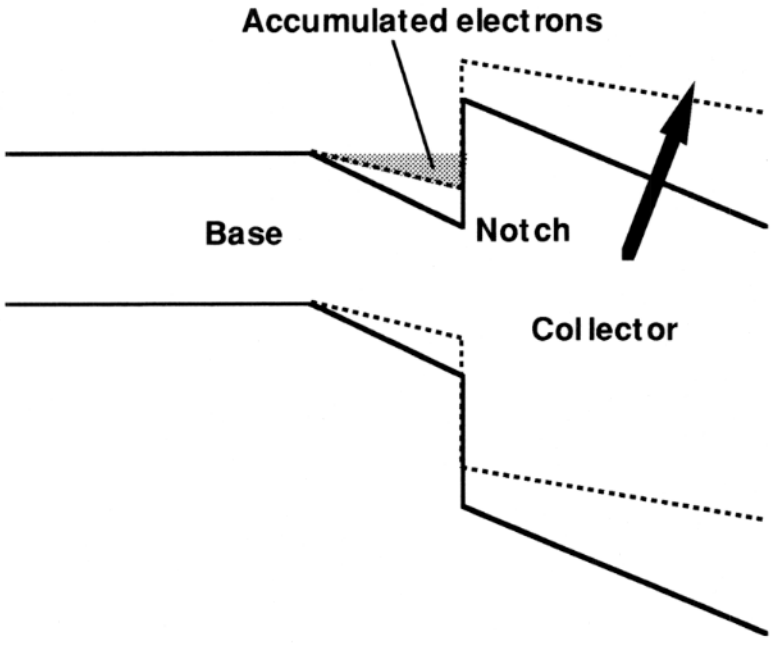

Fig. 3-19. Schematic band diagram of base/collector heterojunction of D-HBT without graded layers. At a high current density, electron accumulation in the notch takes place, and raise the conduction band spike [14].

Figure 3-20 shows the common emitter characteristics of (a) D-HBT/GL and (b) D-HBT. The collector current on the D-HBT is apparently more dependent on the collector/emitter voltage than that of D-HBTs/GL. D-HBT's exponential-like dependence of collector current offers a surmise that carriers tunneling through the spike plays an important role at the base/collector interface. That is, inserting graded layers is capable of suppressing the spike, where carriers have to pass across by the tunneling, and increasing the thermionic emission rate. The current gain of the D-HBT/GL, in turn, exceeds 1000 (I_B=60 μA), doubling what the D-HBT can produce. These results give proof that graded-InGaAsP structure can exhibit the estimated performance, with considerable accuracy.

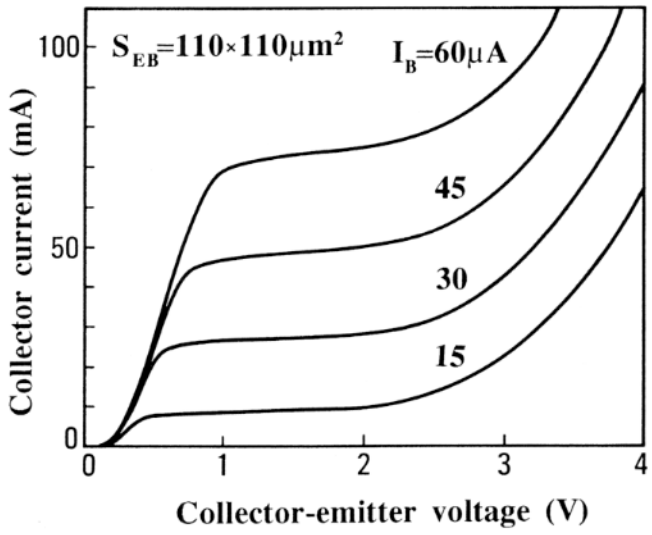

(a) With graded layers.

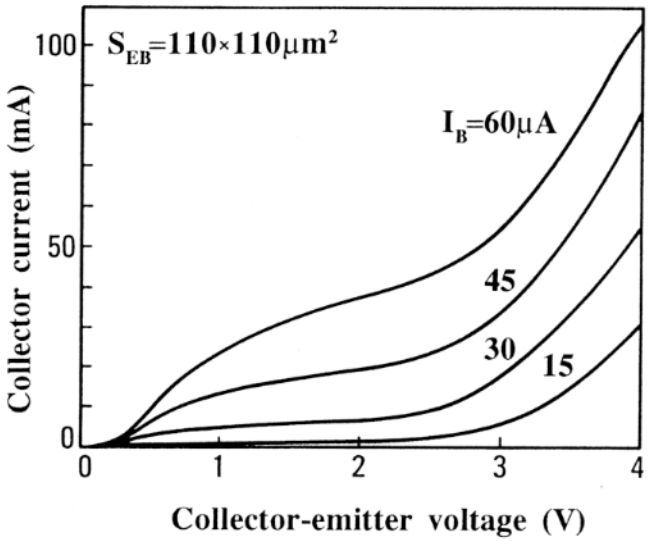

(b) Without graded layers.

Fig. 3-20. Common emitter characteristics of D-HBTs.

Recently, optimization of the graded-InGaAsP collector was reported using the two-dimensional device simulator, MEDICI [15] from Technology Modeling Associates. The simulated structures were similar to that shown in Fig. 3-16: they have 70-nm-thick InP emitter ($n = 7\times10^{17}$ cm^{-3}), and 45-nm-thick InGaAs base ($p = 2\times10^{19}$ cm^{-3}) and 260-nm-thick graded-InGaAsP collector. The collector layers comprise several 20-nm-thick InGaAsP and thick InP layers. Three schemes for grading were selected: (i) the increasing conduction band discontinuity (ΔE_c) scheme, (ii) the uniform ΔE_c scheme agreeing with the counterpart used in the last section, and (iii) the decreasing ΔE_c scheme. Two InGaAsP layers are used in the collector and their bandgap are summarized in Table 3-2.

Figure 3-21 presents simulation results of (a) Gummel plot and (b) conduction band diagram and electron concentration at V_{ce}=1.8 V for the D-HBTs with various band offset schemes. As Fig. 3-21(a) shows, the increasing ΔE_c scheme is least effective in curbing carrier blocking and has the lowest maximum collector current density. The ΔE_c at the last InGaAsP/InP heterointerface is seen in Fig. 3-21(b) to be the largest for the increasing ΔE_c scheme and the associated conduction band spike therefore traps the highest number of electrons. The last conduction band spike, being furthest into the collector, rises significantly and thereby seriously blocks the electron flow at high bias, as shown in Fig. 3-21(b) after trapping a substantial number of electrons. In other words, the increasing ΔE_c scheme traps a higher concentration of electrons than any other concentration of the other two, seems to thereby exhibit the least current gain (I_C/I_B). Likewise, the uniform ΔE_c scheme or increasing ΔE_c scheme can trap a less concentration of electrons, than the increasing ΔE_c. Even as highly biased there, the collector current is restrained from lowering and the base current is restrained from rising.

Table 3-2. Bandgap of various layers of step-graded collector [15].

		Band offset (ΔE_c) scheme		
		Increasing	Uniform	Decreasing
Bandgap E_g/eV	InGaAs		0.75	
	1st InGaAsP	0.82	0.95	1.10
	2nd InGaAsP	1.00	1.15	1.28
	InP		1.35	

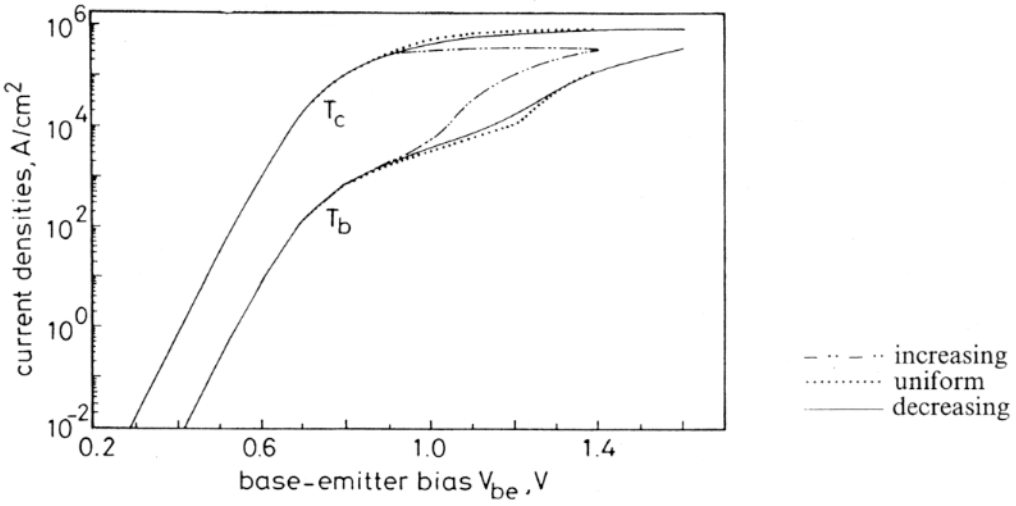

(a) Gummel plot.

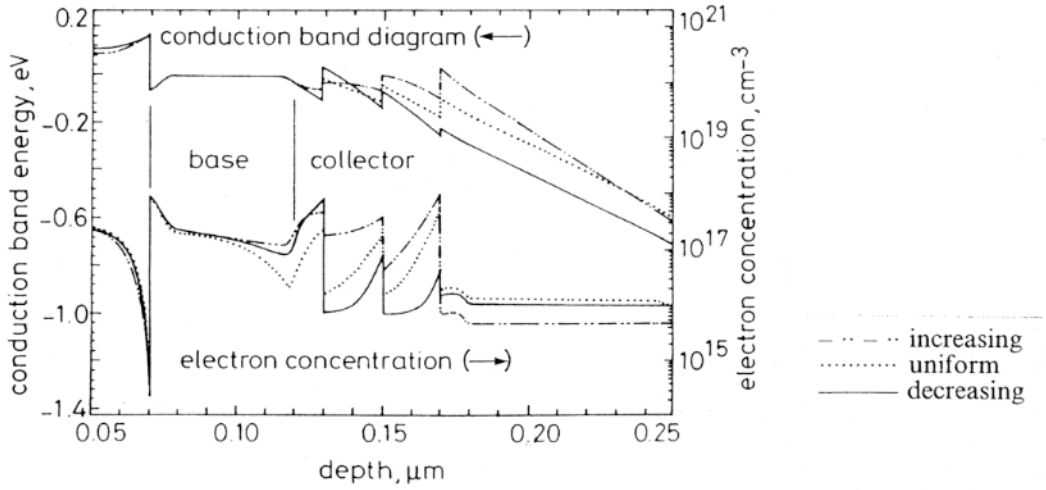

(b) Conduction band diagram and electron concentartion.

Fig. 3-21. Simulation results of (a) Gummel plot and (b) conduction band diagram and electron concentartion at V_{ce}=1.8 V for D-HBTs with various band offset schemes [15].

3.2.6 Ultimate Graded-Structure : Continuous Grading

In terms of a D-HBT's collector of a graded-structure, compositionally-step-graded InGaAsP layers may be incapable of eradicating carrier blocking, which can be linked up with trapping electrons due to the finite conduction spike. Worse, a trifle of trapped electrons may degrade the high-frequency response at a high collector density. It is a specious counteraction against the problem to increase the number of InGaAsP layers. By necessity, the counteraction results in an increased number of heterointerfaces, not to increase generation-recombination current.

If the lattice matching of InGaAsP were under control precisely like AlGaAs/GaAs system, a continuous graded-InGaAsP layer could come into existence to be an ultimate graded-structure. Figure 3-22 presents Secondary Ion Mass Spectroscoy (SIMS) profiles of a collector region in of a D-HBT. Preparatory to fabricating a continuous graded-InGaAsP structure, a number of lattice-matching conditions for InGaAsP layers with various bandgap are indispensable without fail. Figure 3-22 shows that the profiles of P+ and As+ change without cease.

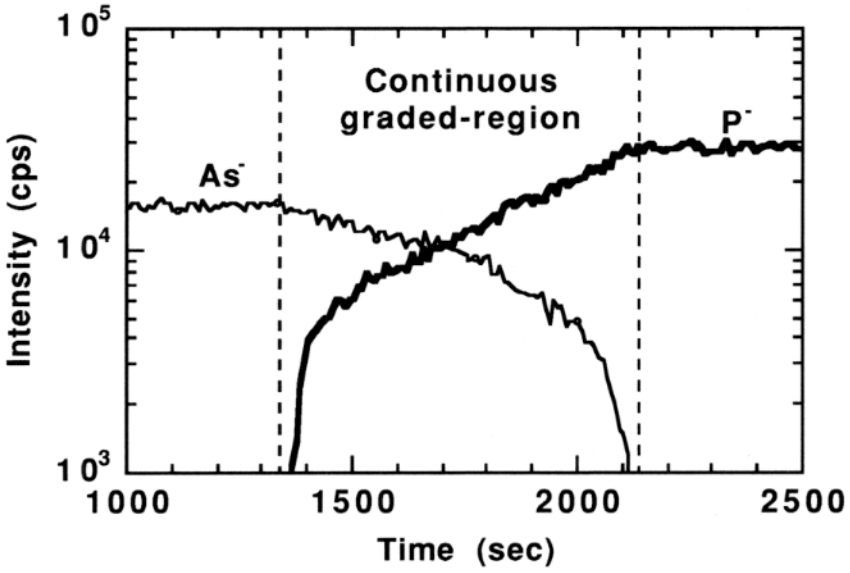

Fig. 3-22. SIMS profiles of continuous graded-InGaAsP region of D-HBTs.

Figure 3-23 shows current-voltage characteristics for the base/collector junction of D-HBT with continuous graded-InGaAsP structure. The reverse-biased leak current is comparable to that of D-HBTs with stepped graded-InGaAsP structure (see Fig. 3-17), which is encouraging characteristics to employ continuous graded-InGaAsP structure.

Fig. 3-24 shows a Gummel plot of a D-HBT with continuous graded-InGaAsP structure, as contrasted with a three-step-graded structure. The plots show no significant difference in the Gummel plot between the two D-HBTs. It reflects that continuous grading and stepped grading can give rise to no substantial difference between both current gains. These results indicate that three-step-graded structure enables to suppress a conduction-band-spike effect enough on static characteristics; and, increasing number of InGaAsP layers can take scarcely any effect in practice. Specifically, stepped-grading structure, easier to fabricate, may be preferable on the whole.

Continuous grading was applied to a laser and is demonstrated in Chapter 4, where continuously-graded GRIN-SCH structure is provided, while showing excellent superior characteristics or no sacrificed performance.

If lattice-matching were indifferent between epitaxial layers and a substrate, it would no doubt be easier to realize a continuous graded-structure, even with InGaAsP. Also, it is a matter of course to pay attention to a critical thickness which allows a dislocation to generate, considering accumulation of the strain energy due to lattice-mismatch. It was reported that a demonstration took place to prove that strained, graded-structure applied to the base layers of HBTs can bring out improvements [16,17, see appendix A]. Further modification may be carried out in combination with a strain-compensated structure so that we can no longer struggle with any lattice-matching.

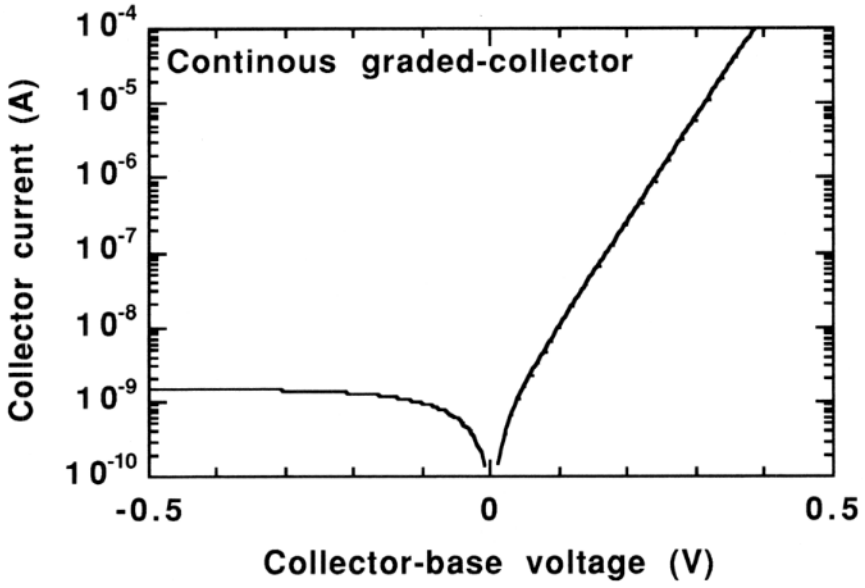

Fig. 3-23. Current/voltage characteristics of the base/collector junction of D-HBTs with continuous graded-InGaAsP structure.

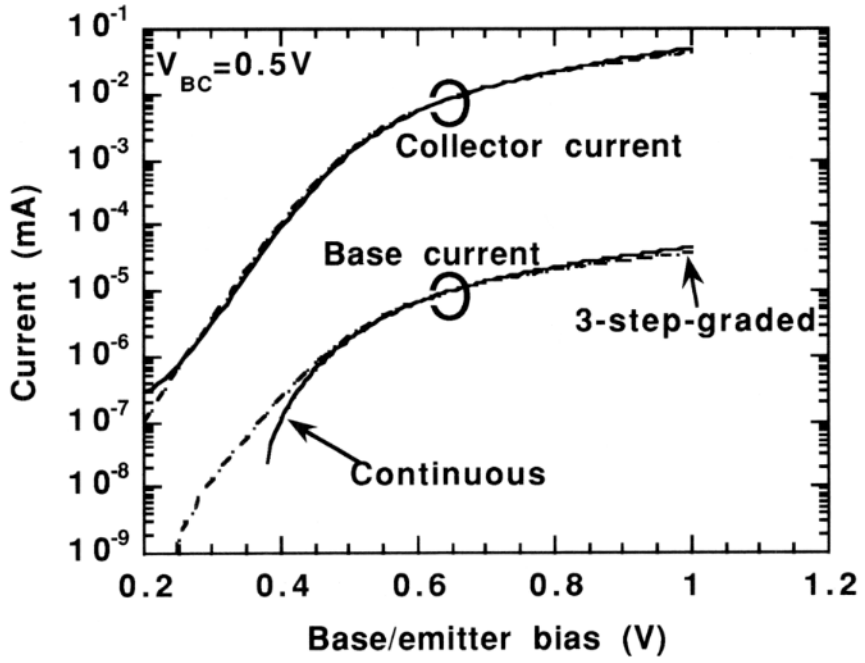

Fig. 3-24. Gummel plots of D-HBT with continuous graded-InGaAsP structure together with step-like graded layers.

3.3 Summary

I have searched out how to manipulate a combination of InGaAsP and GaAs, of which compositional controllability turns out to be good in the low-pressure MOCVD apparatus dedicated to this study. What should be noteworthy is a compositionally immiscible region to emerge during the MOCVD growth of InGaAsP layers on a GaAs substrate — to be caught by sight, using PL measurements. A slight modification of the growth condition has paved the way for growing graded-InGaAsP structures to realize aluminum-free 980-nm GRIN-SCH lasers.

Experimentally, the effect of graded bandgap structure was confirmed, and the nature of graded-InGaAsP interface was characterized, based on InP/InGaAs D-HBTs, each having step graded InGaAsP layers inserted between the InGaAs base and InP collector. I have verified that inserting the graded layers was capable of suppressing the hetero-interface spikes effectively, without any increase of recombination-generation center in a graded-InGaAsP region.

References

[1] M. Irikawa, T. Ijichi, I. J. Murgatroyd, N. Matsumoto, A. Nakai and S. Kashiwa, "Sharp interfaces in GaInAsP/InP single quantum wells grown by MOVPE," *J. Crystal Growth*, vol.93, pp. 370-375, 1988.

[2] A. Iketani, M. Ohkubo, T. Ijichi and T. Kikuta, "First fabrication of continuously graded InGaAsP on GaAs for 0.98μm lasers," *5th InP and Related Materials, Paris*, 1993, WF4.

[3] H. Seki and A. Koukitsu, "Thermodynamic analysis of metalorganic vapor epitaxy of III-V alloy semiconductors," *J. Crystal Growth*, vol. 74, pp. 172-180, 1986.

[4] H. Seki and A. Koukitsu, "Thermodynamic analysis of the MOVPE growth of quaternary III-V alloy semiconductors," *J. Crystal Growth*, vol. 74, pp. 181-186, 1986.

[5] H. Seki and A. Koukitsu, "Thermodynamic analysis of the MOVPE growth process," *J. Crystal Growth*, vol. 76, pp. 233-242, 1986.

[6] S.Tanaka, K.Hiramatsu, Y.Habu, N.Sawaki and I.Akasaki, "Initial stage of LPE growth of InGaAsP on GaAs in the region of immiscibility," *J. Crystal Growth*, vol. 79, 1986, pp.978-983.

[7] K. Onabe, "Calculation of miscibility gap in quaternary InGaPAs with strictly regular solution approximation," *Jpn. J. Appl. Phys.*, vol. 21, no. 5, pp. 797-798, 1982.

[8] K. Hiramoto, T. Tsuchiya, M. Sagawa and S. Tsuji, "Evaluation of InGaAsP crystal on GaAs by low pressure MOCVD," *IEICE, Optical and Quantum Electronics*, OQE92-149, Oct., 1992.

[9] H. Kroemer, "Heterostructure bipolar transistors and integrated circuits," *Proc. IEEE*, vol. 70, no. , pp. 13-25, 1982.

[10] O. Sugiura, A. G. Dentai, C. H. Joyner, S. Chandrasekhar and J. C. Campbell, "High-current-gain InGaAs/InP double-heterojunction bipolar transistors grown by metalorganic vapor phase," *IEEE Electron Device Lett.*, vol. EDL-9, no.5, pp. 282-284, 1988.

[11] E. Tokumitsu, A. G. Dentai, C. H. Joyner, and S. Chandrasekhar, "InP/InGaAs double heterojunction bipolar transistors grown by metalorganic vapor phase epitaxy with sulfer delta doping in the collector region," *Appl. Phys. Lett.*, vol. 57, pp. 2841-2843, 1990.

[12] R. N. Nottenburg, J. C. Bischoff, M. B. Panish and H. Temkin, "High-speed InGaAs(P)/InP double-heterostructure bipolar transistors," *IEEE Electron Device Lett.*, vol. EDL-8, no.6, pp. 282-284, 1988.

[13] W. T. Tsang, A. F. J. Levi and E. G. Burkhardt, "GaInAs/GaInAsP/InP heterostructure bipolar transistors with very thin base (150 Å) grown by chemical beam epitaxy," *Appl. Phys. Lett.*, 53, pp. 983-985, 1988.

[14] D. Ritter, R. A. Hamm, A. Feygenson, H. Temkin and M. B. Panish, "Bistable hot electron InP/GaInAs composite collector heterojunction bipolar transistors," *Appl. Phys. Lett.*, 61, pp. 70-72, 1992.

[15] E. F. Chor and C. J. Peng, "Composition step-graded collector InP/InGaAs/InP DHBT for minimised carrier blocking," *Electron. Lett.*, vol. 32, pp. 1409-1410, July 1996.

[16] K. Kurishima, H. Nakajima, S. Yamahata, T. Kobayashi and Y. Matsuoka, "Effects of compositionally graded $InGa_XAs_{1-X}$ base in abrupt-emitter InP/InGaAs HBTs," *Int. Conf. Solid State Devices and Materials*, Yokohama, 1994, C-6-1.

[17] M. Ohkubo, N. Ikeda and T. Ninomiya, "Graded $GaAs_{1-X}P_X$ bases in heterojunction bipolar transistors with InGaP emitters," *Microwave and Optical Technology Letters*, vol. 11, no. 3, pp.150-153, 1996.

Chapter 4

Fabrication of High-Power Lasers with Graded-InGaAsP Structures

This chapter describes the superiority of a GRIN-SCH system for an aluminum-free 980-nm quantum well laser with an InGaP cladding overall. In this chapter, 'GRIN-SCH structure' denotes Graded Bandgap Structure and Graded Refractive Index Waveguide consisting of InGaAsP layers. Section 4.3 deals with effects of the graded bandgap structures upon the the series-resistance of a laser, and the efficiency of carrier injection into quantum well. Section 4.3.3 casts light on a low series-resistance laser with a high carrier-injection efficiency, which has performed successfully in high-power operation.

An InGaP/GaAs system with a large difference in refractive indices between GaAs and InGaP may cause wide transverse beam divergence. A coupling efficiency with a single-mode fiber (SMF) carries serious weight with practical application to EDFAs, because its core diameter measures as minute as round 10 μm, and its cutoff wavelength is shorter than that of any conventional EDFA pumped by a 1480-nm source. Section 4.4 enters into a waveguide of controlled, refractive indices, made up of step-wise or continuously graded-InGaAsP alloys, which performs efficiently in narrowing down the transverse beam divergence. As a consequence, the coupling efficiency with a SMF has a leap of improvement, and the optical power density is reduced at facets — higher reliability.

4.1 Fabrication Process of Polyimide Buried Ridge Waveguide Lasers

In view of operational reliability, a buried hetero-structure, having its active layer exposed to the ambient air in the process of fabrication, is undesirable for GaAs-based lasers, considering its high surface-recombination velocity in the foregoing structure. A ridge waveguide laser is an adequate candidate to approach the reliability requirement. Moreover, high-power lasing operation needs high thermal conductivity to bring out rapid heat dissipation with a junction-down configuration. Then a planar-structure acts to advantage for a narrow-stripe geometry laser. Yet in addition, high coupling efficiency with an SMF, requires a mesa of narrow width to emit with a circular beam. In an attempt to meet all requirements, the reverse-mesa-shaped ridge waveguide laser buried by polyimide was investigated allowing for stripe geometry lasers.

To safeguard high-power operation against Catastrophic Optical Damage (COD) — sudden failure — as well-known, current-blocked regions were employed in the vicinity of cavity facets [1].

The fabrication process of a polyimide buried ridge waveguide laser [2] follows the proceeding as given below or in Fig. 4-1:

(a) A <110> oriented ridge mesa to be formed by selective chemical etching process

(b) The ridge mesa in (a) to be buried by polyimide, overhead

(c) With the polyimide cured, a p^+-GaAs contact layer to be bared by reactive ion beam etching (RIBE) technique in O_2 plasma

(d) Ti/Pt/Au to be deposited on the surface

(e) With the substrate thinned to 120 μm, AuGeNi/Au to be deposited on the n-side

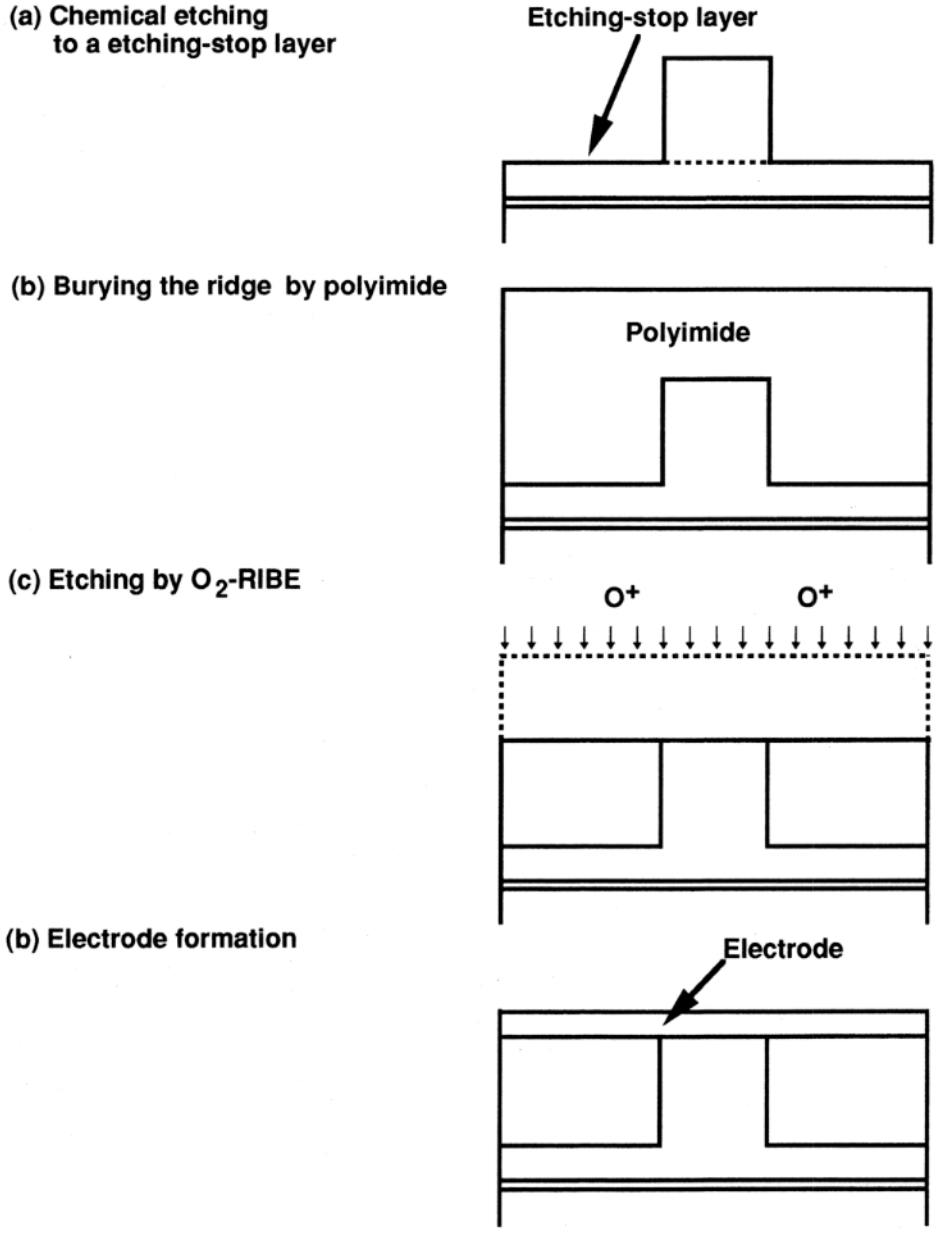

Fig. 4-1. Fabrication process of a polyimide buried ridge waveguide laser.

Figure 4-2 presents a Scanning Electron Micrograph (SEM) image of a cross-sectional polyimide buried ridge waveguide laser. Here it is indispensable to high coupling efficiency with a SMF to be equipped with a narrow mesa for a circular beam pattern. A bottom width of a representative ridge mesa is controlled as narrow as 2 μm.

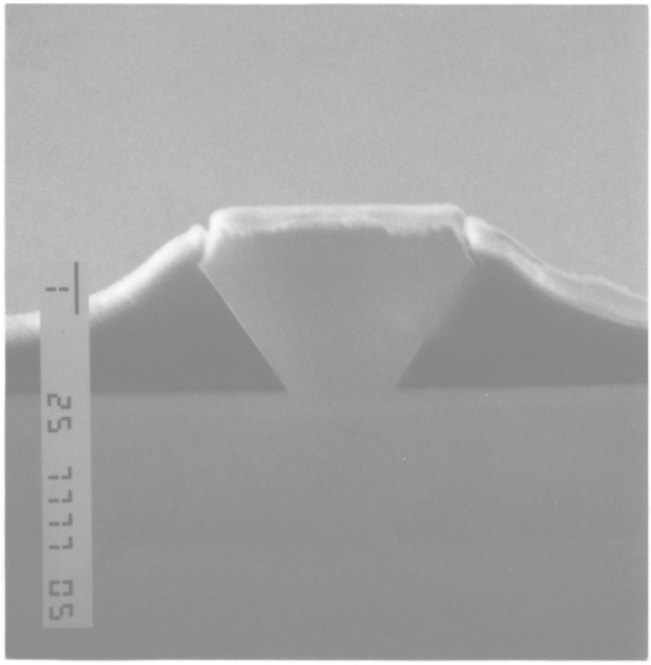

Fig. 4-2. SEM image of a cross-sectional reverse-mesa-shaped polyimide buried ridge waveguide laser.

4.2 Performance of Basic Structures with Undoped (GRIN-)SCH

4.2.1 Epitaxial Structurs

The following is epitaxial layers [3], which were dedicated to the first demonstration of a 980-nm InGaAs/GaAs SCH strained-layer single quantum well laser with InGaP cladding layers.

The layers consist of

i) n-GaAs buffer layer,
ii) n-InGaP cladding layer,
iii) undoped GaAs SCH layer,
iv) SL-SQW active layer,
v) undoped GaAs SCH layer,
vi) p-InGaP cladding layer,
vii) heavily doped p^+-GaAs contact layer.

The amount of strain in the well was calculated to be 1.5 % in lasing at 980 nm. The well was adjusted to less than a critical layer thickness predicted with Matthews and Blakeslee model [4]. A 3-nm-thick p-GaAs layer is inserted in the upper cladding layer so as to fabricate ridge waveguide lasers. The etching process utilizes the GaAs layer — an etching-stop layer — with a selective chemical etchant.

As considered in Chapter 2, a graded-InGaAsP structure is effective for suppressing heterointerface spikes at InGaP/GaAs. The following is the epitaxial structure [1], along with undoped GRIN-SCH waveguide around the active region (Fig. 4-3).

The layers consist of

i) n-GaAs buffer layer,
ii) *n-InGaAsP graded layers*,
iii) n-InGaP cladding layer,
iv) *undoped InGaAsP graded layers*,
v) undoped GaAs SCH layer,
vi) SL-SQW active layer,
vii) undoped GaAs SCH layer,
viii) *undoped InGaAsP graded layers*,
ix) p-InGaP cladding layer,
x) *p-InGaAsP graded layers*, and
xi) heavily doped p^+-GaAs contact layer,

where each graded region consists of three-step InGaAsP layers with a bandgap of Eg = 1.77 eV, 1.65 eV and 1.58 eV.

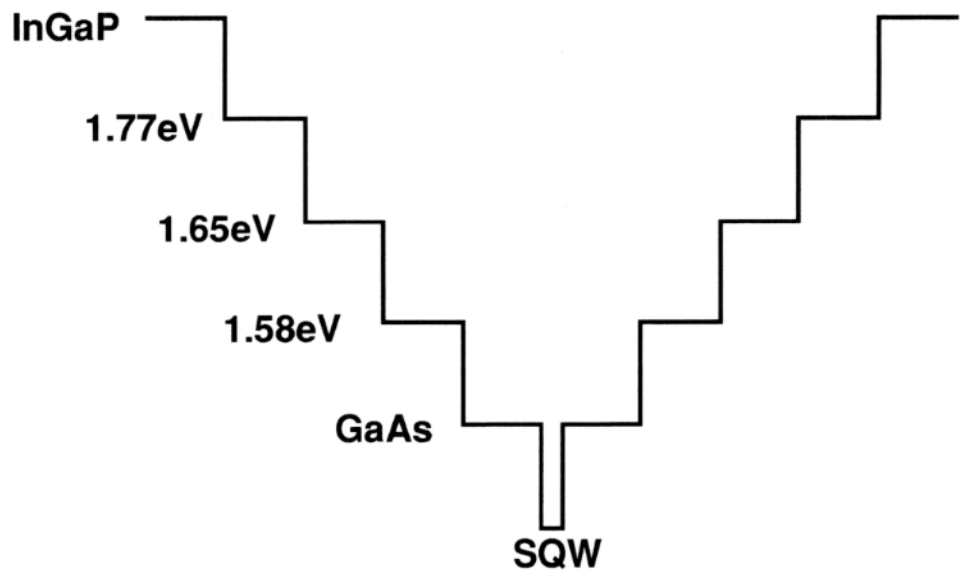

Fig. 4-3. Schematic diagram of GRIN-SCH structure.

4.2.2 Performance

Broad-area lasers were fabricated in the wake of epitaxial growth so as to measure threshold current density (J_{th}). In brief, 100-μm-wide broad-area lasers being 100 μm in width were fabricated by etching off the p^+-GaAs contact layer.

Figure 4-4 plots threshold current density (J_{th}) as a function of cavity length. The straight-lines are fitted to the plots. J_{th} values are both estimated to be as low as 60 A/cm^2 at the infinite cavity lengths, where no excess nonradiative recombination centers exist in those graded layers. In Fig. 4-4, a straight-line refers to a logarithmic current-gain relationship [5].

Figure 4-5 plots inverse external differential quantum efficiency as a function of cavity length in polyimide-buried ridge waveguide lasers with no facet coating. It can be learned from the plots that both lasers should have approached 100 % in internal quantum efficiency (η_i), where the internal loss (α_i) did not exceeded 5 cm^{-1} in SCH lasers or 3 cm^{-1} in GRIN-SCH lasers. GRIN-SCH lasers with thinner GaAs layers in a GRIN-SCH region seems to be low in the absorption loss. Then further improvement is expected without GaAs SCH layers [6,7].

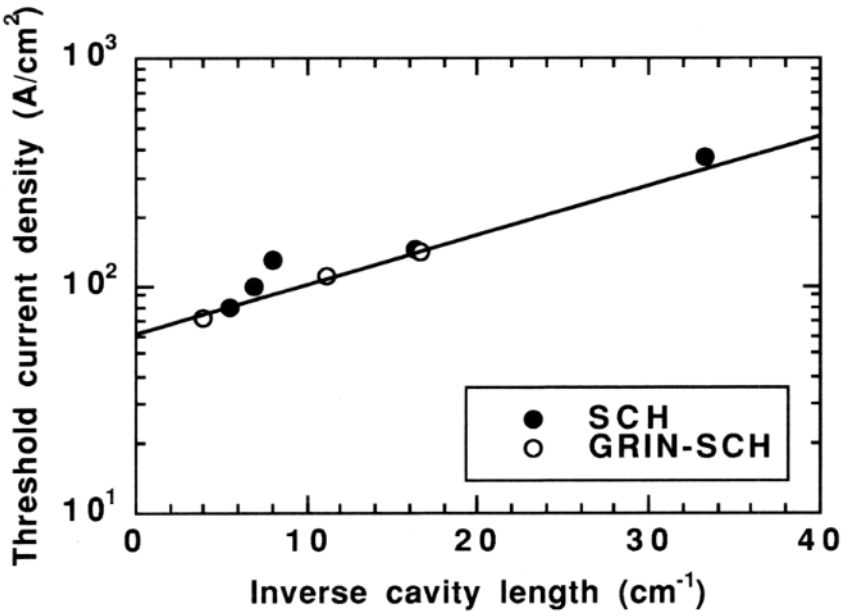

Fig. 4-4. Threshold current density as a function of cavity length.

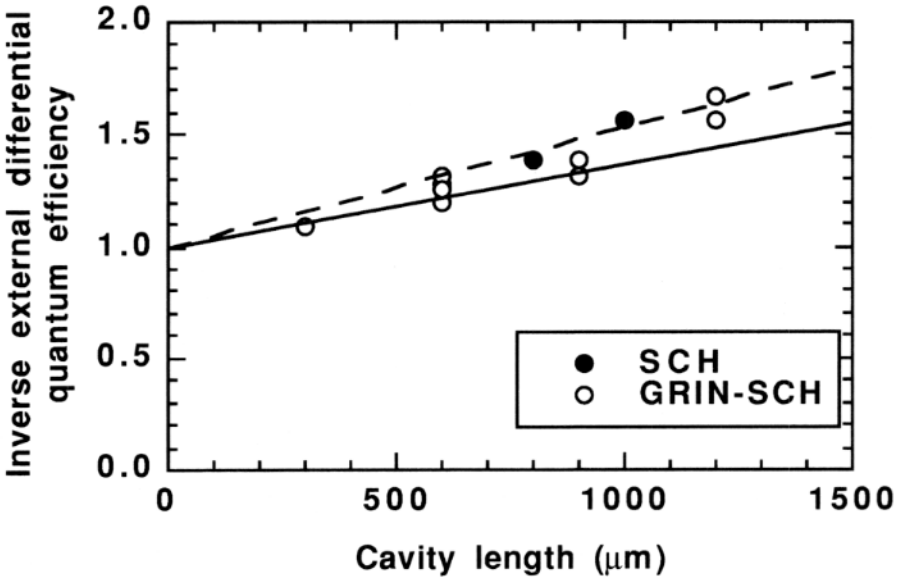

Fig. 4-5. Inverse external differential quantum efficiency as a function of the cavity length.

4.3 Advantages of Graded Bandgap Structures

4.3.1 Low Series Resistance

Chapter 2 describes the effective number of the graded-InGaAsP inserted into an InGaP/GaAs heterojunction so as to reduce heterojunction spikes. Three lasers were prepared in proof of decrease of spikes.

Figure 4-6 characterizes the three lasers in epitaxial structure. An 'SCH-I' laser involves two abrupt junctions of p+-GaAs(contact)/p-InGaP(cladding) and p-InGaP(cladding)/GaAs(active). An 'SCH-II' involves a graded p+-GaAs(contact)/p-InGaAsP/p-InGaP(cladding) junction and an abrupt p-InGaP(cladding)/GaAs(active) junction. By contrast, a 'GRIN-SCH' laser involves two graded junctions of p+-GaAs(contact)/p-InGaAsP/p-InGaP(cladding) and p-InGaP(cladding)/p-InGaAsP/GaAs (active). In effect, the graded InGaAsP regions consisted of three InGaAsP layers as lattice-matched to GaAs, which have a bandgap of Eg = 1.77 eV, 1.65 eV, and 1.58 eV as mentioned in Chapter 3. The graded p-InGaAsP and p-InGaP layers were doped by 1×10^{18} cm^{-3}, while the p-GaAs layers were doped by 1×10^{19} cm^{-3} or more for nonalloyed Ti/Pt/Au metalization.

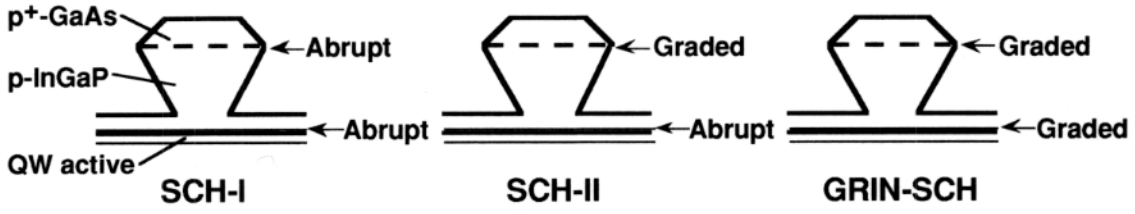

Fig. 4-6. Characterized epitaxial structures.

Figure 4-7 draws current/voltage curves representative of those three types of lasers in response to input signal pulses. The devices were each equipped with waveguides having ridge 3 μm in width and 1 mm in length, but with no facet coatings. Series resistance was estimated to be as high as 7 Ω for 'SCH-I', where, as low as 3 Ω for 'GRIN-SCH'. Inserted step-graded InGaAsP layers make series resistance melt down to be a fair approach to that in an ideal continuously graded junction [8]. It is because, as described in Section 2.3.1, a step-graded junction got rid of heterojunction spikes.

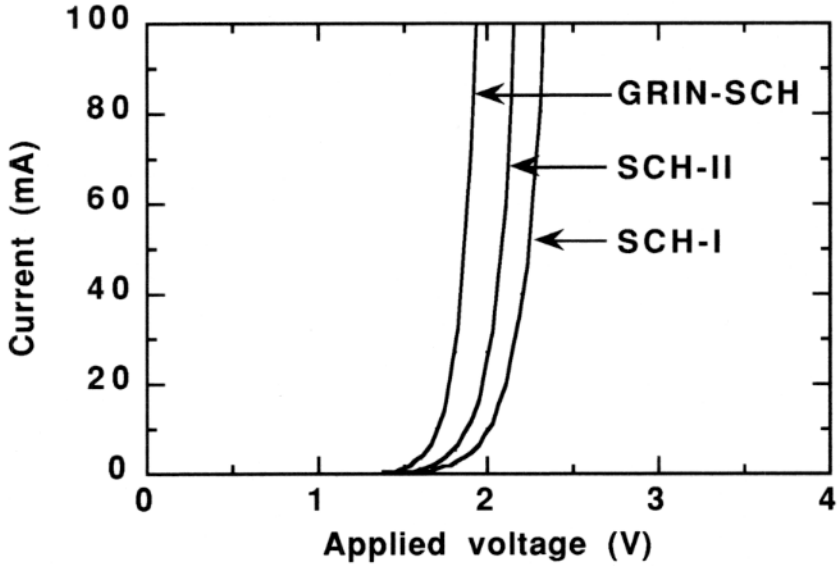

Fig. 4-7. Current/voltage characteristics of three types of lasers.

4.3.2 High Carrier Injection Efficiency

In the wake of Chapter 2 that deals with how the electric field in a change of bandgap in an SCH region — the counterpart of GRIN-SCH — affect the lasing characteristics, this section presents experimental results of temperature characteristics of the optimum-design GRIN-SCH waveguide.

Figure 4-8 shows conduction band profiles of four SCH lasers, with InGaP cladding layers, single step SCH laser [2]: Step-SCH, 4-step-GRIN-SCH [1]: GRIN-SCH-I, 3-step-GRIN-SCH [9]: GRIN-SCH-II and continuous-GRIN-SCH [8]: GRIN-SCH-III. Consequently, Step-SCH and GRIN-SCH-I involve a GaAs barrier; GRIN-SCH-II and GRIN-SCH-III have an InGaAsP barrier with a bandgap of 1.58 eV. All layers have a 9-nm-thick InGaAs single quantum wells in their active layers. Table 4-1 pinpoints particulars of those waveguide structures.

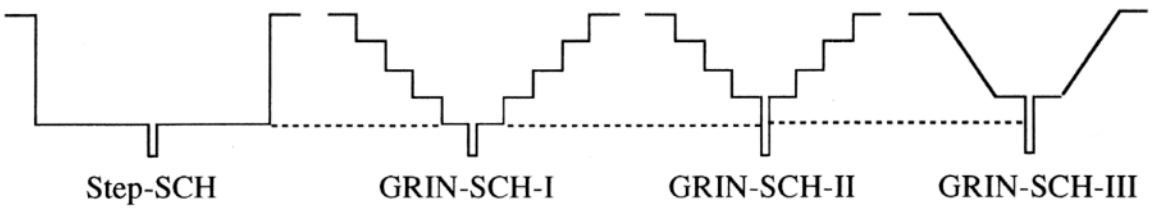

Fig. 4-8. Schematic conduction band profile of four SCH lasers with InGaP cladding layers.

Table 4-1. The details and labeling of SCH structures.

	Eg1 (1.42eV)	Eg2 (1.58eV)	Eg3 (1.65eV)	Eg4 (1.77eV)
Step-SCH	45nm	---	---	---
GRIN-SCH-I	20nm	20nm	20nm	20nm
GRIN-SCH-II	---	20nm	20nm	20nm
GRIN-SCH-III	---	25nm	20nm, continuous	

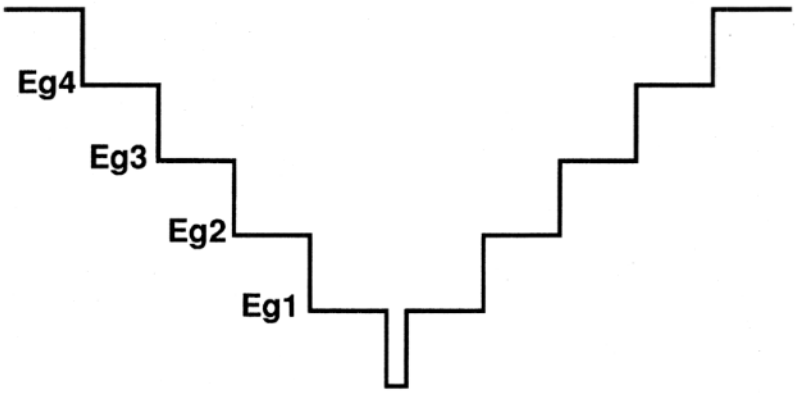

Figure 4-9 shows light/current characteristics of (a) Step-SCH and (b) GRIN-SCH-II. Each device had a ridge waveguide measuring 2~3 μm in width and 1.2 mm in length; one facet was coated with a low-reflective (7 %) SiN layer, and the other one was coated with three pairs of Si/SiN dielectric layers for high-reflectivity (95 %). It can be learned from there, that the GRIN-SCH-II laser greatly surpasses the Step-SCH in threshold current and slope efficiency. The characteristic details of the four SCH lasers are as follows:

Figure 4-10 plots threshold current of the four SCH lasers in cw conditions as a function of temperature. The dependence of threshold current on temperature can be expressed as:

$$I_{th}=I_0\exp\left(\frac{T}{T_0}\right), \tag{4-1}$$

where I_0, T_0 are constants, and I_{th} is threshold current. Values of T_0 were measured in a temperature range of 10-70 ℃: 125 K for Step-SCH, 175 K for GRIN-SCH-I, stand-out 291 K for GRIN-SCH-II, and also stand-out 307 K for GRIN-SCH-III, respectively. Figure 4-11 shows normalized slope efficiency of these lasers as a function of temperature in cw conditions. The normalized slope efficiency decreases in connection with temperature rise. By way of illustration, a normalized slope efficiency ($\eta_{T=70℃}/\eta_{T=10℃}$) at 70 ℃ was estimated at 0.75 for Step-SCH, 0.82 for GRIN-SCH-I, superlative 0.90 K for GRIN-SCH-II, and also superlative 0.90 for GRIN-SCH-III. Here it is noteworthy that less dependency on temperature emerged at higher T_0 values. Table 4-2 lists comparison in characteristics of four SCH lasers.

Table 4-2. Comparison in characteristics of four SCH lasers.

	T_0 (K)	$\frac{\eta_{T=70℃}}{\eta_{T=10℃}}$
Step-SCH	**125**	**0.75**
GRIN-SCH-I	**175**	**0.82**
GRIN-SCH-II	**291**	**0.90**
GRIN-SCH-III	**307**	**0.90**

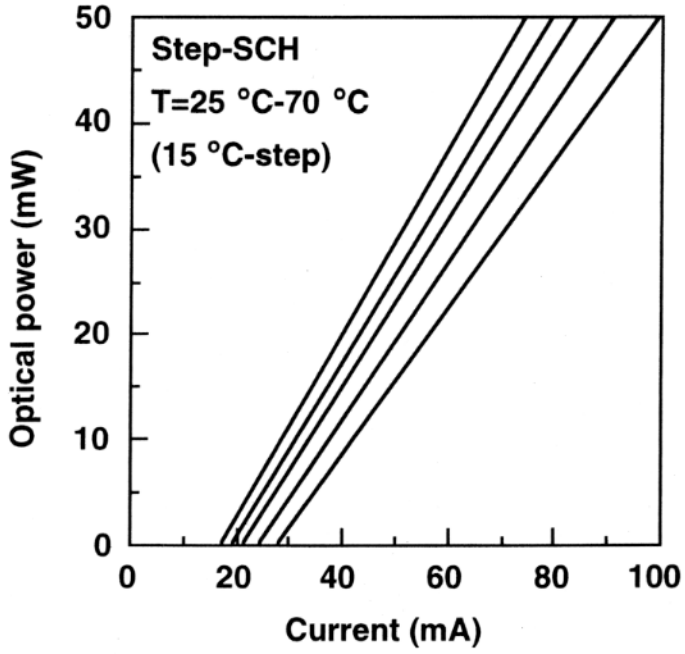

(a) Step-SCH.

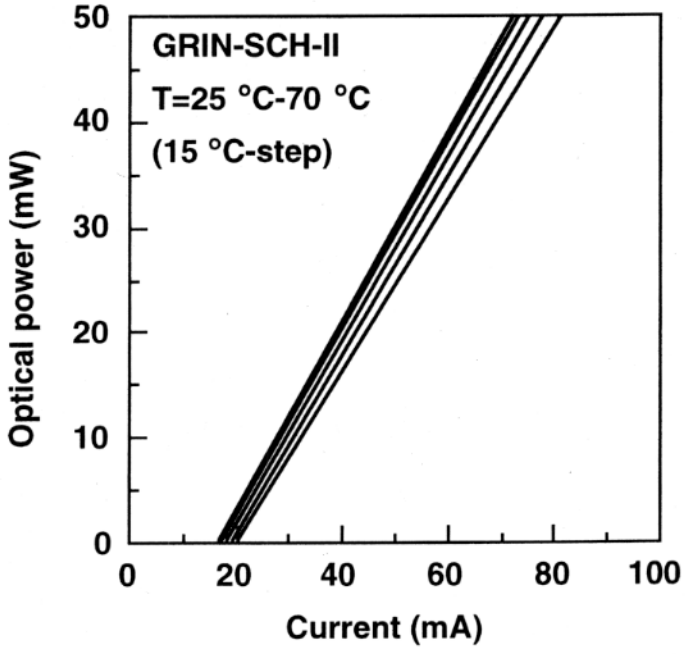

(b) GRIN-SCH-II.

Fig. 4-9. Light/current characteristics of (a) Step-SCH and (b) GRIN-SCH-II.

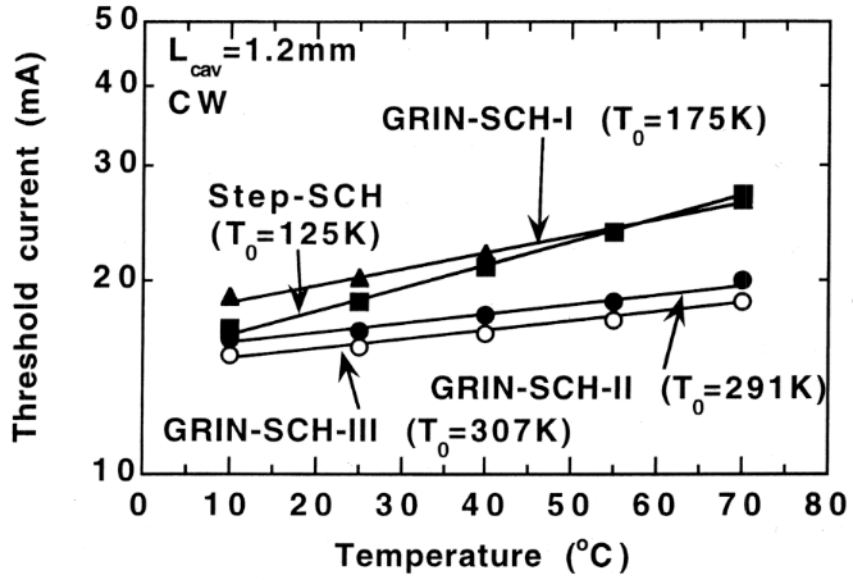

Fig. 4-10. Threshold currents of the four SCH lasers as a function of temperature.

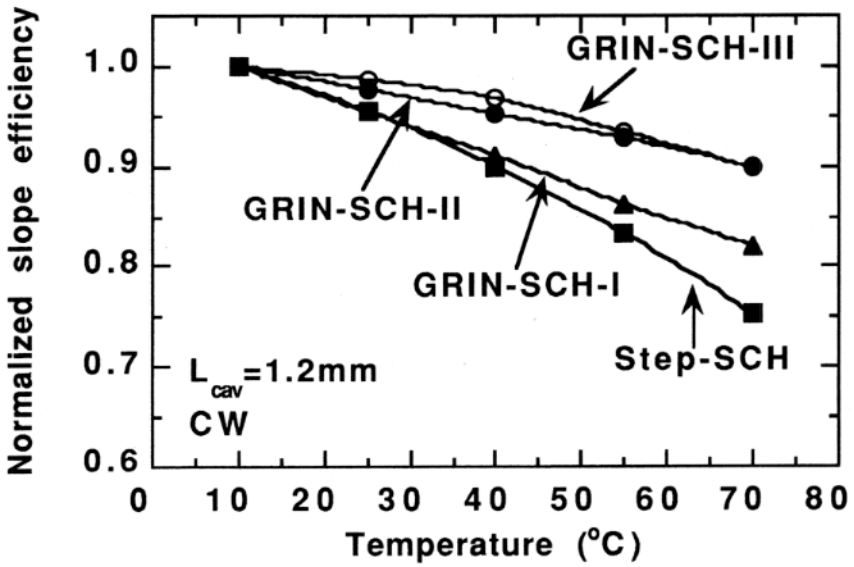

Fig. 4-11. Normalized slope efficiency of the four SCH lasers as a function of temperature.

On analysis, I surmise that those findings can be linked up with the carrier injection efficiency into the quantum well active region, as described in Section 2.3.2. Figure 4-12 presents the normalized factor of electron population in a quantum well as a function of temperature. Term "n_{QW} and n_{SCH}" denotes the carrier density in a quantum well and SCH region; parameters were cited from Section 2.3.2 to derive virtual figures; GRIN-SCH sections were structured linearly.

Bringing out the contrast between Step-SCH and GRIN-SCH-I lasers, the simple step SCH section uniformizes the carrier distribution in the GaAs layers, while the internal electric field arising from the GRIN-SCH-I's graded bandgap concentrates carriers upon the InGaAs single quantum well [10]. This concentration restrains carriers from leaking out toward the optical confinement layers — more likely carrier at higher temperatures. With a similar approach to GRIN-SCH-I and GRIN-SCH-II lasers, the barrier height of an InGaAs/InGaAsP system in GRIN-SCH-I is higher than that of an InGaAs/GaAs in GRIN-SCH-II, where carriers are restrained from the leaking out toward the optical confinement layers, as well. In the process of depicting Fig. 4-12, the quantum well of GRIN-SCH-II or -III was assumed to be 0.1 eV deeper than that of Step-SCH or GRIN-SCH. Since the only carriers in a quantum well contribute to lasing, it becomes available to single out a laser with quantum wells being higher in T_0.

In addition, the propensity of slope efficiency to depend on temperature in Fig. 4-11 might correlate with an increase in internal loss incurred, because of a rise in the population of free carriers overflown to the SCH region, as explained in Section 2.3.2. Free carriers in a quantum well and waveguide region can lead into light absorption. Thus, neglecting the light absorption in the cladding layers, the internal loss, arising from free-carrier light absorption, is figured out as:

$$\alpha_i=\sigma_n(\Gamma_{QW}n_{QW}+\Gamma_{SCH}n_{SCH})+\sigma_p(\Gamma_{QW}p_{QW}+\Gamma_{SCH}p_{SCH}), \qquad (4\text{-}2)$$

where Γ_{QW} and Γ_{SCH} are optical confinement factor in quantum well and SCH region, and p_{QW} and p_{SCH} indicate carrier density in quantum well and SCH region. Free electron and hole absorption loss is expressed as σ_n and σ_p. Figure 4-13 shows normalized $\Gamma_{QW}n_{QW}+\Gamma_{SCH}n_{SCH}$ as a function of temperature, which correlated with the internal loss to be set rising by an increase in the population of free carries overflown to the SCH region. The propensity of a laser to decrease in differential quantum efficiency abreast with temperature rise, allowed us to determine the dependence of slope efficiency on temperature, as given in Fig. 4-11.

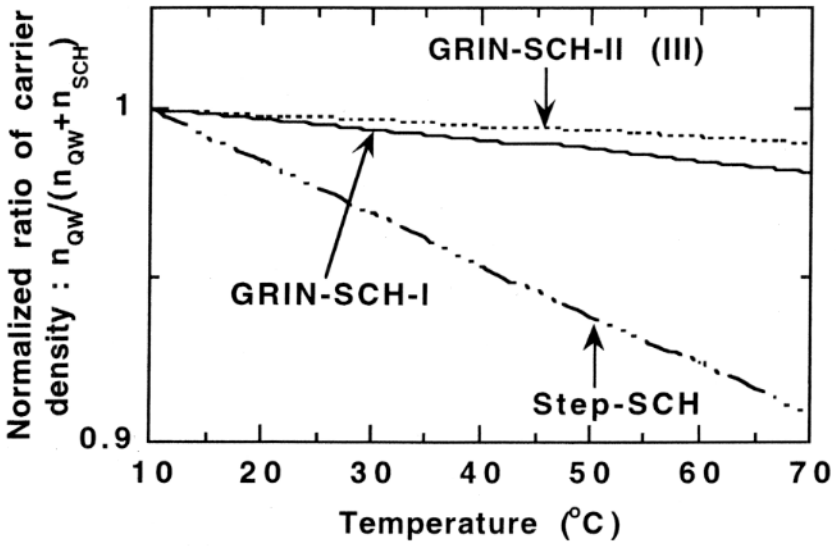

Fig. 4-12. Calculated ratio of the electron population as a function of temperature. n_{QW} and n_{SCH} indicate the carrier density of carrier in quantum well and SCH region. The depth of the quantum well of GRIN-SCH-II (III) is 0.1 eV deeper than that of Step-SCH and GRIN-SCH.

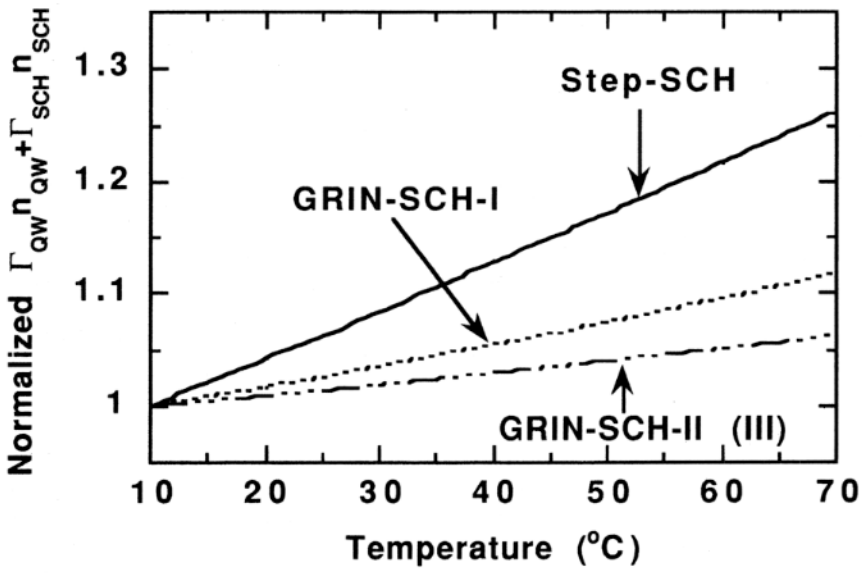

Fig. 4-13. Normalized $\Gamma_{QW}n_{QW}+\Gamma_{SCH}n_{SCH}$ as a function of temperature.

4.3.3 High-Power Operation

The above findings gave rise to a conclusion that a graded-bandgap waveguide with a wide bandgap barrier serves to produce low series resistance and high carrier injection efficiency. Its performance can be enough to sustain high-power operation. Figure 4-14 shows a light/current characteristic of a laser (1-mm-long and 3-μm-wide) with a 3-step-GRIN-SCH waveguide in cw conditions at 25 ℃. Each InGaAsP layer of the GRIN-SCH waveguide was 20 nm in thickness. The front facet was coated to be a low-reflective (5 %) SiN layer, and the rear, to be three pairs of a-Si/SiN dielectric layers as attached with 95 % of high reflectivity. That laser was mounted on a Si heat sink with junction down configuration, exhibiting a threshold current of as low as 18 mA and a slope efficiency of as high as 0.95 W/A. It should be noteworthy that output power linearly increases by and large, and clears 350 mW with some margin at 500 mA. This kink-free behavior results from the suppression of beam-steering [14, see appendix B].

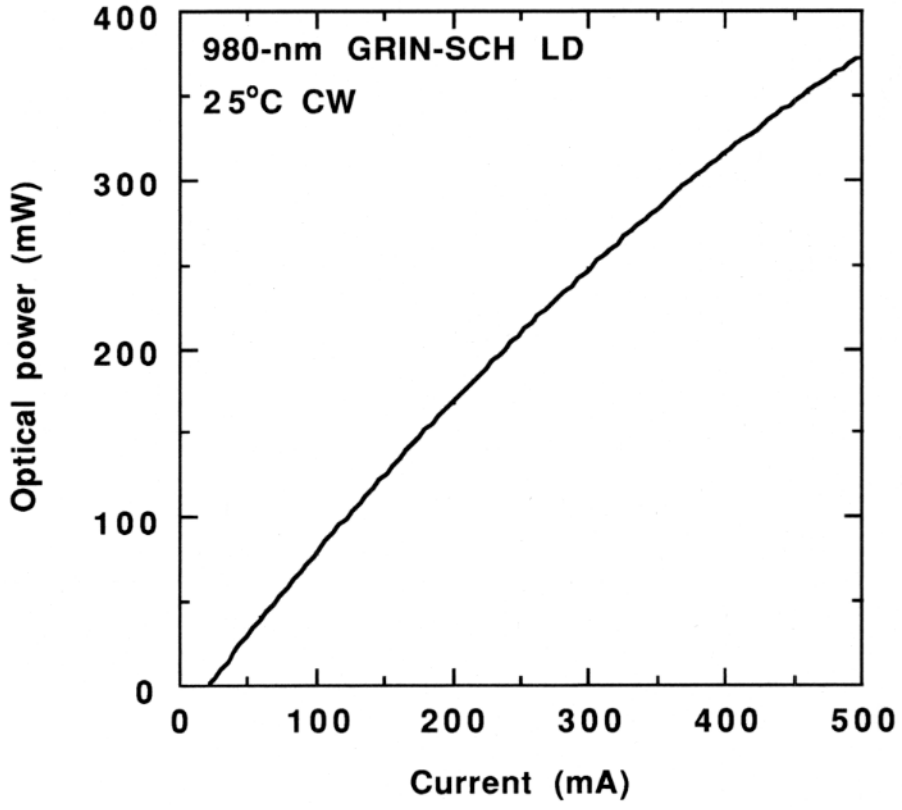

Fig. 4-14. Light/current characteristic of 1mm-long and 3-μm-wide laser with 3-step-GRIN-SCH waveguide at 25 ℃.

4.4 Controlled Graded Refractive Index Waveguides

4.4.1 High Coupling Efficiency into A SMF

High-power semiconductor lasers with symmetric and narrow beams are of great interest to those work on the fiber-optics, optical data storage or free-space optical interconnection. The utilization of 980-nm lasers for EDFAs is not to maximize the optical power from the facets, but to set a coupling with a SMF. But then, it is recognized far and wide, that ridge waveguide lasers are larger in ellipticy as to the far-field patters ($\theta_{\perp}/\theta_{//}$), than the others (e.g., 1480-nm BH lasers), where high coupling efficiency with SMFs can hardly be yielded. One purposive approach to diminishing transverse beam divergence ($\theta_{\perp}$) is to enlarge the transverse mode size — concurring in reducing the optical power density at facets. Thus, high reliability will result from the decrease in optical confinement factor.

The authentic design procedure for a waveguide in laser cavity can never work out, without having a full grip on the refractive indices of all epitaxial layers. Unfortunately, very few reports have dealt with the refractive indices of InGaAsP on GaAs. By contrast, refractive indices of $In_{1-x}Ga_xAs_yP_{1-y}$ on InP were determined, on the strength of a modified single-effective-oscillator (M-SEO) method [12]. The M-SEO method paves the way for approximating the refractive indices of InGaAsP, by applying the formula:

$$n^2=1+\frac{E_d}{E_0}+\frac{E_d}{E_0^3}E^2+\frac{\eta}{\pi}E^4\ln\left(\frac{2E_0^2-E_g^2-E^2}{E_g^2-E^2}\right), \tag{4.3}$$

where

$$\eta=\frac{\pi E_d}{2E_0^3(E_0^2-E_g^2)}, \tag{4.4}$$

for the photon energy E(=hν), and with:

$$E_0=0.595x^2(1-y)+1.626xy-1.891y+0.524x+3.391, \tag{4-5}$$

$$E_d=(12.36x-12.71)y+7.54x+28.91, \tag{4.6}$$

$$E_g=1.35+0.668x-1.17y-0.758x^2+0.18y^2-0.069xy-0.322x^2y+0.03xy^2. \tag{4.7}$$

The lattice-matching condition to GaAs is:

$$x=\frac{0.216+0.1894x}{0.4184-0.013y}. \tag{4.8}$$

Figure 4-15 draws a curve of calculated values, and plots measured refractive indices at 980 nm by an ellipsometry method. Both the calculated and measured are close enough to each other for working out the waveguide design.

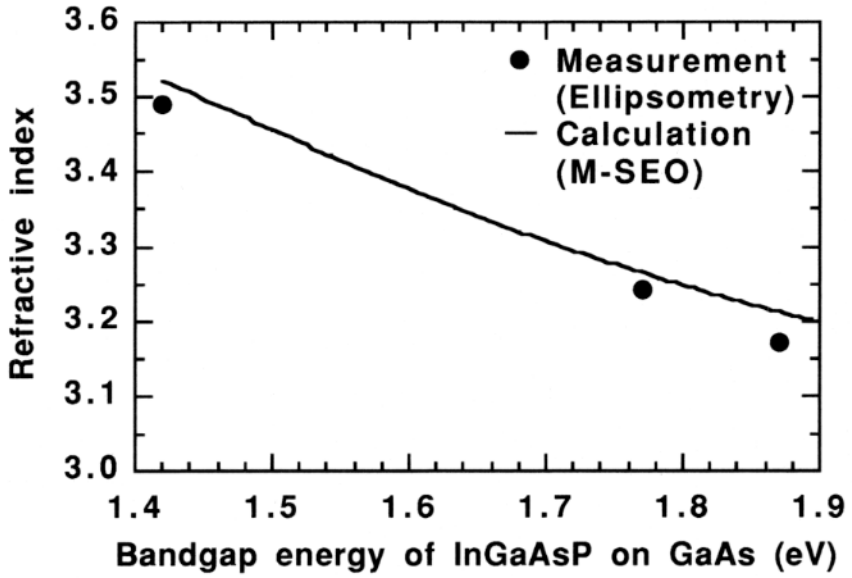

Fig. 4-15. Calculated and measured refractive indices at a wavelength of 980 nm.

Figure 4-16 shows a schematic diagram of the GRIN-SCH waveguide used in the calculation. Maxwell's equation [13] performs in determining the optical field of the N-step or stepwise graded-index. When we put a propagation constant along the z-direction as β and the refractive index of i-th layer as n_i, the optical field distribution: E(y) takes the form of a solution of the Maxwell's equation:

$$\left(\frac{\partial^2}{\partial^2 y} - \beta^2 + n_i^2 \mu_0 \varepsilon_0 \omega^2\right) E(y) = 0 \quad . \tag{4.9}$$

Equation 4.9 is in general modified as:

$$E(y) = A_i \exp\{j\gamma_i (y - y_{i-1})\} + B_i \exp\{-j\gamma_i (y - y_{i-1})\}, \tag{4.10}$$

where γ_i is propagation constant along the y-direction in the i-th layer as:

$$\gamma_i = \sqrt{n_i^2 \mu_0 \varepsilon_0 \omega^2 - \beta^2} \quad . \tag{4.11}$$

The propagation constant is derived, provided that all boundaries in the optical field are fluent for optical propagation, from a matrix out of the Maxwell's equation:

$$\begin{bmatrix} E(y) \\ \dfrac{\partial E(y)}{\partial y} \end{bmatrix} = [T_i(y)] \begin{bmatrix} E(y_{i-1}) \\ \dfrac{\partial E(y_{i-1})}{\partial y} \end{bmatrix}, \tag{4.12}$$

where $T_i(y)$ is a transform matrix:

$$[T_i(y)] = \begin{bmatrix} \cos\{\gamma_i(y-y_{i-1})\} & (1/\gamma_i)\sin\{\gamma_i(y-y_{i-1})\} \\ -\gamma_i\sin\{\gamma_i(y-y_{i-1})\} & \cos\{\gamma_i(y-y_{i-1})\} \end{bmatrix}. \tag{4.13}$$

Here the field converges fluently in the cladding layer; then, a characteristic equation comes into existence:

$$[|\gamma_{-N-1}|, 1][T_N(y_N)][T_{N-1}(y_{N-1})] \cdots [T_{-N}(y_{-N})] \begin{bmatrix} 1 \\ |\gamma_{-N-1}| \end{bmatrix} = 0. \tag{4.14}$$

The optical confinement factor (Γ) in the well is then given by:

$$\Gamma = \frac{\displaystyle\int_{y_{-1}}^{y_1} |E(y)|^2 dy}{\displaystyle\int_{-\infty}^{\infty} |E(y)|^2 dy}. \tag{4.15}$$

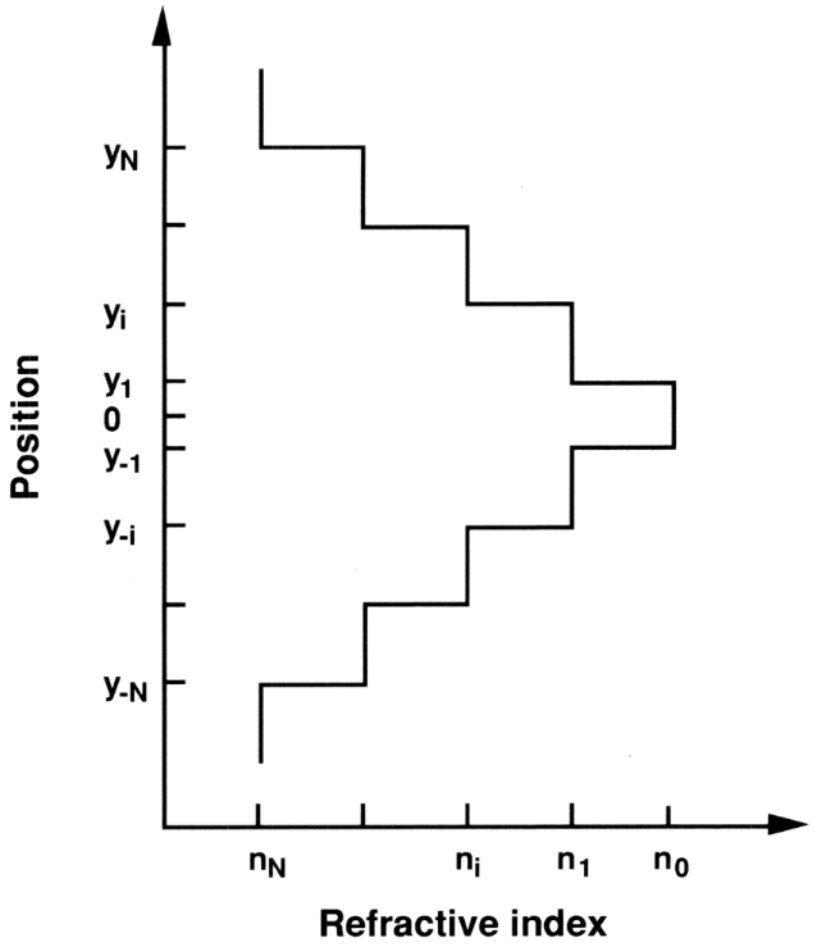

Fig. 4-16. Schematic diagram of the GRIN-SCH waveguide used in the calculation.

Table 4-3 and Figure 4-17 present refractive indices of a 3-step-GRIN-SCH waveguide (cited from calculated values in Fig. 4-15), and the calculated optical field distribution along with optical confinement factors — in a literal order. It was revealed that a decrease in the thickness of InGaAsP-step gave rise to drastic expansion of transverse mode size.

Table 4-3. Refractive index of 3-step-GRIN-SCH waveguide used in the calculation.

	n_0	n_1	n_2	n_3	n_4
Material	**InGaAs**	**InGaAsP**			**InGaP**
Refractive index	**3.67**	**3.42**	**3.34**	**3.25**	**3.16**

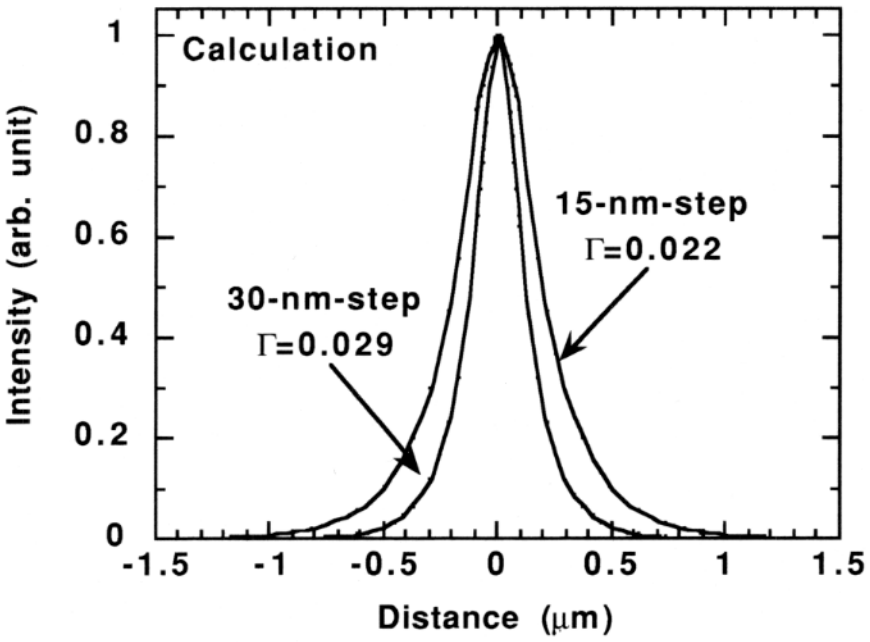

Fig. 4-17. Calculated optical field distribution and optical confinement factor (Γ) of 3-step-GRIN-SCH waveguide.

Where it is possible to figure out the optical field distribution in Fig. 4-17, it is concurrently possible to obtain the far-field patterns by the Fourier transform of the optical field. Figure 4-18 shows far-field patterns together and optical confinement factors. The calculated Full Angle at the Half Maximum (FAHM) is reduced to $\theta_{\perp} = 29^{\circ}$ with a 15-nm-InGaAsP-step. Decreasing the thickness of the InGaAsP-step results in expanding the transverse mode size, and thereby narrows down the beam pattern, but with sacrificing or decreasing the optical confinement factor, as in Fig. 4-19. In brief, some tradeoff takes place between the narrowed transverse beam divergence and decreased optical confinement factor. Lasers with a low optical confinement factor are likely to incur high threshold current or optical gain saturation. Accordingly, the thickness of an InGaAsP-step must be designed with deliberation. Laying emphasis on this tradeoff, I chose a laser with a 15-nm-InGaAsP-step for the high-coupling with an SMF.

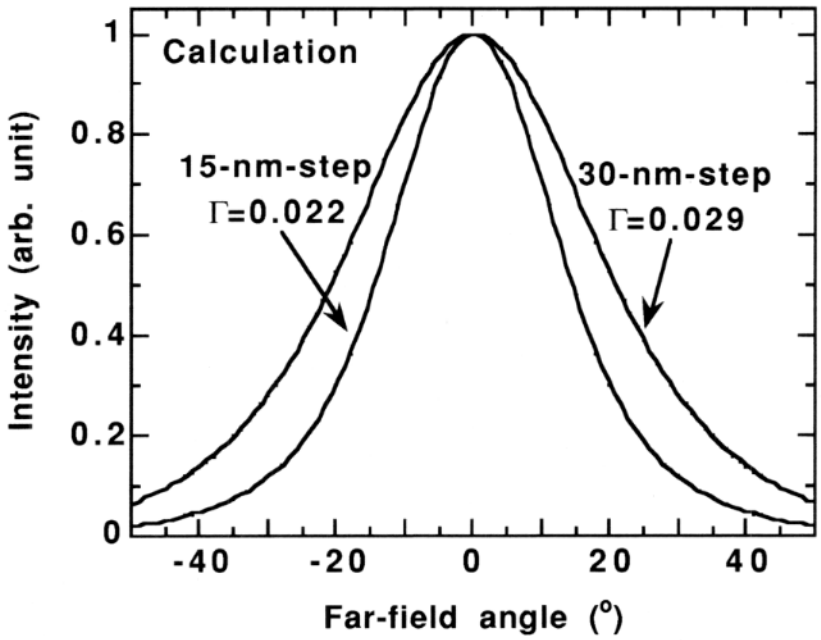

Fig. 4-18. Calculated far-field patterns together and optical confinement factors.

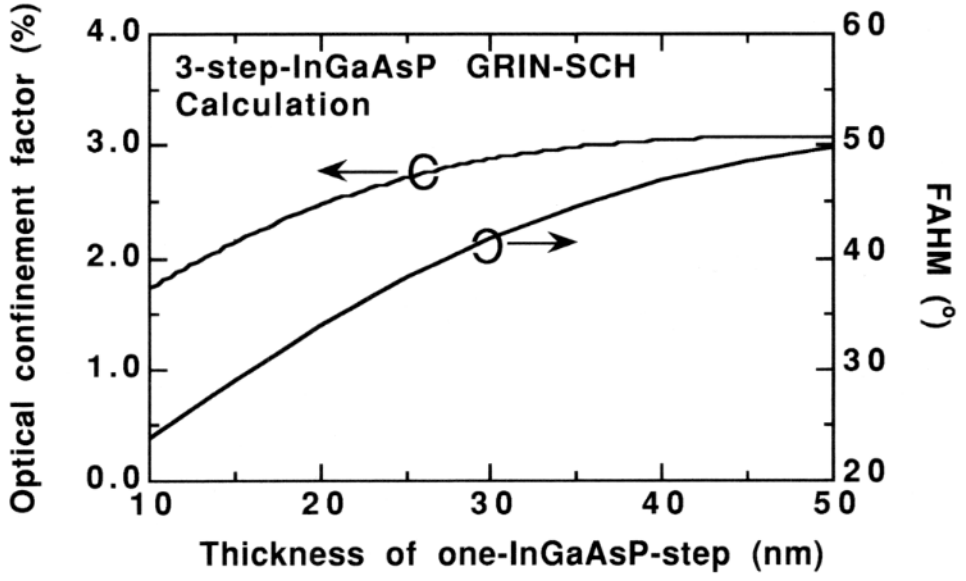

Fig. 4-19. FAHM of transverse beam divergence and optical confinement factor as a function of thickness of one-InGaAsP-step for 3-step-GRIN-SCH waveguide.

Figure 4-20 illustrates a cutaway view of a laser module with a two-lens system [15]. Two lenses are equipped to collimate the laser beam from the facet toward the SMF. The SMF 'FLEXCORE 1060' of Corning Inc. measures 6.2 μm in mode-field diameter and 0.92 μm in cutoff wavelength, and is supported by a ferrule. End facets of the SMF and two lenses are coated with anti-reflection films. The laser chip and lenses are welded onto the package with a YAG laser after an optical alignment.

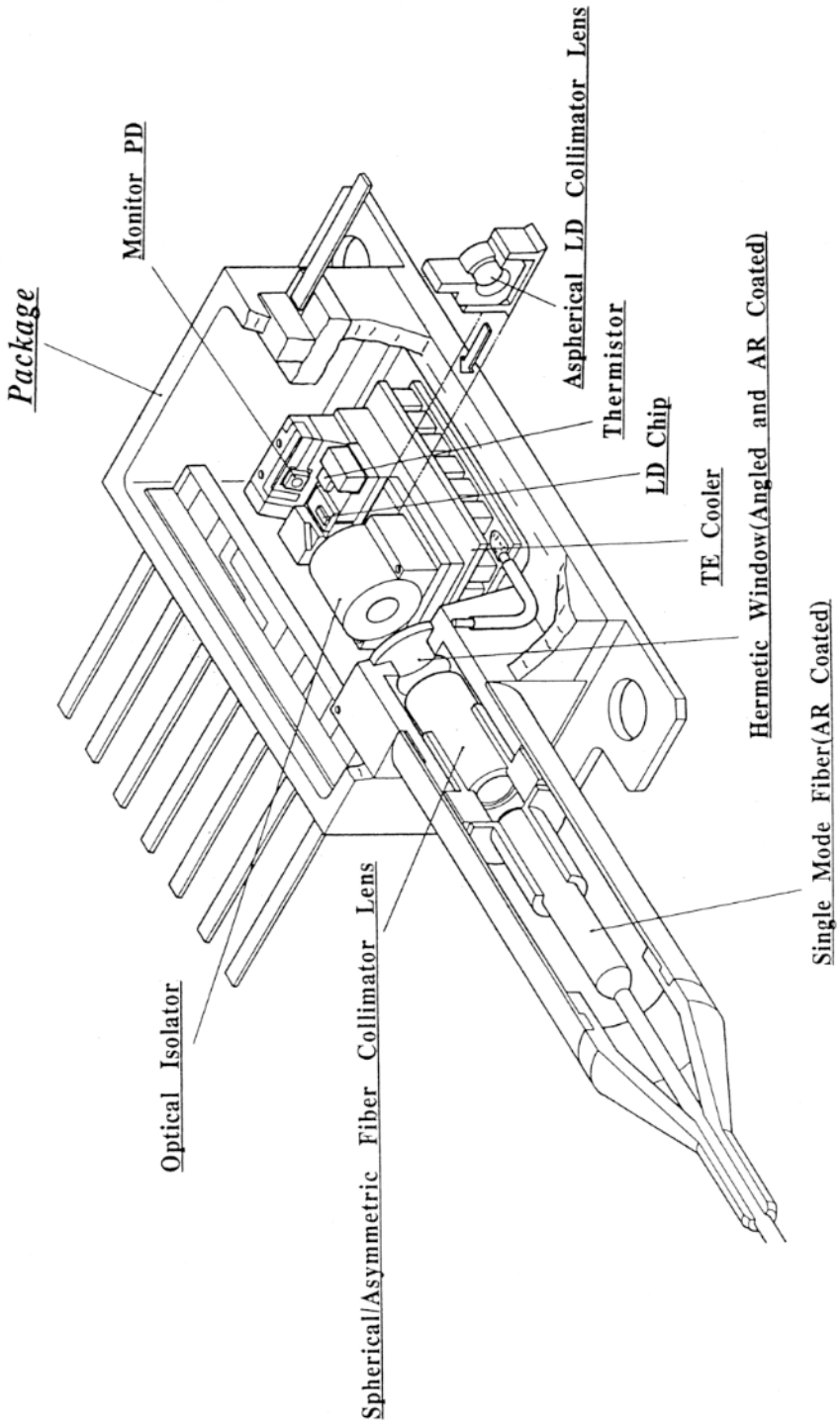

Fig. 4-20. Schematic view of fabricated laser module with a two-lens system [15].

Figure 4-21 shows light/current characteristics in free space (P_0) and the SMF (P_f), which resulted from 3-step-GRIN-SCH laser with a 15-nm-InGaAsP-step in cw conditions at 25 ℃. The LR/HR facet-coated laser was mounted on a Si heat sink with junction-down configuration, where a threshold current of 28 mA and a slope efficiency of 0.88 W/A came into existence. The inset shows far-field patterns of this laser, which reached an optical power of stand-out 240 mW in free space at a driving current of 300 mA. The lateral and transverse angle of the FAHM measured $\theta_{//} = 12^\circ$ and $\theta_{\perp} = 24^\circ$. Ellipticity ratio of far-field pattern ($\theta_{\perp}/\theta_{//}$), being as low as round 2, gave rise to a fall up to 2.22 dB in the coupling loss between the laser module and the SMF (defined as $-10\log(P_f/P_0)$ dB). This coupling loss includes an assembly loss in concurrence with YAG-laser bonding. The coupled optical power from laser into the SMF was as high as 145 mW at 300 mA, which is a record value among 980-nm lasers with InGaP cladding.

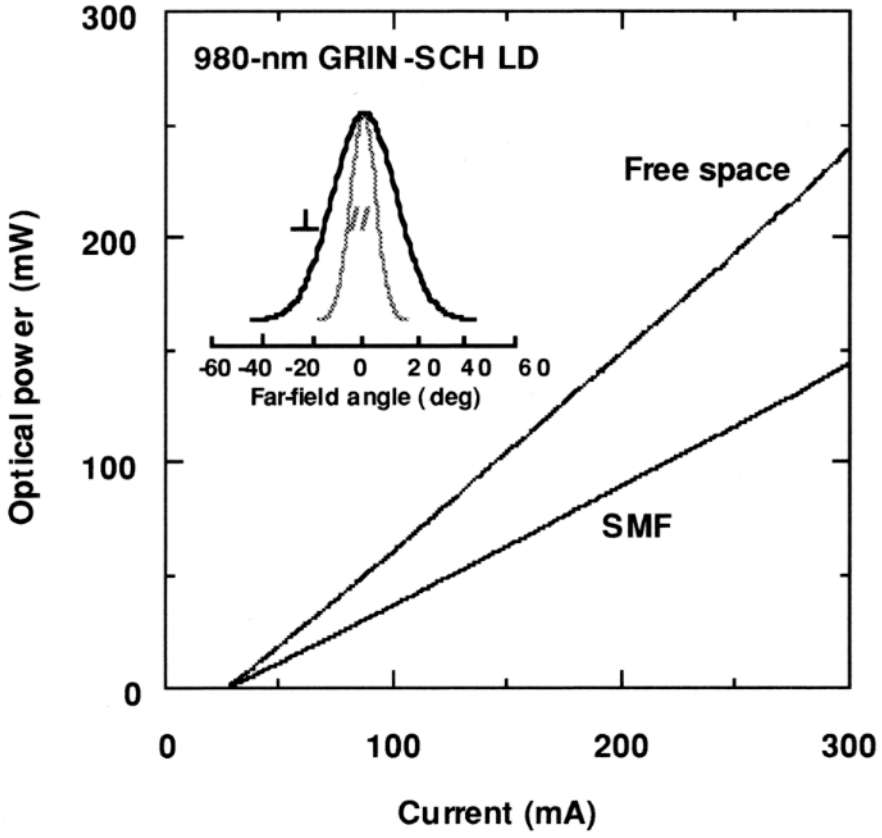

Fig. 4-21. Light/current characteristics in free space (P_0) and the SMF (P_f). The inset shows far field patterns.

4.4.2 High Reliability

One of the primary factors in deteriorating high-power GaAs-based lasers is facet degradation to be triggered by temperature rise at active mirror facets. In effect, a front facet incurred a rise in temperature of as much as a few hundred degrees [16,17]. It is also known that facet degradation depends largely on optical power density at facets. Therefore, it is desirable for high reliability to have a low power density. The last section describes a 3-step-GRIN-SCH laser with a 15-nm-InGaAsP-step, which was proved to have an optical confinement factor of as low as Γ=0.021, and expected to degrade slowly at facets.

Figure 4-22 traces an aging test of lasers operating at an automatic power control of 200 mW at 35 ℃, and. The optical power density of the quantum well active region was calculated as more than 30 MW/cm^2. Four 3-step-GRIN-SCH lasers, each having a mesa 2-μm in width, were set under test, after a screening test which was carried out at an automatic current control of 150 mA at 60 ℃ for 72 hours. What should be noteworthy is that none of the four lasers showed any significant degradation or any sudden failure (called COD) over a marvelous length of 6,000 hours. It is estimated based on the data in Fig. 4-22, that the end-of-life of these lasers with 150-mW output power will span more than 1×10^5 hours at 25 ℃. These results suggests that the pumping lasers of EDFAs seem promising for practical application: InGaP is proved to be advantageous or successful in creating steadfast reliability.

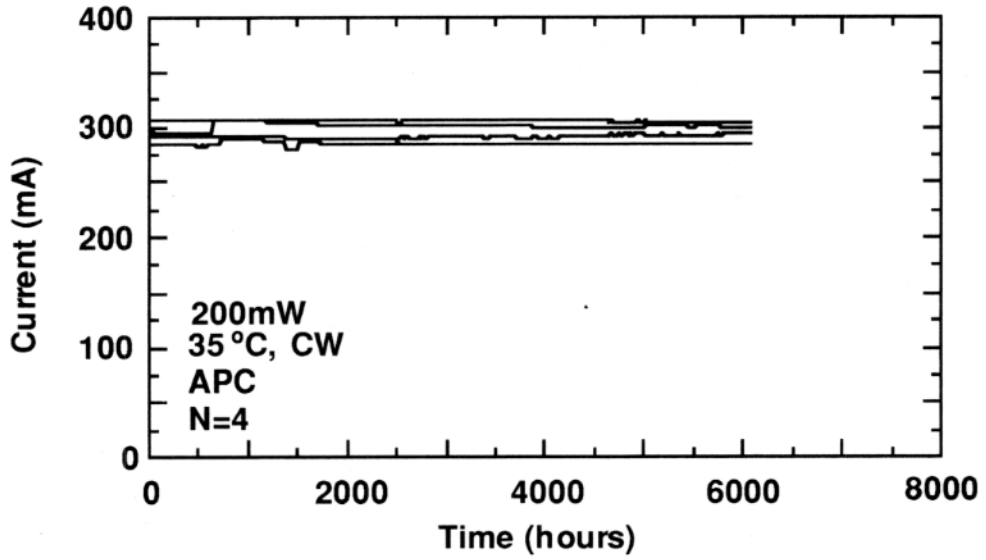

Fig. 4-22. Aging test results at an ambient temperature of 35 ℃ under an automatic control (APC) of 220 mW.

4.5 Summary

We have realized high-power aluminum-free 980-nm lasers, by taking the most advantage of graded-InGaAsP structures. Their graded bandgap structures, arising out of InGaAsP alloys lattice-matched to GaAs at InGaP/GaAs interfaces, can suppress heterojunction spikes, especially in the valence band, and also form the electric field to concentrate carriers in the quantum well active region. This task has brought out a drastic fall in series resistance of GRIN-SCH lasers, in comparison with SCH lasers. Furthermore, the optimized graded-structure has improved the temperature dependence of lasing characteristics (e.g., characteristic temperature). It is searched out that a GRIN-SCH waveguide with InGaAsP barriers is deserving of the optimum structure; 3-μm-wide GRIN-SCH lasers can realize a stand-out optical power of 350 mW at 500 mA, while carrying on a reliable operation at 200 mW over as long as 6,000 hours. At the same time, it turns out that a waveguide with controlled, graded refractive indices can form a confinement profile of less-divergent emission. In conclusion, a 2-μm-wide ridge mesa, having 2 of ellipticity ratio of far-field pattern ($\theta_{\perp}/\theta_{//}$), is proved to exhibit as high as 145 mW of coupled optical power from laser facet into an SMF as driven by 300 mA: those lasers will be in widespread practical use.

Appendix B

Beam Steering

Beam steering [18] causes nonlinearity 'kinks' in an L/I curve, which drops the coupling efficiency with a SMF. We have reported on theoretical approaches to the irksome beam steering, which apply self-consistent two-dimensional single-mode drift-diffusion simulator 'FELES' [19], in view of spatial hole burning [20]. Here is given an overview of the first observation of a periodic optical intensity distribution along the laser cavity in a preliminary backplane electroluminescence [14].

The prepared lasers were of InGaAs/InGaAsP/InGaP GRIN-SCH, with a polyimide-buried ridge waveguide. Figure B-1 shows the structural parameters of three types of lasers concerned in the backplane electroluminescence observation. The horizontal axis refers to the effective refractive indices (Δn) under control of a residual cladding thickness (d); the vertical axis refers to the ridge mesa width (W) under control of the width of photoresist mask in wet-chemical mesa-etching. 'Cut-off' of the first-order lateral mode in the figure was derived where the laser was regarded as a passive waveguide, by Effective Refractive Index Method. The figure teaches that a type A or B is able to support lasing in the fundamental or first-order lateral mode. But, type C laser can perform in the fundamental lateral mode.

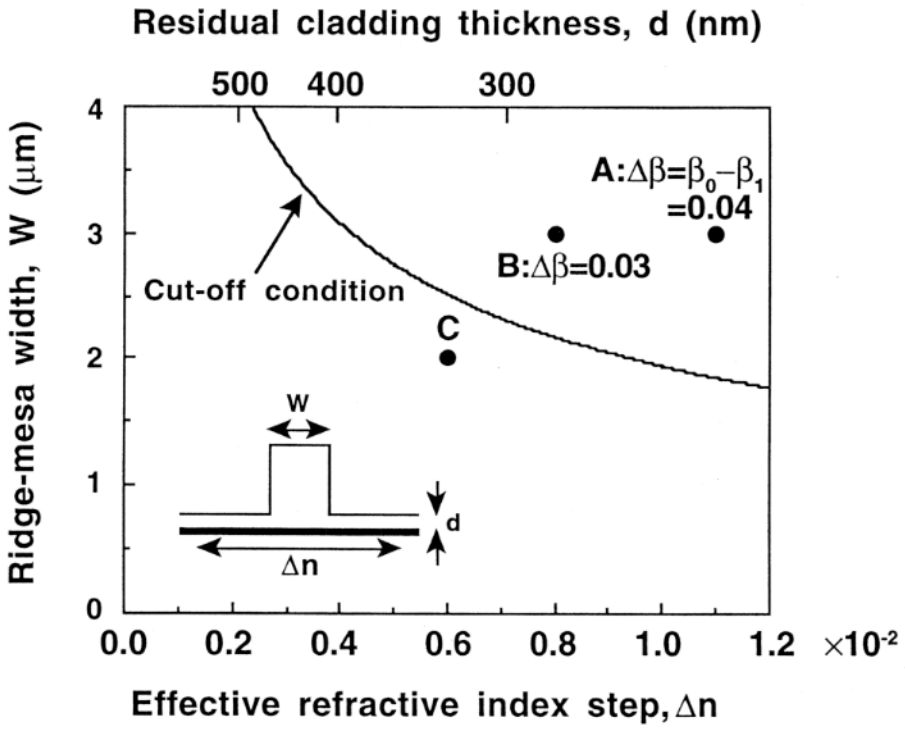

Fig. B-1. Structural parameters of three types of lasers.

Figure B-2 traces injection-current dependence of the lateral far-field pattern (FFP) of a type A laser. Current was injected by 60 to 200 mA in increments of 20 mA. It is perceivable that lateral beam steering emerged at 180 mA in concurrence with a kink. The FAHM of far-field pattern was measured as 18 ° and independent of injection current. Notably, this value did not agree with its calculated counterpart of 12.5 ° . This discrepancy indicates that self-focusing was induced by spatial hole burning. Similarly, a type B laser showed a salient kink at 250 mA of injection current.

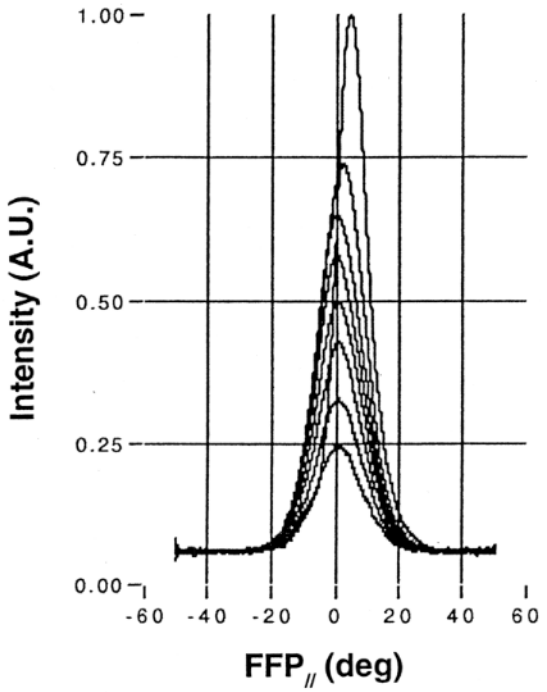

Fig. B-2. Injection current dependence of the lateral FFP of a type A laser.

Figure B-3 presents spot patterns in the backplane electroluminescence at (a) an injection current of I_{op} = 140 mA, an output optical power of P_{out} = 90 mW, and (b) I_{op} = 200 mA, P_{out} = 135 mW, where the type A laser (Δn = 0.011, W = 3 μm), having shown the first kink at 180 mA of injection current, was operated to search for spot patterns. IR-camera observation was performed through a window on the substrate to catch electroluminescence, namely spontaneous emission, from the active region along the laser cavity. Moderate current free from kinks made the electroluminescence form a straight pattern along the laser stripe as in Fig. B-3 (a). But then, a dark band appeared in the middle of the stripe, probably owing to the spatial hole burning, which was indicated by discrepancy between theoretical values and the measured counterparts in terms of FAHM in the lateral FFP. A rise up to 200 mA in injection current, a regular, periodic pattern of spots to move from side to side, at period of $\lambda_{beat} \fallingdotseq$ 135 μm. It turns out that the stimulated emission can be propagated through the dark region with higher refractive

indices than those of the bright region: stimulated emission and electroluminescence are of the same periodic structure. Assuming that the fundamental mode interferes with the first-order mode, its beat period can be figured out, so as to satisfy the cavity round-trip phase condition as expressed as:

$$\lambda_{beat}=\frac{2\pi}{\Delta\beta}. \qquad \text{(B.1)}$$

where $\Delta\beta$ is defined as difference in propagation constant between two lateral modes (specifically, $\Delta\beta = \beta_0-\beta_1$). The λ_{beat} of the A laser was found to be 160 μm, which is in good agreement with its experimental counterpart.

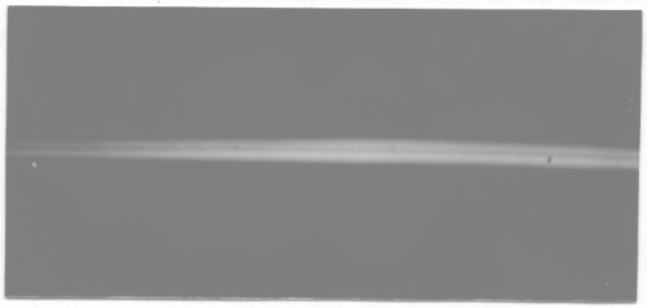

(a) I_{op} = 140 mA, P_{out} = 90 mW.

(b) I_{op} = 200 mA, P_{out} = 135 mW.

Fig. B-3. Spot patterns in the backplane electroluminescence at (a) an injection current of I_{op} = 140 mA, an output optical power of P_{out} = 90 mW, and (b) I_{op} = 200 mA, P_{out} = 135 mW.

Table B-1 in comparison lists experimental values and calculated counterparts of three types of laser. The type B laser with steps of low effective refractive indices, had longer period and showed less difference between experimental and calculated figures. Still, the type C laser, satisfying the cutoff condition, exhibited no periodic behavior in the backplane electroluminescence pattern and or kinks in the L/I characteristic. It is confirmed that the period of an electroluminescence pattern can be estimated with some accuracy, using Effective Refractive Index Method.

Table B-1. Comparison between the experimental values and calculated counterpart.

	Calculated period (μm)	Measured period (μm)
A	135	160
B	220	210
C	No	No

References

[1] M. Ohkubo, T. Ijichi, A. Iketani and T. Kikuta, "Aluminium free InGaAs/GaAs/InGaAsP/InGaP GRINSCH SL-SQW lasers at 0.98μm," *Electron. Lett.*, vol. 28, pp. 1149-1150, June 1992.

[2] M. Ohkubo, T. Ijichi, A. Iketani and T. Kikuta, "High power 1.017μm strained-layer quantum well lasers grown by metalorganic chemical-vapor deposition," *Appl. Phys. Lett.*, vol. 60, pp. 1413-1414, 1992.

[3] T. Ijichi, M. Ohkubo, N. Matsumoto and H. Okamoto, "High power CW operation of aluminium-free InGaAs/GaAs/InGaP strained layer single quantum well ridge waveguide lasers," *12th IEEE Int. Semiconductor Laser Conf., Davos, Switzerland*, 1990, D-2, pp. 44-45.

[4] J. W. Matthews and A. E. Blakeslee, "Defect in epitaxial multilayers," *J. Crystal Growth*, vol. 27, pp.118-125, 1974.

[5] B. Saint-Cricq, S. Bonnefont, R. Azoulay and L. Dugrand, "Performance characteristics of strained layer InGaAs/GaAs broad area ridge waveguide lasers," *Electron. Lett.*, vol. 27, no. 10, pp. 865-866, 1991.

[6] S. H. Groves, J. N. Walpole and L. J. Missaggia, "Very high efficiency GaInAsP/GaAs strained-layer quantum well lasers (λ=980 nm) with GaInAsP optical confinement layers," *Appl. Phys. Lett.*, vol. 61, pp. 255-257, 1992.

[7] M. Sagawa, K. Hiramoto, T. Tsuchiya, S. Tsuji and K. Uomi, "Advantages of InGaAsP separate confinement layer in 0.98μm InGaAs/GaAs/InGaP strained DQW lasers for high power operation at high temperature," *Electron. Lett.*, vol. 28, pp. 1639-1640, 1992.

[8] A. Iketani, M. Ohkubo, T. Ijichi and T. Kikuta, "First fabrication of continuously graded InGaAsP on GaAs for 0.98 μm lasers," *InP and Related Materials, Paris*, 1993, WF4.

[9] M. Ohkubo, S. Namiki, T. Ijichi, A. Iketani and T. Kikuta, "0.98μm InGaAs-InGaAsP-InGaP SL-SQW lasers for coupling high optical power into single-mode fiber", *IEEE J.Quantum Electron.*, vol. 29, no. 6, pp. 1932-35, June, 1993.

[10] H. Hirayama, Y. Miyake and M. Asada, "Analysis of injection efficiency of separate-confinement-heterostructure quantum-film lasers," *IEEE J. Quantum Electron.*, vol. 28, no. 6, pp. 68-74, January, 1992.

[11] R. Nagarajan, T. Fukushima, S. W. corzine and J. E. Bowers, "Effects of carrier transport on high speed quantum well lasers," *Appl. Phys. Lett.*, vol. 59, pp. 1835-1837, 1991.

[12] K. Utaka, Y. Suematsu, K. Kobayashi and H. Kawanishi, "GaInAsP/InP integrated twin-guide lasers with first-odrer distributed Bragg reflectors at 1.3 μm wavelength," *Jpn. J. Appl. Phys.*, vol. 19, pp. L137-L140, 1980.

[13] M. Yamada, S. Ogita, T. Miyabo and Y. Nashida, "A theoretical analysis of lasing gain and threshold current in GaAs-AlGaAs SCH lasers," *Trans. IEICE.*, vol. E 69, pp.948-954, 1986.

[14] M. Ohkubo, Y. Ikegami, T. Ijichi and T. Ninomiya, "Experimental study of beam steering in 980-nm InGaP cladding lasers," *Jpn. J. Appl. Phys.*, vol. 35, pp. L34-L36, 1996.

[15] S. Namiki, Y. Shirasaka, and T. Kikuta, "0.98 μm high power laser modules," *Proceedings of the 1993 ICIER Spring Conference, March, Nagoya*, C-174, pp. 4-210, 1993.

[16] S. Todoroki, M. Sawai and K. Aiki, "Mapping of local temperatures on mirrors of GaAs/AlGaAs laser diodes," *J. Appl. Phys.*, vol. 58, vol. 3, pp. 1124-1128, 1985.

[17] H. Brugger and P. W. M. Epperlein, "Mapping of local temperatures on mirrors of GaAs/AlGaAs laser diodes," Appl. Phys. Lett. vol. 56, no. 11, pp. 1049-1051, 1990.

[18] J. Napi, A. Ovtchinnikov, H. Asonen, P. Savolainen and M. Messa, "Limitation of two-dimensional passive waveguide model for λ = 980 nm Al-free ridge waveguide lasers," Appl. Phys. Lett. vol. 64, no. 17, pp. 2203-2205, 1994.

[19] G. L. Tan, K. Lee and J. M. Xu, "Finite element light emitter simulator (FELES): A new 2D software design tool for laser devices," *Jpn. J. Appl. Phys.*, vol. 32 pp. 583-589, 1993.

[20] J. Guthrie, G. L. Tan, M. Ohkubo, T. Fukushima, Y. Ikegami, T. Ijichi, M. Irikawa, R. S. Mand and J. M. Xu, "Beam Instability in 980-nm Power Lasers: Experimental and Analysis," *IEEE Photon. Technol. Lett.*, vol. 6 pp. 1409-1411, 1994.

Chapter 5

Improvement of Temperature Dependence of GRIN-SCH Lasers

The last chapter ranges over demonstrations of high-power operations with optimum graded-structure, 980-nm lasers. Improving temperature dependence desirably leads into the enhancement of lasing characteristics, e.g., less sensitivity to operation temperature, operating reliability. Some reports indicate that a decrease of mirror loss can improve a mass of lasing characteristics in quantum well lasers [1-3]. This chapter explains the effects of mirror reflectivity on lasing characteristics — especially at characteristic temperature T_0, a distinctive factor in lasing performance to temperature.

5.1 Improvement of Temperature Dependence with Low Mirror Loss

5.1.1 Sample Preparation

The prepared samples were polyimide-buried InGaAs/InGaAsP/InGaP 3-step GRIN-SCH lasers with InGaAsP barriers [4]. Each ridge mesa was controlled to be as narrow as 2 μm in bottom width, while each cavity length (L_c) was 1 mm. The high reflectivity (R_r = 95 %) facet composed of three pairs of Si/SiO dielectric layers. The other one was coated with a low-reflective (LR) SiN layer, where a reflectivity (R_f) was controlled to be within a variation of 1 % and 28 %. These lasers are mounted on Si heatsinks with junction-down configuration.

5.1.2 Improvement in Lasing Performance

Figure 5-1 draws light/current characteristics of a GRIN-SCH laser with a LR facet (R_f = 28 %), which was operated at temperatures of 10, 30, 50 and 70 ℃. This laser exceeded 0.8 W/A of stand-out output efficiency at all temperatures throughout. Figure 5-2 shows temperature dependence of external differential quantum efficiency as a function of LR reflectivity, as normalized at 10 ℃. A rise in LR reflectivity decreases temperature dependence of the external differential quantum efficiency. Figure 5-3 shows temperature dependence of threshold current as a function of LR reflectivity. Characteristic temperature (T_0) increased remarkably, in step with the LR reflectivity on the increase. To investigate this phenomenon, I estimated the temperature dependence of conventional parameters of the lasers, on the strength of a logarithmic current-gain relation.

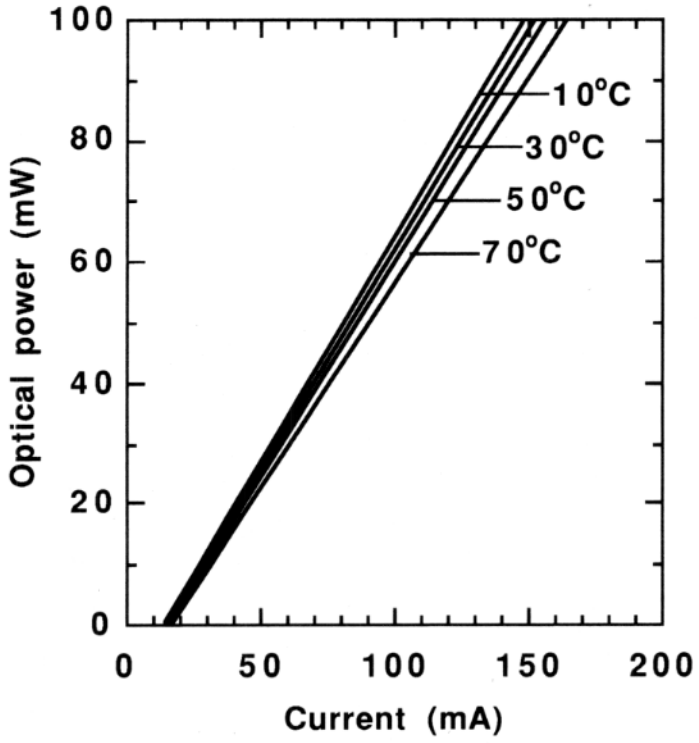

Fig. 5-1. Light/current characteristics of the LR(R_f = 28 %)/HR(R_r = 95 %)-coated 2-μm-wide and 1-mm-long InGaAs/InGaAsP/InGaP GRIN-SCH laser.

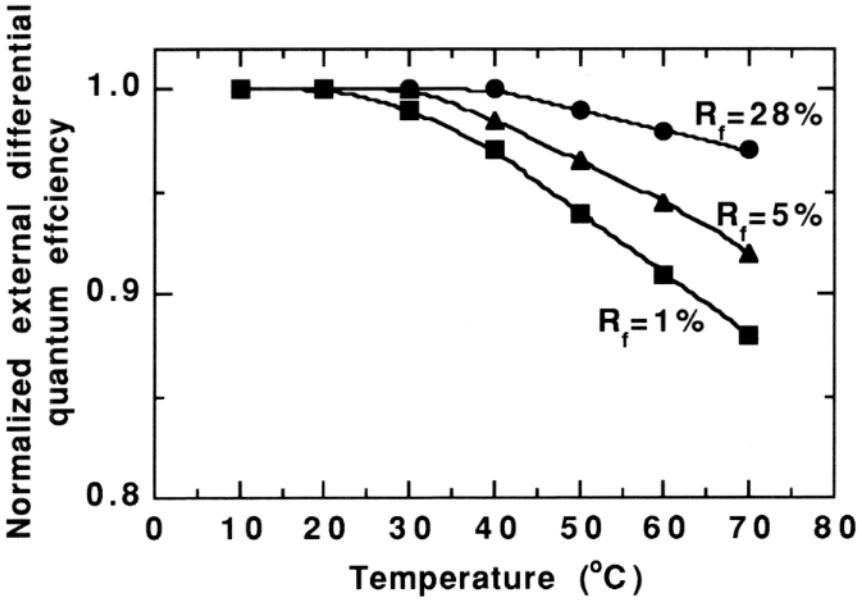

Fig. 5-2. Inverse external differential quantum efficiency as a function of inverse mirror loss.

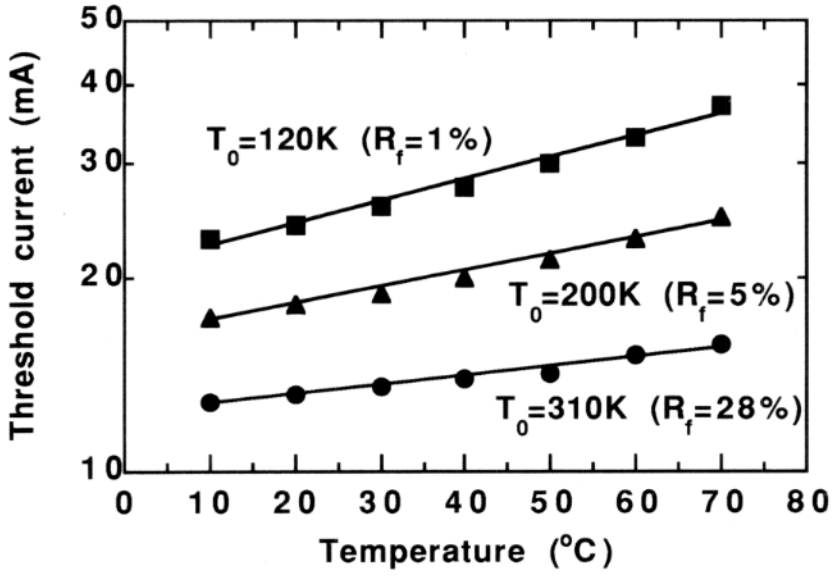

Fig. 5-3. Temperature dependence of threshold current of GRIN-SCH lasers as a function of LR reflectivity.

5.2 Consideration Using Current-Gain Relation

Injected current density (J) and optical gain (G) can be logarithmically related with considerable accuracy, according to the following approximation for quantum well lasers [5]:

$$G=G_0\ln\left(\frac{J}{J_0}\right), \tag{5-1}$$

where J_0 is transparent current density. The differential gain is simply defined as G_0/J_0. At a threshold, the net gain G from the quantum well is equal to the total cavity loss, consisting of internal loss α_i and mirror loss α_m. Thus, threshold condition is as:

$$\Gamma G_{th}=\alpha_i+\frac{1}{2L_c}\ln\frac{1}{R_fR_r}, \tag{5-2}$$

where Γ is optical confinement factor. The threshold current density (J_{th}) is expressed in view of (5-2):

$$\ln(J_{th})=\frac{1}{G_0\Gamma}\left(\alpha_i+\frac{1}{2L_c}\ln\frac{1}{R_fR_r}\right)+\ln\left(\frac{J_0}{\eta_i}\right), \tag{5-3}$$

where L_c is cavity length, α_i is internal loss and η_i is internal differential quantum efficiency; G_0, α_i, η_i and J_0 being dependent parameters on temperature. T_0 can be generally expressed as:

$$\frac{1}{T_0}=\frac{\partial}{\partial T}\ln(J_{th}). \tag{5-4}$$

The above parameters were analyzed, in terms of contribution to T_0: their temperature dependence was estimated.

Figure 5-4 shows inverse external differential quantum efficiency as a function of inverse mirror loss $\ln(R_fR_r)^{-1}/(2L_c)$. The α_i value, regarded as a constant 3 cm^{-1} from 10 ℃ to 70 ℃, can remain unaffected in the temperature range. Then, η_i is weakly dependent on temperature as plotted in Fig. 5-5, and can be approximated as:

$$\eta_i=1-\frac{T-T_{\eta i=1}}{T_{\eta i}}. \tag{5-5}$$

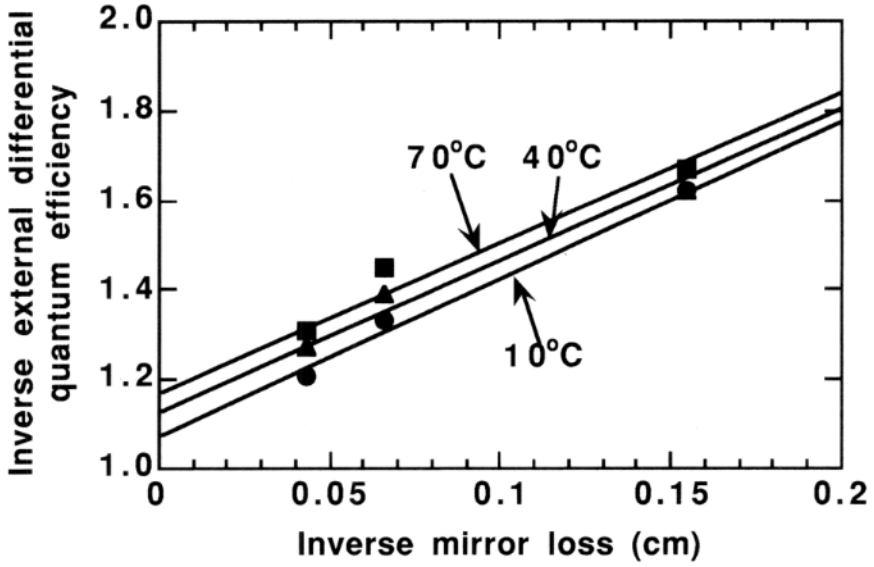

Fig. 5-4. Inverse external differential quantum efficiency as a function of the inverse mirror loss.

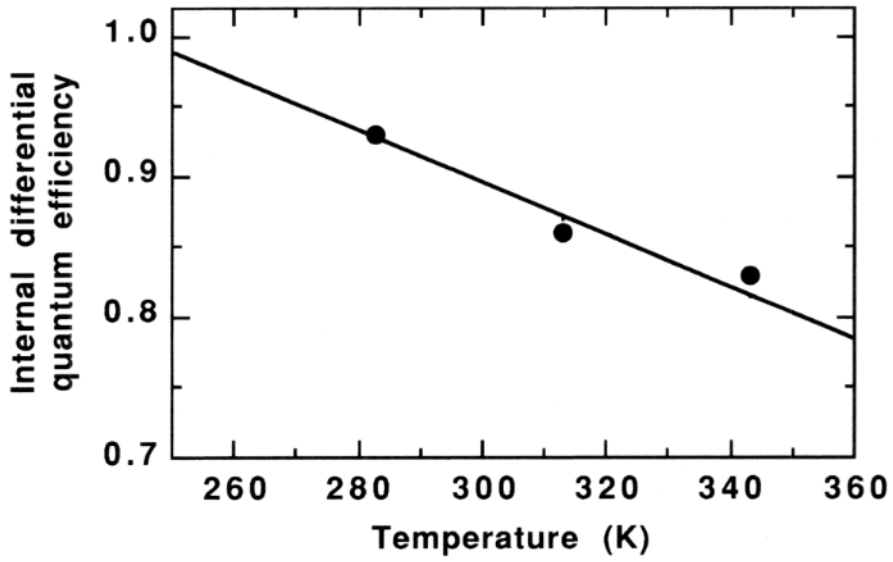

Fig. 5-5. Internal differential quantum efficiency as a function of temperature.

$T_{\eta i=1}$ denotes that η_i representing 1. $T_{\eta i=1}$ and $T_{\eta i}$ are calculated as 243 K and 550 K, which shows η_i is also weakly dependent on temperature.

Figure 5-6 plots the optical gain $(1/2L_c\Gamma)\ln(1/R_fR_r)$ as a function of threshold current density. J_0 remains constant at a value of 270 A/cm^2 from 10 to 70 ℃, throughout. G_0 is strongly dependent on temperature and approximated as:

$$G_0=3980\left(1-\frac{T}{T_{G0}}\right). \tag{5-6}$$

T_{G0} is calculated as 450 K as given in Fig 5.7, indicating that G_0 is the most susceptible to temperature variation concerning other three parameters (α_i, η_i and J_0). Still, the temperature dependence of G_0 is far less than of InP-based quantum well lasers, being less in T_0 value, than GaAs-based lasers [6]. Thus, T_0 can be transformed as:

$$\frac{1}{T_0}=\left(\alpha_i+\frac{1}{2L_c}\ln\frac{1}{R_fR_r}\right)\frac{(-1)}{(G_0\Gamma)^2}\cdot\frac{\partial(G_0\Gamma)}{\partial T}\cdot\frac{1}{\eta_i}\frac{\partial\eta_i}{\partial T}. \tag{5-7}$$

It should be noted that $1/T_0$ increases directly in step with the mirror loss $\ln(R_fR_r)^{-1}/(2L_c)$, in this case, where $1/T_0$ can be finalized as $A+B\cdot\ln(R_fR_r)^{-1}/(2L_c)$. Practically, $1/T_0$ as variable with mirror loss, can be expressed as $A+B\cdot\ln(R_fR_r)^{-1}/(2L_c)$ in comformity to Fig. 5-8, where a logarithmic current-gain relation is predicted. As for an infinite cavity length, T_0 is driven into saturation over 400 K, corresponding to those of 980-nm GRIN-SCH lasers, estimated by some other researcher [7]. This tight dependence of T_0 on the facet reflectivity of a laser stems from the four parameters being least dependence on temperature. Moreover, a high T_0 can be linked with a really high absolute G_0 value or least temperature dependence of G_0, considering InP-based lasers. What was verified last is that the logarithmic relation between current density and optical gain can be of appropriate approximation for quantum well lasers. The adequacy is supported by Fig. 5-8 and expression (5-7) which agree with each other, more than enough.

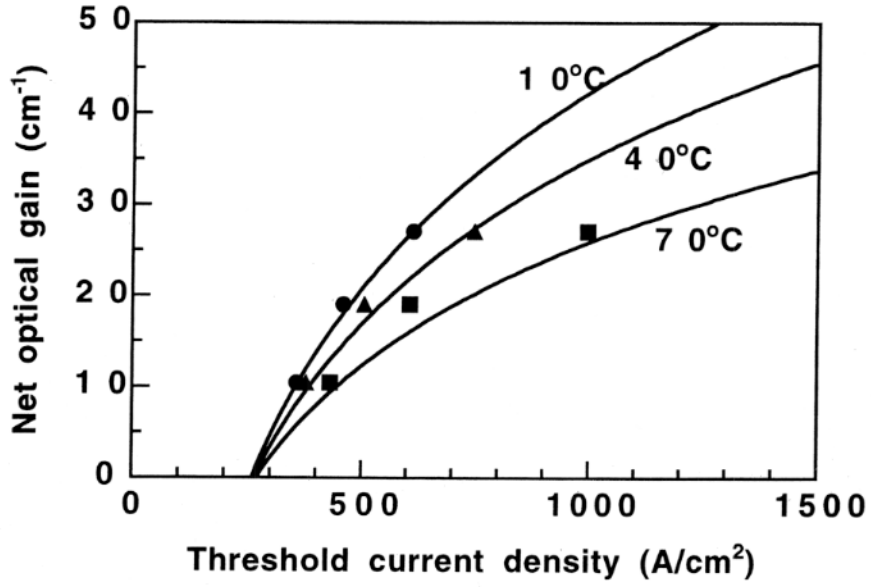

Fig. 5-6. Net optical gain $(1/2L_c\Gamma)\ln(1/R_fR_r)$ as a function of threshold current density.

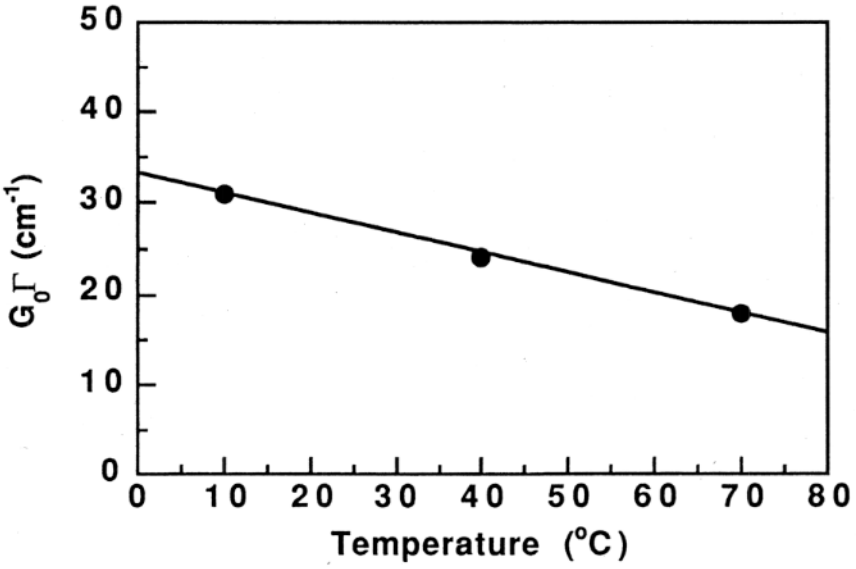

Fig. 5-7. G_0 as a function of temperature.

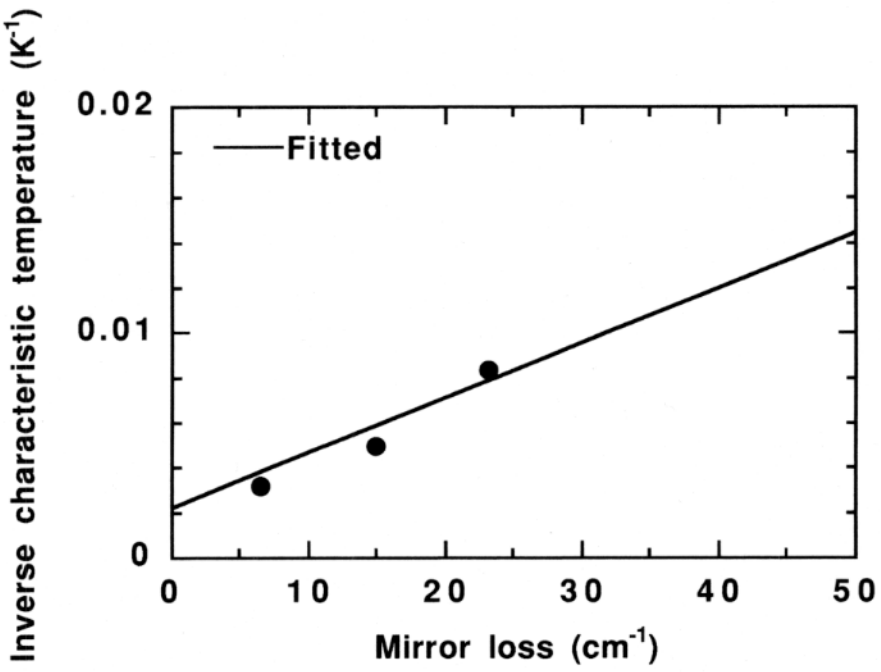

Fig. 5-8 Inverse T_0 as a function of the mirror loss.

5.3 Summary

The mechanics of lasing performance in view of mirror reflectivity was investigated and interpreted in the form of logarithmic relation between current density and optical gain. Two significant findings are T_0 to be driven into saturation over 400 K, and weak temperature dependence and high G_0 to serve as dominant factor in high values of T_0.

References

[1] M. M. Leopold, P. A. Specht, C. A. Zmudzinski, M. E. Givens and J. J. Coleman, "Temperature-dependent factors contributing to T_0 in graded-index separate-confinement-heterostructure," *Appl. Phys. Lett.*, vol. 50 pp. 1403-1405, 1987.

[2] J. Z. Wilcox, G. L. Seterson, S. S. Ou, J. J. Yang, M. Jansen and D. Schechter, "Gain dependence of the threshold characteristics temperature in multiple quantum well lasers," *Appl. Phys. Lett.*, vol. 53, pp. 2272-2274, 1988.

[3] N. Matusmoto, A. Kasukawa, H. Okamoto and S. Kashiwa, "Reduction of threshold current and enhancement of characteristic temperature in 1.3 μm GaInAsP GRIN-SCH-MQW laser diodes by facet coating," Inst. Conf. Ser. No 106: Chapter 10, pp. 765-770, 1989.

[4] M. Ohkubo, S. Namiki, T. Ijichi, A. Iketani and T. Kikuta, "0.98μm InGaAs-InGaAsP-InGaP SL-SQW lasers for coupling high optical power into single-mode biber", *IEEE J.Quantum Electron.*, vol. 29, no. 6, pp. 1932-35, June, 1993.

[5] B. Saint-Cricq, S. Bonnefont, R. Azoulay and L. Dugrand, "Performance characteristics of strained layer InGaAs/GaAs broad area ridge waveguide lasers," *Electron. Lett.*, vol. 27, no. 10, pp. 865-866, 1991.

[6] T. Namegaya, N. Matsumoto, N. Yamanaka, N. Iwai, H. Nakayama and A. Kasukawa, "Effects of well number in 1.3-μm GaInAsP/InP GRIN-SCH starined-layer quantum-well lasers," *IEEE J. Quantum Electron.*, vol. 30, no. 2, pp. 578-584, 1994.

[7] S. Kubota, H. Kurakake, T. Uchida, S. Ogita and H. Soda, "Threshold current density dependence of characteristics temperature in the 0.98μm InGaAs laser," 54th Autumn Meeting of Japan Society of Applied Physics, 29p-K-15, September, 1993.

Chapter 6

Conclusions

Conclusions are articulated with three captions, as follows:

1. Design and Optimization of Aluminum-Free 980 nm GRIN-SCH Lasers.

It has been verified that valence band discontinuity is much higher than conduction band discontinuity in an InGaP/InGaAsP/GaAs system, on the strength of I-V characteristics of the heterojunction. This nature dominates the series resistance of high-power aluminum-free 980-nm lasers. In this study, the nature at issue has been countervailed by inserting 'graded-InGaAsP' into a GaAs/InGaP interface. The manipulation has given birth to an optimized InGaP/graded-InGaAsP/GaAs structure, which reduces unwanted excess voltage in a mass.

Concurrently, a second advantage of the graded-structures works out: its unique electric field, enhancing the carrier population in the quantum well active layer, improves temperature dependence of the lasing characteristics.

2. Establishment and Characterization of MOCVD-Growth of Graded-InGaAsP Structures.

It has been demonstrated that InGaAsP layers on GaAs is equipped with ready compositional-controllability, with the aid of the MOCVD apparatus dedicated in this study. But then, a compositionally immiscible region existing in the MOCVD growth of an InGaAsP on GaAs was caught by PL measurements. Still, this drawback can be resolved by a minor modification of the growth conditions, where graded-InGaAsP structures can be grown without difficulty, so as to realize aluminum-free 980-nm GRIN-SCH lasers.

InGaAs/InP D-HBTs with step-like graded InGaAsP layers between the InGaAs base and InP collector, were made in proof of the effects of graded-bandgap structures, or to characterize the quality of graded-InGaAsP interfaces. Notably it has been brought to light, that inserted graded layers can suppress hetero-interface spikes effectively, without increasing any recombination-generation centers in the graded-InGaAsP region.

3. Realization of High-Power Aluminum-free 980-nm GRIN-SCH Lasers.

High-power aluminum-free 980-nm GRIN-SCH lasers have been realized with making good use of advantages of the graded-InGaAsP structures. The graded-bandgap structures, consisting of InGaAsP alloys lattice-matched to GaAs at the InGaP/GaAs interfaces, thereby make heterojunction spikes ungrown, especially in the valence band,

and forms a unique electric field to make carriers concentrate in the quantum well active region. Consequently, series resistance as to GRIN-SCH lasers drastically drops, as contrasted with SCH lasers. In particular, the optimized, graded-structure improved temperature dependence of the lasing characteristics (e.g., characteristic temperature). The topical lasers seem promising in view of the practical application in industries. Here is a lineup of significant extracts: the optimum structure was a 3-step-GRIN-SCH waveguide with InGaAsP barriers. Devices of 3-μm-wide GRIN-SCH lasers reached an output of remarkably 350 mW at 500 mA. while carrying on an endurance as trouble free, over 6000 hours-operation at 200 mW. A controlled-graded-refractive indices waveguide exhibited an optical confinement profile of less-divergent emission beam. In reality, a 2-μm-wide ridge mesa with 2 of ellipticity ratio of far-field pattern gave birth to a coupled optical power of as high as 145 mW into an SMF, as driven by 300 mA.

Acknowledgment

First and foremost, I must express my heartiest thanks to Professor Shigehisa Arai, Tokyo Institute of Technology, who have supported my toilsome task from phase to phase with resourceful advice.

At the same time, I sincerely thank all members of my doctoral dissertation committee at Tokyo Institute of Technology, Prof. K. Furuya, Prof. M. Konagai, Associate Prof. O. Sugiura and, especially, Associate Professor Y. Miyamoto who gave me pieces of pivotal advice, along the way.

Then, I have to thank a volume of colleagues at The Furukawa Electric Co. Ltd.: Mr. S. Kashiwa, Mr. J. Kikawa, Mr. T. Kikuta, Dr. M. Ogai, Mr. M. Irikawa and Mr. T. Ninomiya, who have encouraged this study of mine and myself. In all sincerity, I thank those who have cooperated in the hand-on research: Messrs. T. Ijichi and A. Iketani (earnest colleague collaborators); Dr. A. Kasukawa, Mr. Y. Ikegami, Dr. T. Fukushima and Mr. T. Namegaya who have given incentives to me during the discussions about lasers and MOCVD-growth; Dr. S. Namiki (laser module fabrication); Messrs. S. Tanaka and N. Ikeda who have given incentives to me during the discussions about HBTs, Messrs. Y. Sasaki, N. Iwai, J. Osabe and M. Ito (technical assistance); Mr. T. Matsuda (TEM observation) and M. S. Seo (SIMS measurement).

In addition, I wish to thank Dr. N. Yokoyama and Mr. S. Shigematsu, Fujitsu Laboratories Co. Ltd. (valued advice about HBTs); Dr. I. Yoshida, Sumitomo Electric Industries and Ms. N. Furusaki, Mitsubishi Kagaku Co. Ltd. (mental encouragement).

In particular, I am appreciative of prose patterns, with which this doctoral dissertation of mine was favored by Mr. A. Ito, corporate technical writer & translator.

List of Publications

Papers and Letters

1. M. Ohkubo, A. Iketani, T. Ijichi and T. Kikuta, "InGaAs/InP double-heterojunction bipolar transistors with step graded InGaAsP between InGaAs base and InP collector grown by metalorganic chemical vapor deposition," *Appl. Phys. Lett.*, vol. 59, no. 21, pp. 2697-2699, 1991.
2. M. Ohkubo, T. Ijichi, A. Iketani and T. Kikuta, "High power 1.017μm strained-layer quantum well lasers grown by metalorganic chemical-vapor deposition," *Appl. Phys. Lett.*, vol. 60, no. 12, pp. 1413-1414, 1992.
3. M. Ohkubo, T. Ijichi, A. Iketani and T. Kikuta, "Aluminum free InGaAs/GaAs/InGaAsP/InGaP GRINSCH SL-SQW lasers at 0.98μm," *Electron. Lett.*, vol. 28, no. 12, pp. 1149-1150, June 1992.
4. M. Ohkubo, S. Namiki, T. Ijichi, A. Iketani and T. Kikuta, "0.98μm InGaAs-InGaAsP-InGaP SL-SQW lasers for coupling high optical power into single-mode fiber", *IEEE J. Quantum Electron.*, vol. 29, no. 6, pp. 1932-1935, June, 1993.
5. T. Ijichi, M. Ohkubo, A. Iketani and T. Kikuta, "High-power 0.98-μm strained quantum-well lasers with InGaP cladding," *Microwave and Optical Technology Letters*, vol. 7, no. 3, pp. 139-143, 1994.
6. M. Ohkubo, T. Ijichi, A. Iketani and T. Kikuta, "980-nm aluminum-free InGaAs/InGaAsP/InGaP GRIN-SCH SL-SQW lasers", *IEEE J. Quantum Electron.*, vol. 30, no. 2, pp. 408-414, June, 1994. (Invited)
7. M. Ohkubo, A. Iketani, M. Ikeda and T. Ninomiya, "Emitter material comparison between InGaP and InGaAsP in GaAs-based heterojunction bipolar transistors," *Jpn. J. Appl. Phys.*, vol. 33, L993-L995, 1994.
8. M. Ohkubo, N. Iwai, T. Ijichi and T. Ninomiya, "Very weak dependence on temperature of 980-nm InGaAs/InGaAsP/InGaP lasers," *Jpn. J. Appl. Phys.*, vol. 33, pp. L1307-L1309, 1994.
9. J. Guthrie, G. L. Tan, M. Ohkubo, T. Fukushima, Y. Ikegami, T. Ijichi, M. Irikawa, R. S. Mand and J. M. Xu, "Beam instability in 980-nm power lasers: experimental and analysis," *IEEE Photon. Technol. Lett.*, vol. 6, no. 12, pp. 1409-1411, 1994.
10. M. Ohkubo, Y. Ikegami, T. Ijichi and T. Ninomiya, "Experimental study of beam steering in 980-nm InGaP cladding lasers," *Jpn. J. Appl. Phys.*, vol. 35, pp. L34-L36, 1996.

Related Papers

1. M. Ohkubo, S. Tanaka, M. Irikawa and T. Kikuta, "Heavily Zn-doped graded-base AlGaAs/GaAs HBT's," *IEEE Trans. Electron Devices*, vol. 38, No. 6, pp. 1557-1560, 1991.
2. M. Ohkubo, N. Ikeda and T. Ninomiya, "Graded $GaAs_{1-X}P_X$ bases in heterojunction bipolar transistors with InGaP emitters," *Microwave and Optical Technology Letters*, vol. 11, no. 3, pp.150-153, 1996.

International Conferences

1. T. Ijichi, M. Ohkubo, N. Matsumoto and H. Okamoto, "High power CW operation of aluminum-free InGaAs/GaAs/InGaP strained layer single quantum well ridge waveguide lasers," *12th IEEE Int. Semiconductor Laser Conf.*, Davos, Switzerland, 1990, D-2, pp. 44-45.
2. M. Ohkubo, A. Iketani, T. Ijichi and T. Kikuta, "InGaAs/InP double-heterojunction bipolar transistors with step graded InGaAsP between InGaAs base and InP collector grown by metalorganic chemical vapor deposition," *3rd InP and Related Materials, Cardiff*, 1991, TuE2.
3. M. Ohkubo, A. Iketani, T. Ijichi and T. Kikuta, "Aluminum free InGaAs/GaAs/InGaAsP/InGaP GRIN-SCH strained layer single quantum well lasers emitting at 0.98μm," *Conference on Lasers & Elector-Optics*, 1992, CPD24.
4. T. Ijichi, M. Ohkubo, A. Iketani and T. Kikuta, "InGaAs/GaAs strained layer quantum well lasers using InGaP for cladding layers," *4th Optoelectronics Conf., Chiba*, 1992, 17B1-2.
5. A. Iketani, M. Ohkubo, T. Ijichi and T. Kikuta, "First fabrication of continuously graded InGaAsP on GaAs for 0.98μm lasers," *5th InP and Related Materials, Paris*, 1993, WF4.
6. T. Ijichi, M. Ohkubo, Y. Ikegami and T. Kikuta, "Circular beam 980-nm strained QW lasers," *Optical Amplifiers and Their Application, Yokohama*, 1993, TuC3.
7. M. Ohkubo, N. Ikeda and T. Ninomiya, "Graded-$GaAs_{1-X}P_X$ base in heterojunction bipolar transistors with InGaP emitters," *7th InP and Related Materials, Sapporo*, 1995, ThP23.

Domestic Conferences

1. T. Ijichi, M. Ohkubo, A. Nakai, N. Matsumoto, H. Okamoto and S. Kashiwa, "Strained quantum well lasers using InGaP cladding layer," 37th Spring Meeting of Japan Society of Applied Physics, 30a-SA-8, March 1990.
2. M. Ohkubo, T. Ijichi, Y. Ikegami, T. Kikuta and H. Okamoto, "High power InGaAs/GaAs/InGaP strained layer quantum well lasers," 51st Autumn Meeting of Japan Society of Applied Physics, 28a-R-10, September 1990.
3. M. Ohkubo, A. Iketani, T. Ijichi and T. Kikuta, "InGaAs/InP D-HBTs with graded-InGaAsP layers between InGaAs base and InP collector grown by MOCVD," 52nd Autumn Meeting of Japan Society of Applied Physics, 9p-H-16, October 1991.
4. T. Ijichi, M. Ohkubo, A. Iketani and T. Kikuta, "Characteristics of 1.06μm InGaAs/GaAs/InGaP strained layer quantum well lasers," 52nd Autumn Meeting of Japan Society of Applied Physics, 12a-ZM-6, October 1991.
5. M. Ohkubo, T. Ijichi, A. Iketani and T. Kikuta, "High power operation of InGaAs/GaAs/InGaP strained layer quantum well lasers," 39th Spring Meeting of Japan Society of Applied Physics, 29a-SF-24, March 1992.
6. A. Iketani, M. Ohkubo, T. Ijichi and T. Kikuta, "0.98μm strained layer quantum well lasers using InGaAsP-GRIN structure," 53rd Autumn Meeting of Japan Society of Applied Physics, 17a-V-3, September 1992.
7. M. Ohkubo, A. Iketani, S. Namiki, T. Ijichi and T. Kikuta, "0.98μm strained layer quantum well lasers using InGaAsP-GRIN structure (2)," 40th Autumn Meeting of Japan Society of Applied Physics, 31p-C-12, March 1993.
8. M. Ohkubo, A. Iketani, M. Ikeda and T. Kikuta, "Static characteristics of InGaAsP/GaAs HBTs with carbon-doped base," 54th Autumn Meeting of Japan Society of Applied Physics, 28a-ZP-2, September 1993.
9. N. Iwai, M. Ohkubo, A. Iketani, T. Ijichi and T. Ninomiya, "0.98μm strained layer quantum well lasers using InGaAsP-GRIN structure (3)," 54th Autumn Meeting of Japan Society of Applied Physics, 29p-K-17, September 1993.
10. M. Ohkubo, Y. Ikegami, T. Ijichi and T. Ninomiya, "0.98μm strained layer quantum well lasers using InGaAsP-GRIN structure (4)," 42nd Autumn Meeting of Japan Society of Applied Physics, 28p-ZG-1, March 1995.
11. N. Ikeda, M. Ohkubo and T. Ninomiya, "Graded-$GaAs_{1-X}P_X$ base in HBTs with InGaP emitters," 42nd Autumn Meeting of Japan Society of Applied Physics, 28p-ZL-8, March 1995.

12. T. Shiojima, M. Ohkubo N. Ikeda, T. Yamaguchi and T. Ninomiya, "InGaP/GaAs HBTs with $In_{0.5}(Ga_{1-X}Al_X)P_{0.5}$ hetero-guarding layers," 43rd Autumn Meeting of Japan Society of Applied Physics, 28p-M-2, March 1996.
13. N. Ikeda, M. Ohkubo and T. Ninomiya, "RF characteristics of graded-$GaAs_{1-X}P_X$ base HBTs," 43rd Autumn Meeting of Japan Society of Applied Physics, 28p-M-3, March 1996.

Symposia

1. M. Ohkubo, Y. Ikegami, Y. Sasaki, T. Aikiyo, T. Ijichi, A. Kasukawa and T. Ninomiya, "Experimental study of beam steering phenomenon in 980nm InGaP cladding lasers," *IEICE, Lasers and Quantum Electronics*, LQE95-84, Oct., 1996.
2. N. Ikeda, M. Ohkubo and T. Ninomiya, "Development of graded $GaAs_{1-X}P_X$ bases in heterojunction bipolar transistor," *IEICE, Electron Devices*, ED95-139, Jan., 1996.